Comparison Of Measured Photon And Electron Beam Dose Distributions Between 3D Water Phantom And Profiler 2 Scanning Systems, South Africa.

M.Sc. (Physics)

K M Moji

2013

Comparison Of Measured Photon And Electron Beam Dose Distributions Between 3D Water Phantom And Profiler 2 Scanning Systems, South Africa.

By

Kabelo McDonald Moji

RESEARCH DISSERTATION

Submitted in fulfillment of the requirements for the degree of

Master of Science

in

PHYSICS

in the

Faculty of Health Sciences

at the

University of Limpopo

Supervisor: Dr. Mpho Enoch Sithole

2013

Declaration

I declare that the dissertation hereby submitted to the University of Limpopo, for the degree of master of science has not previously been submitted by me for a degree at this or any other university, that this is my work in design and in execution, and that all material contained herein has been duly acknowledged.

_____ _____

Initials & Surname (Title) Date

Student Number:_____

Acknowledgements

I would like to acknowledge the contributions of Doctor Mpho Enoch Sithole and Miss Welhemina Letsoalo who provided valuable comments during the initial phase of the project. Credit to be given to Klerksdorp / Tshepong Hospital Complex for the support and permission to use and utilize their facilities to make this project possible.

I would like to thank again Doctor Mpho Enoch Sithole for his contribution as a supervisor and inputs on setting up the program, he deserves a special recognition. Thanks to be sent to
Mr. Modisenyane Mongane (MSc student at University of the Free State) and Mr. Nhlakanipho Mdletshe (Medical Physicist at Greys Hospital - Pietermaritzburg) for their contribution in providing the necessary assistance with references.

I would also like to thank my aunt Mrs. Matshediso Moji, who has been a mother to me, from when I was six months old, for what she has been to me, from then till now.

Lastly, but not least, Our Heavenly Father, the beginning and the end, for the sincerity, talent and grace He has given me to perform my best, as well as blessing me with three kids, Onkarabile Seakgoe (my daughter), Lehlohonolofaditswe Moji (my first son) and lastly Rearabetswe Moji (my younger son).

ABSTRACT

Background and Objectives: To establish whether the profiler 2 scanning system can be used as a substitute for the 3D-water phantom, by comparing the percentage depth doses and beam profiles for both the photons and electron beams, and validating the results using CMS XiO treatment planning system.

Methods: Beam data (profiles, percentage depth doses and absolute dosimetry) were acquired for the two systems: (3D-water phantom and profiler 2 scanning system) for beam energies 6 MV and 15 MV photon beams, and 4, 6, 8, 10, 12 and 15 MeV electron beams generated by the Elekta Synergy linear accelerator (linac) for the field sizes of 6 × 6 cm^2, 10 × 10 cm^2, 14 × 14 cm^2, 20 × 20 cm^2, and 25 × 25 cm^2 at depths of 0.5 cm, 1.0 cm, 2.0 cm, and 5.0 cm respectively. These measurements were acquired using ionization chambers in water and diode detectors in Perspex. The acquired data was sent to CMS XiO treatment planning system for validation.

Results: In general, the dose distributions for both systems compared very well with uncertainties within recommended limits. The largest maximum difference in symmetry was 1.6 % for a 6 MV photon beam defined at 25 × 25 cm^2 field size. The largest maximum difference in flatness was 2.77 % for a 4 MeV electron beam defined at 10 × 10 cm^2 applicator size. The penumbra largest maximum difference was 1.708 cm for 8 MeV electron beam defined at 25 × 25 cm^2 applicator size, which was outside the recommended limit of 1.2 cm. The largest maximum difference in field size was 2.388 cm for a 6 MeV electron beam defined at 20 × 20 cm^2 applicator size, which was outside the recommended limit of 0.4 cm.

The largest maximum difference in percentage depth dose at 10 cm depth was 1.69 % for the 6 MV photon beam. The absolute dose output measurements showed a very good agreement between the two systems to a maximum percentage difference and highest standard deviation of -0.99 % and 0.69 % respectively for the 6 MV photon beam. Validation measurements showed an agreement to less than 1 % and 2 mm for percentage depth doses and beam profiles respectively.

Conclusion and recommendation: From the results obtained, it is evident that the profiler 2 scanning system can be used as a substitute for the 3D-water phantom beam data acquisitions during linear accelerator commissioning. The future work based on this study could be to study the limitations involved with the profiler 2 scanning system when used during measurements for commissioning of a linear accelerator. Limitations like field size (maximum field size of 20×30 cm^2 at SSD = 100 cm), number of Perspex slabs to be used on top of the profiler 2 scanning system and diagonal profile measurements.

TABLE OF CONTENTS

Declaration *i*

Acknowledgements *ii*

Abstract *iii*

Table of Contents *v*

List of Acronyms *viii*

CHAPTER 1: INTRODUCTION 1

1.1. Overview. 1

1.2. Research question of the study. 4

1.3. Aim of the study. 4

1.4. The objectives of the study. 4

1.5. The scope of the study. 4

CHAPTER 2: LITERATURE REVIEW 6

CHAPTER 3: BASIC PRINCIPLES OF RADIATION PHYSICS 12

3.1. Overview. 12

3.2. Production of X-rays. 12

3.3. Photon interactions. 15

3.3.1. Photoelectric effect. 16

3.3.2. Coherent (Rayleigh) scattering . 17

3.3.3. Compton scattering effect. 18

3.3.4. Pair production. 20

3.4. Electron interaction. 21

3.4.1. Rate of energy loss. 22
3.5. Absolute dosimetry. 23
3.6. Protocols. 25
3.7. Statistical analysis. 27
3.8. Characterization of the linear accelerator beam. 28

CHAPTER 4: MATERIALS AND METHODS 32

4.1. Equipments. 32
4.1.1. Linear accelerator. 32
4.1.2. 3D-water phantom. 33
4.1.3. Ionization chambers. 34
4.1.4. Electrometer. 35
4.1.5. Profiler 2 Scanning system. 36
4.1.6. CMS XiO Treatment Planning System. 38
4.2. Beam data acquisition. 38
4.2.1. 3D-water phantom measurements. 38
4.2.2. Profiler 2 scanning system measurements. 42
4.2.3. Absolute dose measurements in water. 47
4.2.4. Absolute dose measurements with profiler 2 scanning system. 48
4.3. Beam modeling. 49

CHAPTER 5: RESULTS AND DISCUSSIONS 50

5.1. Overview. 50
5.2. Characterization of profiles and PDDs. 50
5.3. Photon beams. 53
5.3.1. Profiles for 6 MV photon beam. 53
5.3.2. Profiles for 15 MV photon beam. 56
5.3.3. PDDs for 6 MV photon beam. 59
5.3.4. PDDs for 15 MV photon beam. 60

5.4. Electron beams. 61
5.4.1. Profiles for electron beams. 61
5.4.2. PDDs for electron beams. 69
5.5. Analysis of tables. 72
5.6. Validation of beam data. 79
5.6.1. Photon beams (profiles). 80
5.6.2. Photon beams (PDDs). 81
5.6.3. Electron beams (profiles). 82
5.6.4. Electron beams (PDDs). 84
5.7. Absolute dose comparisons 85

CHAPTER 6: CONCLUSION AND RECOMMENDATIONS 88

REFERENCES 90

APPENDICES 100

APPENDIX A-1: List of figures 100
APPENDIX A-2: List of pictures 104
APPENDIX A-3: List of tables 104

LIST OF ACRONYMS

CMS = Computer Medical Systems.

NXEGS = Neutron and X-ray Electron Gamma Shower.

RW3 = Acrylic slab phantom.

MU = Monitor Unit.

Z = Atomic number.

RTD = Real Time Dosimetry.

QA = Quality Assurance.

SCD = Source Chamber Distance.

Prof 2 = Profiler 2.

3DWP = 3D-water phantom.

TPS = Treatment planning system.

PDDs = Percentage depth doses.

PDD_{10} = Percentage depth dose at 10 cm depth.

Linac = Linear accelerator.

cm = centimeters.

MV = Megavoltage.

MeV = Mega electron voltage.

RT = Radiation Therapy.

IMRT = Intensity Modulated Radiotherapy.

TPR = Tissue phantom ratio.

VMAT = Volumetric Modulated Arch Therapy.

CT = Computed Tomography.

MRI = Magnetic Resonance Imaging.

DP = Dose profiles.

MLC = Multileaf collimator.

keV = kiloelectron voltage.

SSD = Source Surface Distance.

DC = Direct current.

EPID = Electronic portal imaging device.

CHAPTER 1

INTRODUCTION

1.1. Overview.

The linear accelerator (linac) is a device that uses high-frequency electromagnetic waves to accelerate charged particles such as electrons and photons to high energies through a linear tube. The device is widely used for photon and electron radiation therapy. Consider the following block diagram (figure 1.1) showing the important components of a linear accelerator.

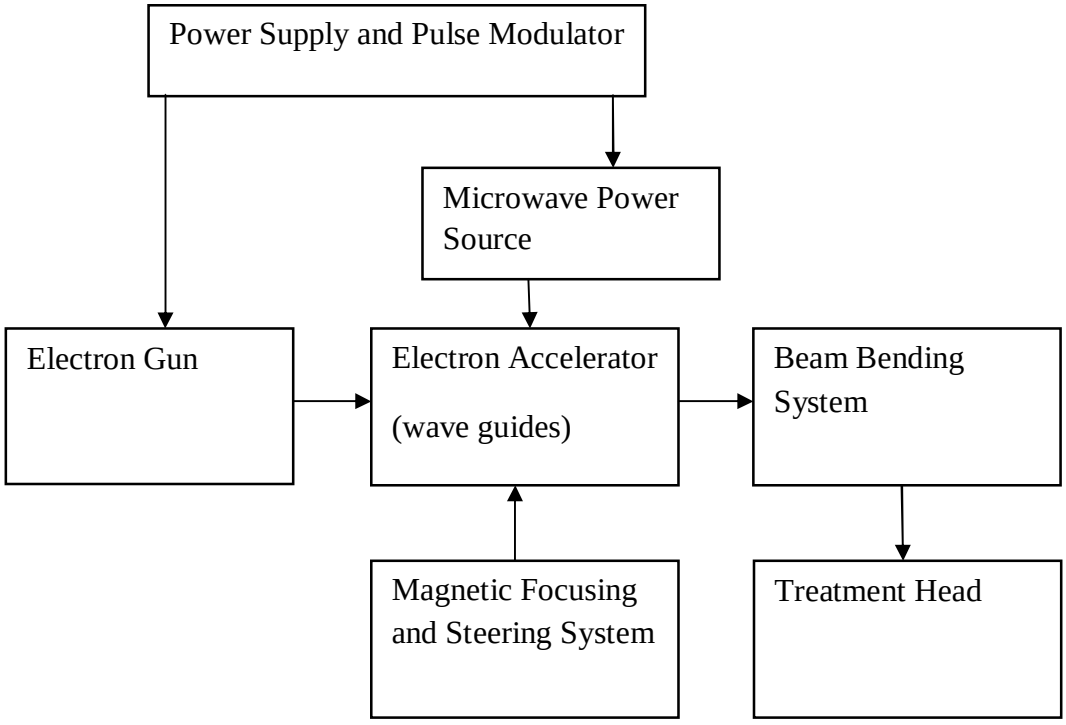

Figure 1.1: Block diagram of a linear accelerator.

The linac accelerates electrons either by travelling or stationary electromagnetic waves of frequencies in the microwave region of approximately 3000 megacycles/second. The power supply provides direct current (DC) to the modulator which forms high voltage pulses which are

simultaneously delivered to the magnetron/klystron and the electron gun (Khan F. M. 2003). The magnetron/klystron then produces pulsed microwaves which are injected into the accelerator tube. The electrons with the initial energy of about 50 keV interact with the electromagnetic field of the microwaves of the tube, which causes them to be accelerated to higher megavoltage energy regions. The high energy electrons emerge from the exit window of the accelerator tube in a form of a pencil beam approximately 3 mm in diameter to the treatment head (Podgorsak E. B. 2003, Khan F. M. 2005). Depending on the energy, it either emerges as a straight or bent beam using bending magnets, focusing coils and other components of the beam transport system. The linac head contains a number of important components relating to photon and/or electron treatment options as shown in figure 1.2.

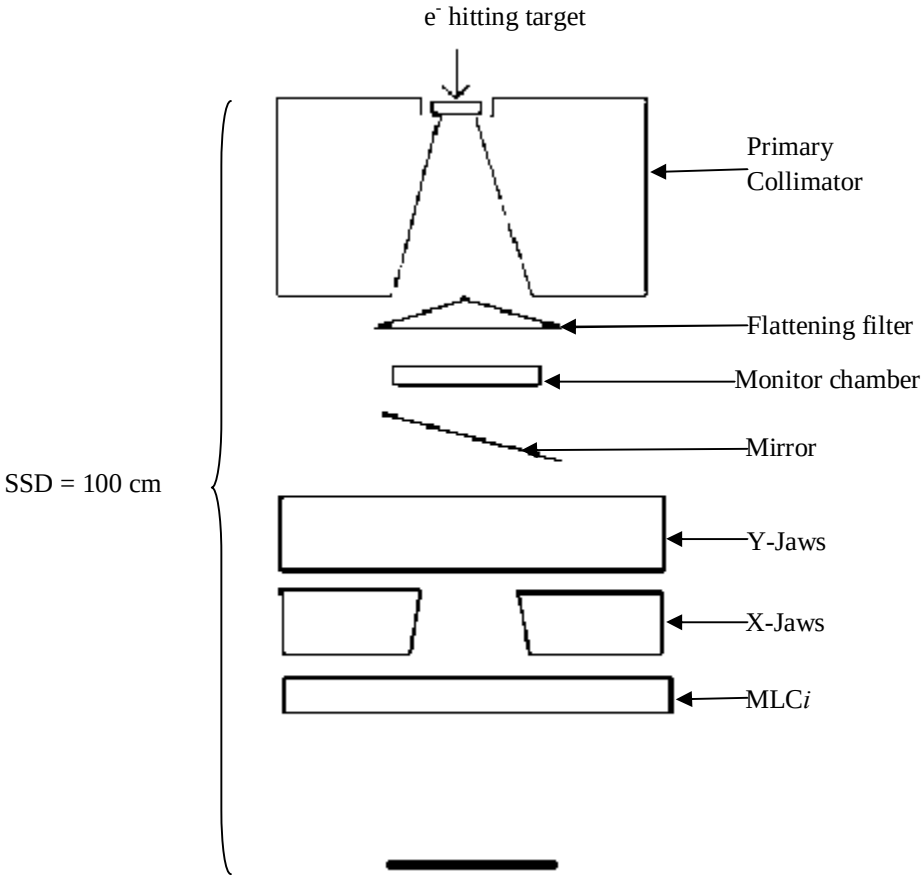

Figure 1.2: Typical linear accelerator head (Ding G. X. 2003).

A primary collimator is located adjacent to the target and its pyramidal or conical aperture defines the maximum field size, further delineated for photon therapy by a variable collimator (Karzmark C. J. and Pering N. C. 1973). The target material is tungsten which produces X-rays when electron beam interacts with it. The flattening filter is used to make the radiation beam intensity uniform across the field. The monitor chambers are used to monitor the dose rate, integrated dose and field symmetry. The mirror is used to project a light beam as if it emits from the photon focal spot, and thus the light field and radiation field are congruent. The *X* and *Y* jaws are used to define the field sizes. The Multi Leaf Collimators are used to define the field of both regular and irregular shapes (Khan F. M. 2003).

There are two modes of beam transport system for the linac which are:

Electron mode: The photon flattening filter and field light mirror are usually removed from the beam. The electron therapy beam is brought out of the evacuated structure through a thin window to minimize scattering and energy loss. After leaving the accelerator tube, the electron beam is made to strike the electron scattering foil which spreads the beam and gives uniform fluence across the treatment field. After the scattering foil, the beam is then incident on transmission monitoring ionization chambers whose primary functions are to monitor radiation dose produced by the beam. After passing the ionization chambers, the beam is further collimated by continuously movable collimators. The electron beam is further shaped by an external electron applicator attached to the treatment head. Collimation of the beam is necessary to limit its size and to protect surrounding healthy tissues (Khan F. M. 2005).

Photon mode: A beam flattening filter is provided externally in the treatment head. The treatment head also contains the field size and SSD optical systems. The output of the machine is again monitored by transmission ionization chambers which are thin walled when electrons are used so as to minimize X-ray contamination and reduction in electron energy (Khan F. M. 2005).

1.2. Research question of the study.

Setting up a 3D-water phantom is a tedious and time consuming procedure, which requires a lot of effort in filling the tank with water, aligning it with spirit level, lifting it to the required distance, performing a quality assurance associated with it, which can take up to an hour to two hours, as well as the fact that it takes about 10 minutes at most just to scan one profile. Thus the question is can the profiler 2 scanning system be used as a substitute for the 3D-water phantom for linear accelerator commissioning since it is easy to setup, assemble and requires less effort, and one profile can be scanned in a matter of seconds.

1.3. Aim of the study.

The aim of this study was to determine whether the profiler 2 scanning system can be used as a substitute for the 3D-water phantom used during linear accelerator commissioning.

1.4. The objectives of the study.

- To compare the photon and electron beam dose distributions measured with the 3D-water phantom with those measured with the profiler 2 scanning system (Marshall M. G. 1992, Woo M. *et al* 2003).
- To compare the absolute dose measurements for both systems for all beam energies of an Elekta Synergy Platform linear accelerator.
- To validate the dose distributions by modeling the 3D-water phantom beam data acquired on CMS XiO treatment planning system and compared the modeled data with both profiler 2 scanning system data and the 3D-water phantom data.

1.5. The scope of the study.

This chapter provided an overview of the work. A literature review on the equipments used, the 3D-water phantom, profiler 2 scanning systems, comparison of dose distributions and dose validation by treatment planning system are discussed in chapter 2 and chapter 3. The parameters

that influences the photon and electron therapy, a review on basic principles of radiation physics are discussed in this sections. Dosimetric quantities of a linear accelerator and statistical analysis on absolute dose determination are further discussed in chapter 3. Chapter 4 deal with the characterization of the materials to be used for this study (linear accelerator, 3D-water phantom, profiler 2 scanning system and CMS XiO treatment planning system), with XiO being used to validate data. In addition, the methodologies followed to acquire beam data (percentage depth dose curves, profiles and absolute dose measurements) are presented. Results and discussions on the beam data measurements between the two scanning systems (3D-water phantom and profiler 2 scanning system (Perspex block)) and CMS XiO treatment planning system are dealt with in chapter 5. The summary, conclusion and future recommendations are presented in chapter 6.

CHAPTER 2

LITERATURE REVIEW

Radiation therapy or radiotherapy is also called radiation oncology. There are two goals of radiation treatment, which are: (i) to control the malignancy and (ii) to avoid unacceptable damage to normal tissues. Radiotherapy may be used for curative or adjuvant treatment. It is used as palliative treatment (where cure is not possible and the aim is for local disease control or symptomatic relief) or as therapeutic (where the therapy has survival benefit and it can be cured). Radiotherapy has several applications in non-malignant conditions such as the treatment of trigeminal neuralgia, severe thyroid, eye disease, pterygium, pigmented villonodular synorictics, prevention of keloid scar growth and prevention of heterotypic ossification (Podgorsak E. B. 2003; Khan F. M. *et al* 2005). The use of radiotherapy in non-malignant conditions is suited partly by worries about the risk of radiation-induced cancers (Podgorsak E. B. 2003).

It is common to combine radiotherapy with surgery, chemotherapy, hormone therapy, immunotherapy or some mixture of the four. Most common cancer types can be treated with radiotherapy in some way. The precise treatment intent (curative, adjuvant, neo-adjuvant, therapeutic or palliative) will depend on the tumor type, location and stage and the general health of the patient (Podgorsak E. B. 2003, Khan F. M. *et al* 2005). In radiation therapy the radiation fields may also include the draining lymph nodes if they are clinically or radiologically involved with tumor, or if there is a thought to be a risk of subclinical malignant spread (Podgorsak E. B. 2003).

Medical Physicists in radiation therapy departments are always faced with many challenges including the need for precision, a variety of testing methods, data validation, lack of standards and time constraints. It is thus vital that the beam data acquired should be of high quality to avoid dosimetric and patient treatment errors that may subsequently lead to poor radiation outcome. Therefore one often needs to compare two dose distributions. Especially with the wide clinical implementation of IMRT, software tools for quantitative dose (or fluence) distribution

comparison are required for patient-specific quality assurance. Dose distribution comparison is not a trivial task since it has to be performed in both dose and spatial domains in order to be clinically relevant. Each of the existing comparison methods has its own strengths and weaknesses and there is a room for improvement (Jiang S. B. *et al* 2006).

Generally 3D-dose distributions obtained from TPS have to be verified by dosimetric methods as stated by Saminathan S. *et al* (2010). They also compared two-dimensional results calculated and measured in several coplanar planes to within 3 % and 3 mm criteria. Both J. A. and Pawlicki T. (2004) have also reported an agreement to confidence level of 3 % and 3 mm when comparing dosimetric data between physical measurements and the Monte Carlo NXEGS simulations when commissioning the electron beams. In principles there are many possibilities to measure two-dimensional dose distributions such as films, flat-panel EPIDs, ion chambers and ionization chamber arrays, and radiographic and radiochromic films. Saminathan S. *et al* (2010) showed that the EPIDs give a good resolution and offer a possibility for real-time measurements.

A good agreement between the 2D-plastic scintillation detectors (PSDs) array was demonstrated by Guillot M. *et al* (2010), the matrix ion chamber array and the Pinnacle 3 treatment planning system dose distributions, and also demonstrated that the dose distributions in the irradiated volume of the 2D-plastic scintillation detectors is not modified by the presence of hundreds of scintillation detectors. These plastic scintillation detectors are characterized by a unique set of properties including high spatial resolution, angular independence, energy independence and real-time readout.

The dose distribution comparison is always achieved by comparing the following beam data:
(i). Central axis depth dose tables which are percentage depth dose tables and tissue phantom ratios which may be prepared manually by interpolation of measured data or generated by computer software (Khan F. M. 2005).
(ii). Isodose curves whereby the measured and computer generated data should agree to within ± 2 % in the central part of the field (e.g. up to about 1 cm inside the field edge) and about 2 mm in the penumbra (e.g. between 90 % and 20 % decrement lines), with the same criteria applying

to wedged isodose curves except that the computer algorithms are not as accurate near the edges of the wedges as stated by Khan F. M. (2010).
(iii). Monitor Unit Calculations which is required as part of commissioning as stated by Klemp P. F. B. *et al* (1988), Chang P. S. *et al* (1993) and Sharma S. C. *et al* (2007).

There are different methods or tools that were developed to quantitatively compare dose distributions, either measured or calculated, one of those methods being the γ-tool. Before computing γ, the dose and distance scales of the two distributions referred to as evaluated and referenced, are normalized by dose and distance criteria. The renormalization allows for dose distribution comparison to be conducted simultaneously along dose and distance axes. In typical clinical use, the fraction of points that exceeds 3 % or 3 mm can be extensive, thus typical a 5 % or 2-3 mm is used in clinical evaluations. A limitation with the dose difference test is that it becomes overly sensitive in steep dose gradient regions. The small spatial offsets between the two distributions caused by experimental error yield identical dose distributions to exhibit large dose difference in regions of steep dose gradients. Thus the usefulness of dose distributions is strongest in regions of relatively shallow dose gradients (Low D. A. *et al* 2003).

The process of radiation therapy is complex and involves many steps. Numerous phantoms have been developed in order to compare doses calculated by planning systems to actual doses measured. Howlett S. *et al* (1999) used an anthropomorphic dose measurement phantom for showing variation in the measured and calculated dose for 3D system in heterogeneous conditions, whilst Kilic A. *et al* (2002) have used the RW3 solid water phantom and wellhofer 3D-water phantom to check the radiotherapy treatment planning systems data with measurements under homogeneous density conditions.

Modern radiation therapy has advanced considerably in the recent decades through the development of conformal techniques that better shape the high dose to tumor volumes while minimizing the dose to the surrounding normal tissue. Techniques such as IMRT and VMAT are available, where the intensity within a radiation field is varied dynamically during treatment, and thus sophisticated dose painting is enabled. The rapid pace of these developments and significant increase in the associated complexities, have introduced considerable new challenges to the

radiation treatment team. This is particularly true for the clinical medical physicist, whose role is to ensure the correct delivery of radiation dose for patientôs treatment. The challenges for patient treatment verification have motivated the development of sophisticated strategies, tools and equipments to measure dose and to analyze the measurements so that the physics team can assess safe delivery of dose to patients. Point dosimeters such as ionization chambers, thermoluminescent dosimeters and diodes have been used for decades to commission treatment units, to calibrate output and to verify dose delivery at single points in a phantom. The 2D dosimetry techniques such as silver-halide and radiochromic film or digital systems incorporating flat panel arrays of ionization chambers or diodes that are often used in IMRT delivery validation, and the full 3D dosimeters such as scintillator detector array or volumetric chemical dosimeters probed by MRI or by radiographic examination and optical computed tomography techniques for IMRT and VMAT have been used (Fogliata A. *et al* 2007, Schreiner L. J. *et al* 2011). The accuracy of radiation therapy has been discussed previously which showed that errors in the dose delivery should not exceed 5 % (Amin E. *et al* 2001).

The dose distribution in a medium traversed by a photon for the recommended beam depends on beam energy, field size and the medium nature (Rafaravavy R. *et al* 2007). For the energy considered in radiotherapy, Compton Effect is the main interaction in tissue. The percentage depth doses and dose profiles will be established to study these distributions (Elder P. J. *et al* 1995, Rafaravavy R. *et al* 2007). This will be achieved with the use of ionization chambers and array of diode detectors.

Advances in computer technology have led to the availability of sophisticated 3D-treatment planning systems for use in many radiotherapy centers. One aim of introducing such TPSs is to improve the accuracy of dose calculations in radiotherapy planning (ICRU Report 42 1987).
Many optimization functions and methods including gradient methods and stochastic optimization methods to solve dose distribution problems in radiotherapy planning have been used (ICRU Report 42 1987, Wu X. *et al* 2001). Two types of cost functions, deterministic models that are based on radiobiological effects or dose criteria and probability models that are similar to the maximum likelihood estimations have been successfully applied to radiotherapy planning (ICRU Report 42 1987, Xing L. *et al* 1999).

STATDOSE is an interactive computer program for 3D dose analysis and plotting 1D dose distributions using the *xvgr/xmgr* plotting package. 3D dose data such as those generated using the EGS4 user-code DOSXYZ developed at NRCC for OMEGA project are examples of typical dose data. STATDOSE functions include normalization, re-binning, plotting and analysis of the dose distributions. Distributions can also be compared both statistically and graphically. Graphs to aid in statistical analysis of the distributions as well as both cross-plots and depth-doses are provided by STATDOSE (McGowan H. *et al* 2007). Siantar C. L. H. *et al* (1999) used the PEREGRINE Monte Carlo system to compare the dose distributions between the 3D-water phantom and Scanditronix photon diode detectors and found a good agreement between the systems. The PEREGRINE Monte Carlo dose calculation system is designed to provide Monte Carlo transport calculations for photon beams, electron beams and neutron beams fast enough for day-to-day radiation therapy planning. It operates on low-cost, commodity hardware, enables real time visualization of the dose as it is simulated and completes a full treatment simulation in minutes (Saintar C. L. H. *et al* 1999). Although in our study the algorithms within the TPS (CMS XiO) as well as excel generated data will be used for data analysis.

The CMS XiO 3D-TPS system is based on the pencil beam model, where physical quantities such as profiles and percentage depth dose curves are estimated using conventional method. The photon dose calculation model in this TPS system is based on convolution, superposition and Clarksonôs algorithms (Elder P. J. *et al* 1995).The mono-energetic depth doses, calculated with convolution method from Monte Carlo generated point spread functions (PSF), are added to yield the pure photon depth dose distributions (Amin E. *et al* 2001). The poly-energetic pencil-beam is then used to calculate the dose distribution for a given case by convolution with the machine specific energy-fluence matrix modulated by the actual field shape (Amin E. *et al* 2001). One of the features of the system is that it calculates the monitor settings for the planned fields (Amin E. *et al* 2001). As stated by Alber M. *et al* (2008), one of the interesting tools of dose distributions comparison is to compare the absolute value of absorbed dose. The dose difference can be expressed in so many ways but generally the absolute value of dose is used. This difference is normalized to the dose having a specific value, for instance the prescribed dose, the maximum dose or the dose on the beam axis at the same depth. Starkschall G. *et al*

(2000) reported calculated relative doses that matched measured relative doses in water phantom for field sizes from 4 × 4 cm^2 to the largest field size available to 0.5-1 % along the central axis and 2 % along off-axis beam profiles while commissioning the 3D convolution/superposition photon dose algorithm. Thus in this study absolute dose differences will be compared for the 3DWP and the Prof 2 scanning system. Because there is a need to check consistency of beam outputs and energy of the linear accelerator, Ravichandran R. *et al* (2007) have reported the dose/MU for all radiation beams of Varian Clinac 600 CD and Clinac 2300 CD to within 2 % accuracy measured over a period of 30 months. In our study the dose measurements comparisons were performed over a period of 3 months to establish the agreement between the 3DWP measurements and the profiler 2 scanning system dose measurements.

CHAPTER 3

BASIC PRINCIPLES OF RADIATION PHYSICS

3.1. Overview.

In this chapter the production of X-rays, photons and electrons will be discussed as well as the interaction processes which may occur when ionization radiation interacts with matter. The determination of absorbed dose, statistical analysis and characterization of the linear accelerator beam will also be included.

3.2. Production of X-rays.

X-rays were discovered by Wilhelm Conrad Roentgen on November 8, (1895) while studying cathode rays (stream of electrons) in a gas discharge tube (Johns H. E. *et al* 1983, Thomas S. C. III. *et al* 1990). The discovery was that another type of radiation was produced during interaction of electrons with glass walls of the tube that could be detected outside the tube and can penetrate opaque substances, produce fluorescence, blacken a photographic plate, and ionize gas, and this was named X-rays (Johns H. E. *et al* 1983, Thomas S. C. III. *et al* 1990, Khan F. M. 2003).

The X-ray Tube.

Consider the following figure, which is a schematic representation of a conventional X-ray tube.

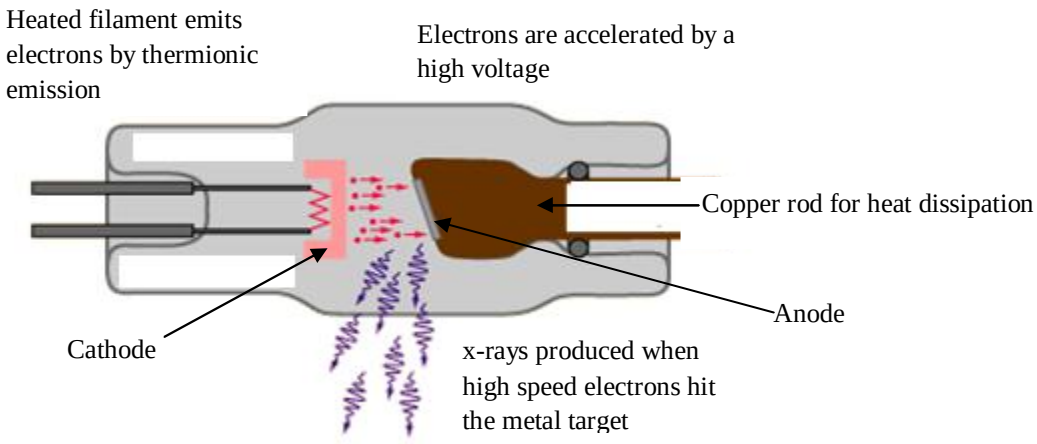

Figure 3.1: Therapy X-ray tube with hooded anode (Nave C. R. *et al* 2000).

The tube consist of a glass envelope which has been evacuated to high vacuum. At the one end is a *cathode* (negative electrode) and the other an *anode* (positive electrode) (Johns H. E. *et al* 1983, Thomas S. C. III. *et al* 1990, Khan F. M. 2003).

The tungsten (*anode* design-rotating to reduce the temperature of the target at any one spot) is the choice of target material because of its high atomic number and high melting point to withstand intense heat produced in the target by the electronic bombardment (Johns H. E. *et al* 1983, Thomas S. C. III. *et al* 1990, Khan F. M. 2003).

The *cathode* consists of a wire filament (a circuit to provide filament current) and a negatively charged focusing cup (Johns H. E. *et al* 1983, Thomas S. C. III. *et al* 1990, Khan F. M. 2003). The electrons produced by the cathode bombard the anode and x-rays are produced. This process gives rise to *bremsstrauhlung x-rays* and *characteristic x-rays*. The process of *bremsstrahlung* (breaking radiation) is the results of radiative ñcollisionò (interaction) between high speed electron and the nucleus.

The electron while passing near a nucleus may be deflected from its path by action of Coulomb forces of attraction and lose energy as bremsstrahlung.

Figure 3.2: Bremsstrahlung process (Nave C. R. *et al* 2000).

As the electron, with its associated electromagnetic field passes in the vicinity of the nucleus, it suffers sudden deflection and acceleration, as a results part of its energy is dissociated from it and propagates in space as electromagnetic radiation. This process is illustrated in figure 3.2. Thus the resulting bremsstrahlung photon may have any energy up to its initial energy of electron (Johns H. E. *et al* 1983, Thomas S. C. III. *et al* 1990, Khan F. M. 2003, Podgorsak E. B. 2003). The process of *characteristic x-rays* production is also achieved from interaction of an electron with matter and some of the electrons are knocked out of their shells by a process called inner-shell ionization as shown in figure 3.3 (Johns H. E. *et al* 1983, Podgorsak E. B. 2003).

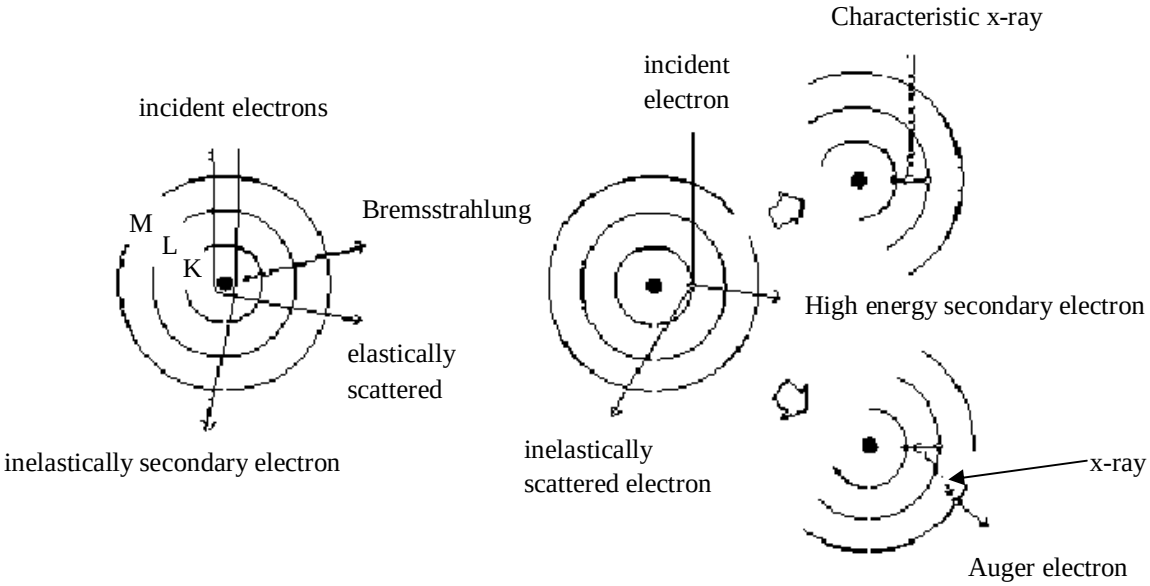

Figure 3.3: The production of characteristic x-rays (Nave C. R. *et al* 2000).

An incident electron with kinetic energy E_0, may interact with the atoms of the target by ejecting an orbital electron (elastically scattered electron) such as a K, L, or M electron leaving the atom ionized. The original electron (in-elastically scattered electron) will recede from the collision with energy of $E_0 - \Delta E$, where ΔE is the energy given to the orbital electron (Khan F. M. 2003, Barkla C. G. *et al* 1997). As part of ΔE is spent in overcoming the binding energy of the electron and the rest is carried by ejected electron. When the vacancy is created in the orbit, an outer orbital electron will fall down to fill that vacancy and in so doing, the energy is radiated in the form of electromagnetic radiation, and thus this is called characteristic radiation (Johns H. E. *et al* 1983, Thomas S. C. III. *et al* 1990, Khan F. M. 2003).

3.3. Photon interactions.

When a photon beam passes through matter, some of the photons interact with atoms of the material and they are attenuated, scattered or transmitted. The attenuation of photons in matter is described by the following equation in a homogenous medium (Podgorsak E. B. 2003).

$$I_x = I_0 e^{-\mu(hv,Z)x} \qquad (3.1)$$

where I_x is the intensity of a narrow monoenergetic photon beam.
I_0 is the initial intensity of the unattenuated beam.
$\mu\ (hv, Z)$ is the linear attenuation coefficient, which depends on photon energy hv and attenuator atomic number Z.
x is the thickness of the attenuator.

The half value layer (HVL or $x_{1/2}$) is defined as that thickness of the attenuator that attenuates the photon beam intensity to 50 % of its original value:

$$HVL = \frac{\ln 2}{\mu} \qquad (3.2)$$

Similarly, the tenth-value layer (*TVL or* $x_{1/10}$) is defined as the thickness of the attenuator that attenuates the photon beam intensity to 10 % of its original value:

$$TVL = \frac{\ln 10}{\mu} \qquad (3.3)$$

The mass attenuation coefficient μ_m, atomic attenuation coefficient ${}_a\mu$ and electronic attenuation coefficient ${}_e\mu$ are proportional to the linear attenuation coefficient μ through the following relationship (Podgorsak E. B. 2003): N_A

$$\mu = \rho\mu_m = \frac{\rho NA}{A}{}_a\mu = \frac{\rho NAZ}{A}{}_e\mu \qquad (3.4)$$

where ρ, Z and A are the density, atomic number and atomic mass number, respectively for the attenuator.

Photons may undergo various possible interactions with the atoms of an attenuator; the probability or cross-section for each interaction depends on the energy hv of the photon and on the atomic number Z of the attenuator (Johns H. E. *et al* 1983, Thomas S. C. III. *et al* 1990, Podgorsak E. B. 2003, Khan F. M. 2003).

3.3.1. Photoelectric effect.

The photoelectric effect is a phenomenon in which a photon interacts with an atom and ejects one of the orbital electrons from the atom as shown in figure 3.4 (Johns H. E. *et al* 1983, Khan F. M. *et al* 2003).

$$\mathbf{E_{photon}} = \boldsymbol{hv}$$

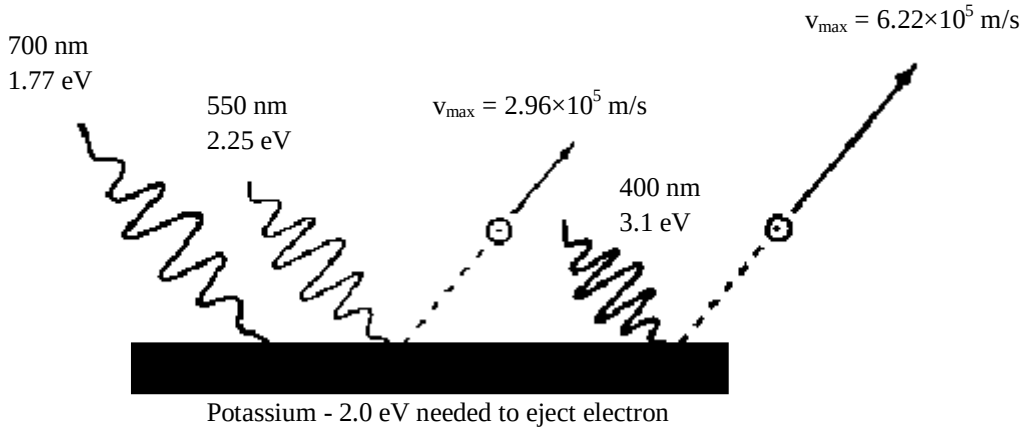

Figure 3.4: The process of photoelectric effect (Nave C. R. *et al* 2000).

The photon interacts with a tightly bound orbital electron of the attenuator and disappears, while the orbital electron is ejected from the atom as a photo-electron with kinetic energy E_K given as (Thomas S. C. III. *et al* 1990, Podgorsak E. B. 2003):

$$E_K = hv - E_B \qquad (3.5)$$

where hv is the incident photon energy and E_B is the binding energy of the electron.

This type of interactions can take place with electrons in the K, L, M, or N shells (Johns H. E. *et al* 1983, Khan F. M. 2003). After the electron has been ejected from the atom (attenuator), a vacancy is created in the shell, thus leaving the atom (attenuator) in an excited state. This vacancy can be filled by an outer orbital electron with the emission of characteristic x-rays (Thomas S. C. III. *et al* 1990, Khan F. M. *et al* 2005).

3.3.2. Coherent (Rayleigh) scattering.

The coherent (Rayleigh) scattering is a process whereby, like photoelectric effect, the photon interacts with the bound orbital electron (i.e. with the combined action of the whole atom). This process is visualized by considering the wave nature of electromagnetic radiation (Podgorsak E. B. 2003, Khan F. M. *et al* 2005).

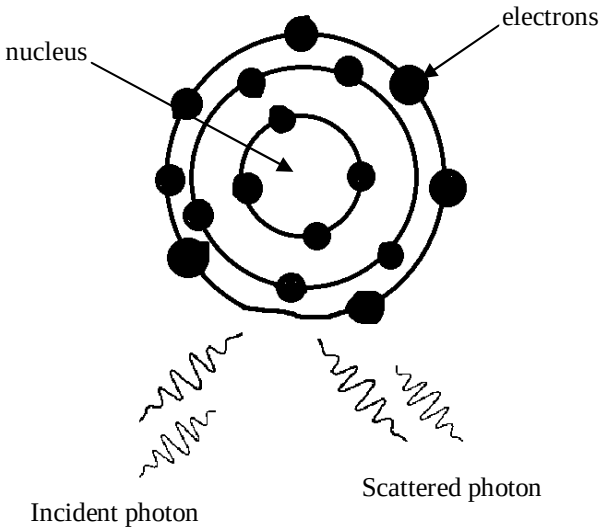

Figure 3.5: The process of coherent scattering (Nave C. R. *et al* 2000).

An electromagnetic wave passes near the electron and setting it into oscillation. The oscillating electron re-radiates the energy at the same frequency as the incident electromagnetic wave. In this process, the scattered photon has the same wavelength as the incident photon and there is no energy transfer (elastic interaction). The coherent scattering is probable in high atomic number materials and with photons of low energy (Khan F. M. 2003, Podgorsak E. B. 2003). This process is shown in figure 3.5.

3.3.3. Compton scattering effect.

The Compton scattering (incoherent) effect represents a photon interaction with essentially free and stationary (i.e. the binding energy of the electron is much less than the energy of the bombarding photon) orbital electron as illustrated by figure 3.6.

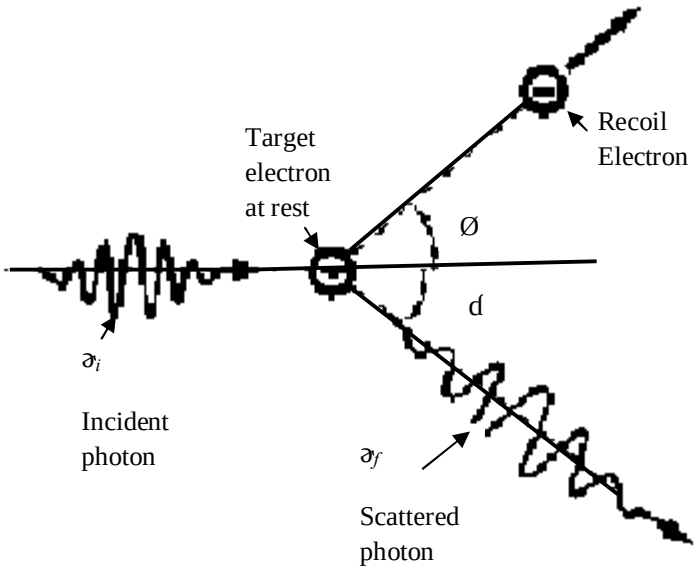

Figure 3.6: The Compton effect (Simpson and John J. 2000).

In this interaction the electron receives some energy from the photon and is emitted at an angle (θ). The incident photon energy *hv* is much larger than the binding energy of the orbital electron. The photon with reduced energy is then scattered at an angle (θ) (Khan F. M. 2003). The Compton process can be analyzed in terms of a collision between two particles, a photon and an electron. By applying the laws of conservation of energy and momentum, the following relationships can be derived:

$$E = hv\frac{\alpha(1-\cos\theta)}{1+\alpha(1-\cos\theta)} \tag{3.6}$$

$$hv' = hv\frac{1}{1+\alpha(1-\cos\theta)} \tag{3.7}$$

$$\cos\theta = \frac{(1+\alpha)\tan\theta}{2} \tag{3.8}$$

where *hv, hv'*, and *E* are the energies of the incident photon, scattered photon, and electron, respectively and

$$\alpha = \frac{hv}{m_0 c^2} \tag{3.9}$$

where m_0c^2 is the rest energy of the electron (0.511 MeV).
α is the ratio of the incident photon and the electron energy.
c^2 is the square of the speed of light.

The Compton scattering effect can make three different hits on an electron: (i) a *direct hit* (when a photon makes a direct hit with the electron and the electron travel forward (θ=0°) the scattered photon travels backwards (θ=180°) after the collision). (ii) a *grazing hit* (when an electron is emitted at right angles (θ=90°) and the scattered photon will go in forward direction (θ=0°)), and (iii) a *90° photon scatter* (when a photon is scattered at right angles to its original direction (θ=90°)) (Khan F. M. 2003).

3.3.4. Pair production.

This process occurs when the energy of the incident photon (hv) is greater than 1.02 MeV. In this process, the incident photon interacts strongly with the electromagnetic field of an atomic nucleus and gives up all its energy in the process of creating a pair consisting of a negative electron (e^-) and a positive electron (e^+). Since the rest mass energy of the electron is equivalent to 0.511 MeV, a minimum energy of 1.02 MeV is thus required to create these pair of electrons (Khan F. M. 2003).

Consider the following diagram illustrating the pair production process.

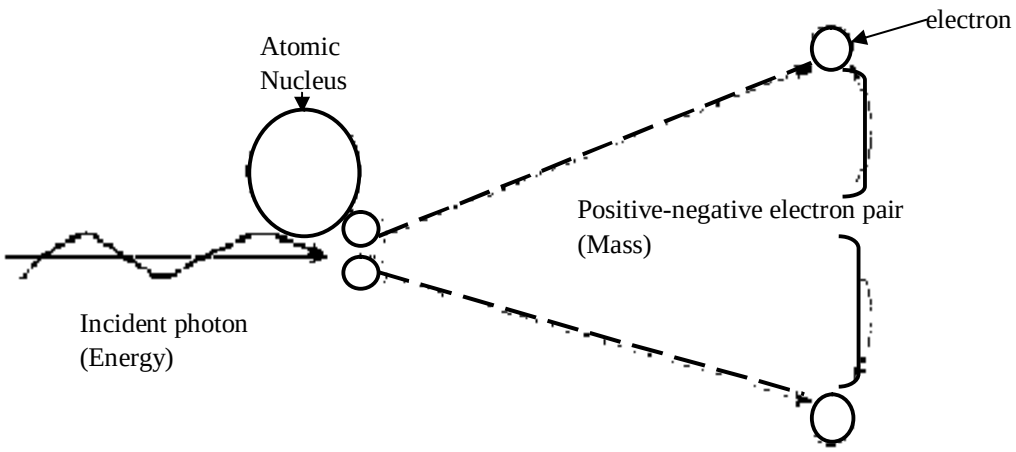

Figure 3.7: The Pair production process (Nave C. R. *et al* 2000).

3.4. Electron interaction.

An electron is the smallest negatively charged particle. Its charge (1.6×10^{-19} coulombs) is equal to that of a proton but opposite in sign (Bomford C. K. *et al* 1993). Electrons interact with matter by ionization, excitation (inelastic collisions with atomic electrons), and bremsstrauhlung (inelastic collisions with nuclei) processes which radiative collisions occur, and elastic collisions with atomic electrons and with nuclei. These interactions are mediated by Coulomb forces between the electric field of travelling particles and electric fields of orbital electrons and nuclei of atoms of the material. These electrons also suffer multiple scattering and change its direction because of their small mass without significant loss of energy (Khan F. M. 2003, Podgorsak E. B. 2003). In inelastic collisions, some of the kinetic energy is lost as it is used in producing ionization or converted to other forms of energy such as photon energy and excitation energy. In elastic collisions, kinetic energy is not lost although it may be redistributed among the particles emerging from the collision.

3.4.1. Rate of energy loss.

The total distance an electron travels in a medium before losing all its energy is referred to as its range and is determined by the initial energy of the electrons and the density of the medium. An electron traveling in a medium loses energy as a result of collisional and radiative processes. The rate of energy loss per gram per centimeter squared, which is called the mass stopping power, is greater for low atomic number (Z) materials than for high atomic number materials. This is due to high Z materials having fewer electrons per gram than low Z materials, and high Z materials have tightly bound electrons. The rate of energy loss per centimeter is approximately proportional to the electron energy and to the square of the atomic number (Z^2). The probability of radiation loss relative to the collisional loss increases with the electron kinetic energy and with Z. The total mass stopping power $\left(\frac{S}{\rho}\right)_{tot}$ of a material for charged particles is given in equation (3.10) (Khan F. M. 2003):

$$\left(\frac{S}{\rho}\right)_{tot} = \frac{dE}{\rho dl} \tag{3.10}$$

where S is the stopping power and dE is the total energy lost by particle in traversing a path length dl in the material of density ρ.

$$\left(\frac{S}{\rho}\right)_{tot} = \left(\frac{S}{\rho}\right)_{col} + \left(\frac{S}{\rho}\right)_{rad} \tag{3.11}$$

where $\left(\frac{S}{\rho}\right)_{col}$ and $\left(\frac{S}{\rho}\right)_{rad}$ apply to collisional losses and radiation losses, respectively (Khan F. M. 2003).

3.5. Absolute dosimetry.

When a photon beam passes through air, it produces excitation and ionization. The measure of the amount of ionization that occurs in air is then called exposure (X).

$$X = \frac{dQ}{dm} \qquad (3.12)$$

where dQ is the absolute value of the total charge of the ions of one sign produced in air when all the electrons liberated by photons in air of mass dm are completely stopped in air.
Absorbed dose ($\overline{D}$) is a non-stochastic quantity for all types of ionization radiation (directly and indirectly) including charged and uncharged particles, all materials and all energies defined as:

$$\bar{D} = \frac{d\bar{E}}{dm} \qquad (3.13)$$

where $d\bar{E}$ is the mean energy imparted by ionizing radiation to medium of mass dm (Khan F. M. 2003).

Kerma (K) is the kinetic energy released per unit mass of an absorber. It is also a non-stochastic quantity relating to indirectly ionizing radiation such as photons and neutrons. It is defined as:

$$K = \frac{d\bar{E}_{tr}}{dm} \qquad (3.14)$$

where $d\bar{E}_{tr}$ is the sum of the initial kinetic energies of all charged ionizing particles (electrons) liberated by uncharged particles (photons) in the medium dm (Podgorsak E. B. 2003). Due to finite range of the secondary electrons released through photon interactions, the transfer of energy (Kerma) from the photon beam and the absorption of energy by the medium (absorbed dose) do not take place at the same location.

The relationship between absorbed dose and Kerma is best described by the figures 3.8 and 3.9.

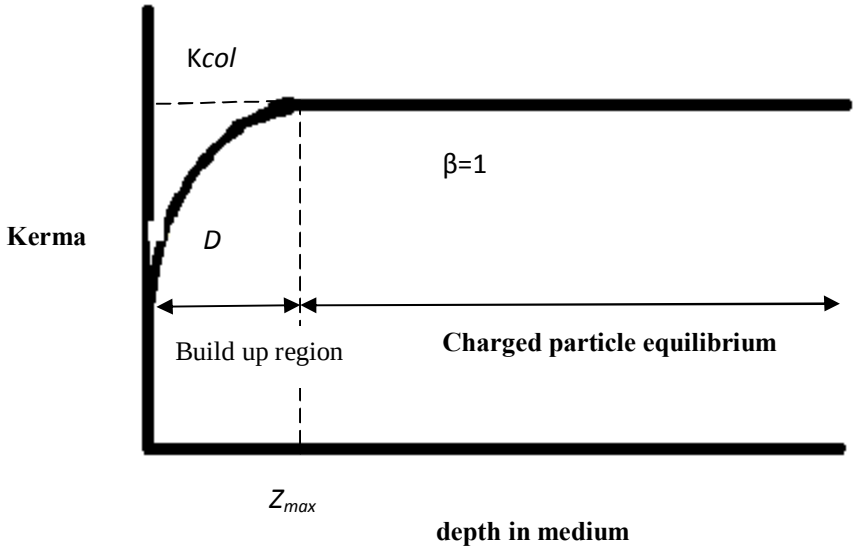

Figure 3.8: Relationship between collision Kerma and absorbed dose for ϐ=1.

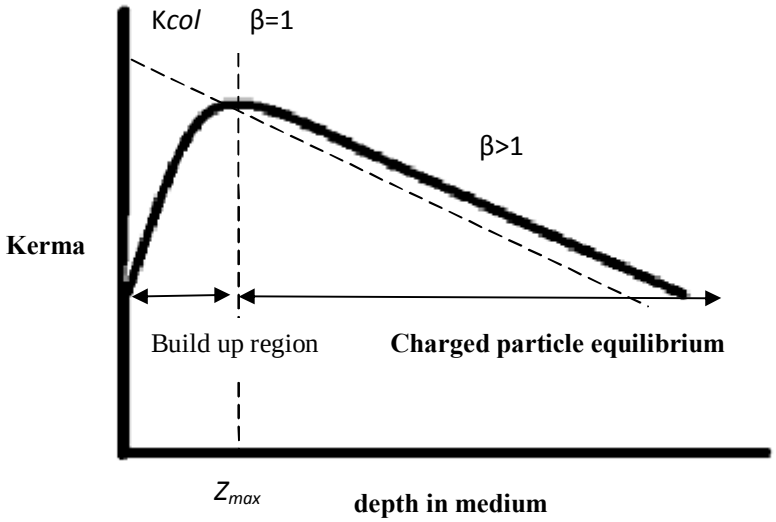

Figure 3.9: Relationship between collision Kerma and absorbed dose for ϐ=1 and ϐ>1.

As the high energy beam penetrates the medium, Kerma is maximal at the surface of the irradiated medium and this is because the particle fluence is greatest at the surface. Initially the charged particle fluence and absorbed dose increases as a function of depth until the depth of maximum dose (Z_{max}) is attained. If there was no attenuation or scattering, situation in figure 3.8

would occur and the electronic equilibrium is achieved. Since a radiation beam does undergo attenuation and scattering the situation in figure 3.9 is achieved when a constant relation between collision Kerma and absorbed dose exists. Collision Kerma and absorbed dose decreases constantly after the depth of maximum dose, but the absorbed dose curve is slightly above the Kerma curve. The buildup region in the absorbed dose curve is responsible for the skin sparing effect when high energy photon beams are used. The surface dose is due to the electron contamination in the beam.

The dose (D_{water}) in water at depth d_{water} is related to the dose (D_{med}) in solid medium at a corresponding depth d_{med}, provided secondary electron equilibrium exists (normally within a few millimeters of the surface) and energy spectra at each position are identical (TG-25 1991, Khan F. M. 2003) by:

$$D_{water}(d_{water}) = \frac{D_{med}(d_{med})\left[\left(\frac{S}{\rho}\right)_{col}\right]water}{\left[\left(\frac{S}{\rho}\right)_{col}\right]med}\theta \qquad (3.15)$$

where $\frac{\left[\left(\frac{S}{\rho}\right)_{col}\right]water}{\left[\left(\frac{S}{\rho}\right)_{col}\right]med}$ is the ratio of the mean unrestricted mass collision stopping power in water to that in medium and θ is the fluence factor.

In radiation therapy department, both high energy electrons and photons are used for the treatment of malignancies.

3.6. Protocols.

Several protocols were introduced previously for clinical reference dosimetry of external beam radiation therapy using photon beams with nominal energies between Co-60 and 50 MV and

electron beams with nominal energies between 4 and 50 MeV. Some of these protocols were used in this study. They were written by Task Group 21 (TG-21) and Task Group 51 (TG-51) of the Radiation Therapy Committee of the American Association of Physicists in Medicine (AAPM) and were formally approved by AAPM for clinical use. These were followed by Technical Report Series 277 (TRS-277), Technical Report Series 381 and lastly the Technical Report Series 398 (TRS-398) of the International Atomic Energy Agency (IAEA), which was introduced in 2001. The TG-21, TG-51, TRS-277 and TRS-381 protocols were based on the calibration factor in air (N_{gas}), whilst the TRS-398 is based on the calibration factor in water (N_{Dw})thus absorbed dose to water, since the quantity relates closely to the biological effects of radiation (TG-21, TG-51, TRS-277, TRS-381, TRS-398).

The TRS-398 was used for dosimetry measurements in this study, for both high energy electron beams and high energy photon beams. When a dosimeter is used in a beam of quality Q different from that used in its calibration, Q_0, the absorbed dose to water is given by:

$$D_{w,Q} = M_Q N_{D,w,Q} k_{Q,Q_0} \qquad (3.16)$$

where the factor k_{Q,Q_0} corrects the effects of the difference between the reference beam quality Q_0 and the actual user quality Q. The dosimeter reading M_Q has been corrected to the reference values of influence quantities (temperature and pressure), other than beam quality, for which the calibration factor is valid, and $N_{D,w,Q}$ is the absorbed dose calibration factor in water.

$$k_{Q,Q_0} = \frac{\left(S_{w,air}\right)_Q P_Q}{\left(S_{w,air}\right)_{Q_0} P_{Q_0}} \qquad (3.17)$$

which depends only on quotients of water to air stopping power ratios and perturbation factors at the beam quality Q and Q_0.

$$k_{TP} = \frac{(273.2+T)P_0}{(273.2+T_0)P} \qquad (3.18)$$

where T_0 and P_0 are temperature and pressure of the day respectively. T and P are the standard temperature and pressure (which are 22 ℃ and 1013 mbar respectively) with k_{TP} being the temperature and pressure correction factor applied to the dosimeter reading M_Q.

3.7. Statistical Analysis.

The statistical analysis was used to analyze the absolute dose measurements measured over a period of three months to determine the reliability and accuracy of the profiler 2 scanning system in measuring the dose. A common form of scientific experimentation is the comparison of two groups. This comparison could be of two different treatments, the comparison of treatment to control, or before or after comparison.

Every value of the variable differs from the sample mean by some specific amount which is called its deviation (Veer B. R. 2006, Indrayan A. 2006). The deviation (d) of an observation (X) is given by the following equation:

$$d = X - \bar{X} \qquad (3.19)$$

The *mean deviation* is an average mean of the deviations of values from the central tendency, which can either be arithmetic *mean, mode or median*. Therefore the mean deviation can be defined as the mean of all the deviations in a given set of data obtained from an average.

$$Mean\ Deviation\ (MD)\bar{x} = \frac{\sum\left(X - \bar{X}\right)}{N} \qquad (3.20)$$

where $\sum\left(X - \bar{X}\right)$ is a deviation of the mid value of the class from the population mean.

N is a total number of observations.

The *standard deviation* of a series is the positive square root of the arithmetic mean of the squares of deviations of the various items from the arithmetic mean of the series also called root mean square deviation (Veer B. R. 2006, Indrayan A. 2006).

This is given by a formula:

$$\sigma = \frac{\sqrt{\sum X^2}}{N} \qquad (3.21)$$

where σ is a standard deviation.

X is deviation obtained from actual mean.

N is a total number of observations.

The *variance* is the arithmetic mean of the squares of sum of the deviations from the mean value of the data (Veer B. R. 2006), which is given by the following formula:

$$Variance\ \sigma^2 = V = \frac{\sum\left(X - \bar{X}^2\right)}{n} \qquad (3.22)$$

where n is a number of degrees of freedom.

Therefore, the *coefficient of variance* is then given by:

$$CV = \frac{(s\tan dard\ deviation)}{Mean} \times 100 = \frac{\sigma \times 100}{\bar{X}} \qquad (3.23)$$

The coefficient of variation is a measure of relative dispersion.

3.8. Characterization of the linear accelerator beam.

Percentage depth dose curves and beam profiles can be measured by means of ion chambers, solid state detectors or radiographic films (Supply 25 B. J. R. 1996, Niroomand-Rad A. *et al* 1998, Podgorsak E. B. 2003, Khan F. M. 2003, Pai S. *et al* 2007). The beam profile is a measure of the variation of dose across the field.

A figure below shows the beam profile and its description:

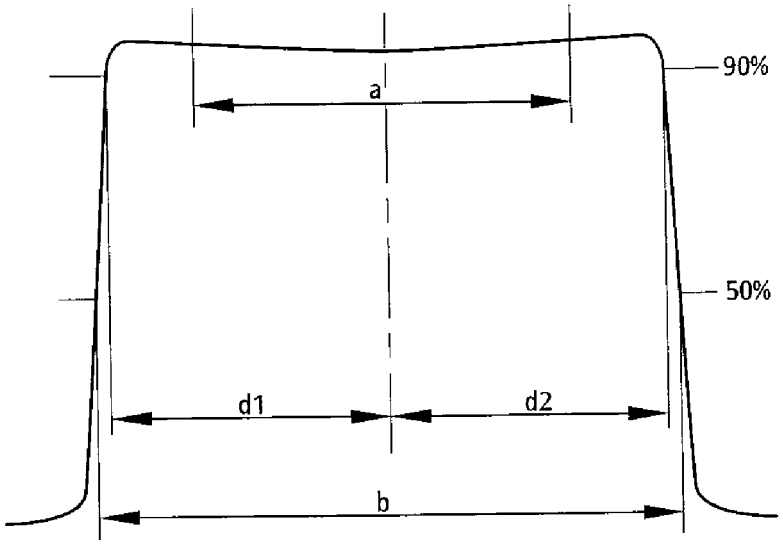

Figure 3.10: Depth dose profile for a linear accelerator beam (Elekta Synergy Platform 2008).

From figure 3.10, the distance *a* defines the beam uniformity (flatness), distance *d*1and *d*2, describes the beam symmetry, and distance *b*, defines the geometrical beam field size which is the 50 % of the isodose curve (Wysocka A. *et al* 2000). The dose at any depth is greatest on the central axis of the beam and gradually decreases towards the edges of the beam (or exhibits horns - which are areas of high dose) near the surface in the periphery of the field. Near the edges of the beam (the penumbra region), the dose rate decreases rapidly as a function of lateral distance from the beam axis. This fall-off is also caused by the reduced side scatter (Yin F. F. 1995, Weber L. *et al* 1997). Outside the geometric limits of the beam and the penumbra, the dose variation is the results of side scatter from the field and both leakage and scatter from the collimator system (Khan F. M. 2003).

For the energy beam specification, the central axis depth dose curve is characterized as shown in figure 3.11.

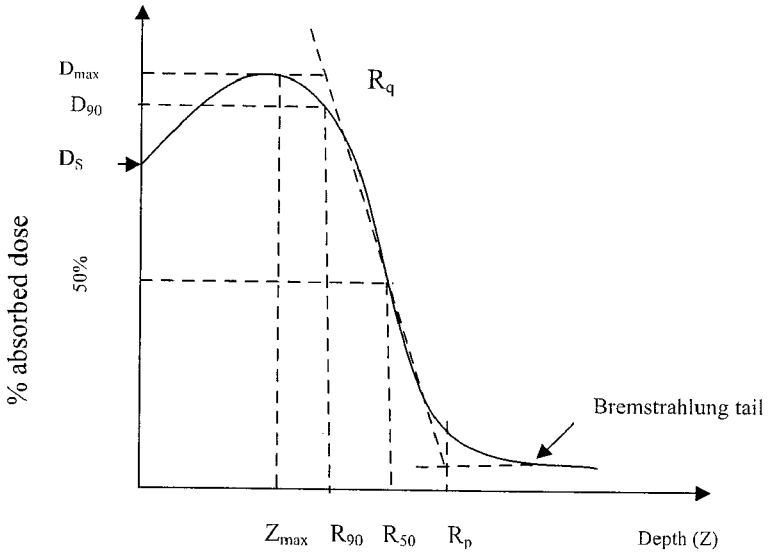

Figure 3.11: Typical electron beam central axis depth dose curve (ICRU 35 1984).

Figure 3.11 shows a typical electron beam central axis depth dose curve measured in water. In general the electron beams exhibits a high surface dose as compared to the photon beams due to its less penetrative capabilities. The dose builds up to the maximum (D_{max}), at a depth referred to as depth of maximum dose (Z_{max}) (Gerbi B. J. *et al* 1990).

As the beam travels further in medium, there is a continuation of energy loss and scattering of the electrons and thus this is responsible for the sharp fall-off of dose beyond the Z_{max}, as compared to photon beams where the fall-off is gradual. As the beam travels further in the medium, the small dose levels results in the photon contamination (Bremsstrahlung Tail), as compared to the electron contamination in the photon beam at deep depths. The rate of fall-off in the electron beam vary with the incident electron beam, i.e., as the electron beam energy increases, the rate of dose fall-off decreases (i.e. low energy electron beam results in a sharper dose fall-off as compared to higher energy electron beam) (Nilsson B. *et al* 1986, Zhu T. C. *et al* 1989, Sjögren R. *et al* 1996, Saini A. S. *et al* 2004).

At energies as high as approximately 20 MeV, the percentage depth dose curves lose their sharp dose fall-off, and begin to take the characteristics of a photon beams due to bremsstrahlung energy loss (Khan F. M. *et al* 1991, Khan F. M. 2003, Podgorsak E. B. *et al* 2005).

CHAPTER 4

MATERIALS AND METHODS

4.1. Equipments.

In this chapter the equipments, materials and methods used are discussed.

4.1.1. Linear accelerator.

The Elekta Synergy linear accelerator is one of the state of the art linac equipped with Multi Leaf Collimator (MLC*i*) for field shaping. The machine produce the 6 and 15 MV photon beams used for treatment of deep seated tumors and 4, 6, 8, 10, 12 and 15 MeV electron beams for superficial treatment of cancer tumors and other malignancies (Khan F. M. *et al* 1991). Picture 1 show the Elekta Synergy Platform linear accelerator used in this study.

Picture 1: Elekta Synergy Platform linear accelerator (model 151834).

4.1.2. 3D-water phantom.

The 3D-water phantom (75 × 70.5 × 49.5 cm^3) model 9860 from multi-data scanning system is an MP3 large size motorized phantom with up to 60 cm detector moving range and it allows for full scatter contribution for a 40 × 40 cm^2 field size data. The system allows for scanning of beam data (profiles) in cross-plane, in-plane (*x* and *y*) directions and diagonal directions as well as in depth (*z*) direction. The water phantom must be filled with water to the level deep enough to allow the beam scanning to the depth of 30 cm (Schmid M. G. *et al* 1989, Mellenberg D. E. *et al* 1990). The water phantom consists of a remote controlled, precision probe positioning mechanism mounted into it and designed to measure complete radiation field characteristics in any of three scanning planes. The probe carriage is supported on both sides and remains submerged when the detector is at or above the water surface. The probe holders are indexed for rotation at 45° intervals and shaped to minimize water ripple (Das I. J. *et al* 2008). The water phantom uses finite precision stepping motors, where the number of digital impulses corresponds directly to the travel distance. In addition, an independent high resolution potentiometric measurement circuit exists to verify the actual performance of the direct positioning drive. Specially designed stainless steel cables are used for positioning to avoid mechanical hysteresis in detector position and to provide tight, but smooth motion during scanning (Das I. J. *et al* 2008).

The water phantom is made from stress relieved acrylic with glued seams. The left, front and right side walls are nominal 1 cm thick, providing a horizontal ówindowô access from the front. The clear water phantom provides extra visibility of the light field and facilitates its leveling and setup by using the treatment machineôs patient positioning lasers (Das I. J. *et al* 2008). The scanning mechanismôs design is extremely efficient in using all the water volume available and provides excellent water surface access, assuring easy positioning of even the largest Electron Cone (applicator). All parts in contact with water are corrosion resistant stainless steel or selected plastic materials. Stainless steel is used only where it is required for rigidity and strength, and then only in the form of air-filled, thin-walled tubes to minimize scatter (Kalach N. I. *et al* 2003, Das I. J. *et al* 2008). The water phantom is fully interfaced with Multidataôs Real-Time Dosimetry (RTD) system equipment and is interconnected to the electrometer and signal

conditioning unit using an extra shielded, thin and round interconnect cable. The interface consists of six digitally pulsed lines (a plus and minus direction line for each axis), and three analog position output lines. This phantom will be used for scanning beam data (profiles and depth doses). The 1D-water phantom (31 × 33.5 × 38 cm^3, model PK266M-01A, WQP 51790 Multidata QA Phantom) which allow for a 10×10 cm^2 field size set up used for absolute dose output measurements, from multi-data scanning system, it is an MP1 small size motorized phantom with up to at least 33 cm detector moving range in depth. It allows for measurements of depth doses and absolute dose measurements (Spokas J. J. *et al* 1980).

Picture 2 shows the 1D-water phantom used for absolute dosimetry.

Picture 2: 1D-Water phantom.

4.1.3. Ionization chambers.

Ionization chambers have been used since the discovery of radiation and are still widely used due to their small variation in response to energy, dose, dose rate, and reproducibility. Ion-chambers are operated in the voltage range of 300 - 400V. They have an almost constant energy response

for megavoltage photon beams and can be used without corrections (Das I. J. *et al* 2004, Podgorsak E. B. *et al* 2005).

Since chambers can be calibrated against a national standard, they can provide a direct measure of the dose. Ion chambers are relatively inexpensive, readily available, and are manufactured in various shapes (cylindrical, spherical and parallel plate) and sizes [standard (å$10^{-1}cm^{-3}$), both mini (å$10^{-2}cm^{-3}$) and micro (å $10^{-3}cm^{-3}$)]. Two ionization chambers (Type PTW 31010) with sensitive volumes of 0.125 cm^3 (which gives enough signal to use the chambers also for high precision absolute dose measurements) vented to air were used. The sensitive volume is approximately spherical resulting in a flat angular response and a uniform spatial resolution along all three axes of a water phantom. They are both waterproof, semi flexible design for easy mounting in the scanning water phantom, with a minimized directional response. These chambers will be used for scanning the radiation beam data (profiles and depth doses).

The PTW 30013 Farmer type ionization chamber is a waterproof, fully guarded chamber with a sensitive volume of 0.6 cm^3 vented to air with graphite acrylic wall and an aluminum central electrode (Kim Y. K. *et al* 2005). It is the standard ion-chamber for absolute dose measurements in radiation therapy. Correction factors needed to determine absorbed dose to water or air Kerma are published in the pertinent dosimetry protocols. Its waterproof design allows the chamber to be used in water or in solid state phantoms. The acrylic chamber wall ensures the ruggedness of the chamber.

4.1.4. Electrometer.

The electrometers used with a water phantom scanning system have a high degree of fidelity with a wide dynamic range (Podgorsak E. B. 2003). They can measure charge in the range of 10^{-6} to 10^{-14} C. They should be reset to zero before scanning. The response must be verified that it is linear before measuring any data in various gain range settings. A collected reading is a composite response of the detector and electrometer. The detector reading is normally microseconds whilst the electrometers are milliseconds, hence electrometer response is much critical in scanning (Podgorsak E. B. *et al* 2005). The Model 9855 Dual Channel Electrometer

Amplifier consists of two identical, radiation hardened, electrometer amplifier circuits with two isolated internal power supplies, one for the ion-chamber bias voltage and the other to provide power for the signal conditioning electronics. The amplifiers have exceptionally high input impedance and offer a special guarding and shielding configuration, designed to tolerate high cable capacitance without increased noise or degradation of the ion-chamber signal. The triaxial input is arranged to isolate the signal from the bias voltage through a shield at ground potential, allowing effective guarding up to the base of the ion-chamber (Das I. J. *et al* 2008).

The PTW Unidos E Universal dosimeter is an easy to use reference class or field class dosimeter for routine dosimetry. It is an economic high quality dosimeter for universal use in radiation therapy and diagnostic radiology. It complies with the following standards: IEC 60731 as a field class dosimeter, IEC 60731 as a reference class dosimeter, IPEM guidelines on dosimetry transfer instruments as a secondary standard dosimeter and IEC 61674 as a diagnostic dosimeter. It has a high accuracy, excellent resolution (1 fA) and wide dynamic measuring ranges. It has a high voltage (HV) power supply of ± 400V in increments of ± 50V. It measures the integrated dose (or charge) and dose rate (or current) simultaneously. It has an RS232 interface for device control and data output. The electrometer also has the capability to connect both the ionization chamber and the solid-state detectors.

4.1.5. Profiler 2 Scanning system.

A detector array system can be used for simultaneous data acquisition (beam profiles) over the entire open beam and offers the most suitable method for soft wedge (dynamic wedge or virtual wedge) profile measurements. The detector diodes are widely used for their quick response time (microseconds compared to milliseconds of an ion chamber), excellent spatial resolution, absence of external bias and high sensitivity (Zhu T. C. *et al* 1997, Sidhu N. P. 1999). They provide energy independent of mass collision stopping power ratios. The response of diodes detectors depends on temperature, dose rate (SSD or wedge), energy and some may have angular dependence as well.

The Model 1174 profiler 2 scanning system has two intended uses. Primarily, it is intended for Quality Assurance (QA) measurements and analysis of the radiation output profiles across the beam of an ionizing radiation treatment machine. Its secondary use is for the measurements of beam data in radiotherapy departments, for dose modeling in the treatment planning (Khrunov V. *et al* 1990, Heydarian M. *et al* 1993, Hoban P. W. *et al* 1994, Zhu T. C. *et al* 1997). The profiler 2 scanning system is an advanced beam QA tool with *Y* and *X* axes to simultaneously measure saggital and axial profiles in real time for both photons and electron beams. The system uses 139 detectors which have the highest sensitivity and lowest volume of any dosimetric measurement system. Measuring only 0.8 mm × 0.8 mm, profiler 2 detectors are an amazing 1.9×10^{-5} cm^3 ensuring accurate beam measurements under all conditions.

Picture 3 below shows the profiler 2 scanning system.

Picture 3: The profiler 2 scanning system.

The *Y*-axis consists of 83 detectors with 4 mm spacing, which is suitable for a field size of 30 cm at 100 cm SSD. The *X*-axis consists of 57 detectors with 4 mm spacing suitable for a field size of 20 cm at 100 cm SSD. The profiler 2 system uses virtual water build-up above the detector plane. The physical distance from the surface to the detectors is equal to the water equivalent distance (both 1.0 cm) (TG-62 2005, Griessbach I. *et al* 2005).

4.1.6. CMS XiO Treatment Planning System.

The CMS XiO TPS is a comprehensive 3D treatment planning platform that combines the latest tools and most robust dose calculation algorithms to allow users to generate plans quickly and accurately to optimize the delivery of radiation therapy (MeKenna M. G. *et al* 1995, TG-53 1998). The system is based on the pencil beam model, where physical quantities such as profiles and percentage depth dose curves are estimated using conventional method (Lamb A. *et al* 1998). The photon dose calculation model in this TPS system is based on convolution, superposition and Clarksonôs algorithms.

4.2. Beam data acquisition.

4.2.1. 3D-water phantom measurements.

Setting up the water phantom system properly can help improve the workflow, and more importantly, reduce the likelihood of collecting sub-optimal data, which may result in considerable amount of processing and sometimes may even require rescanning. Before setting up the water phantom for data collection, one has to check the existing cable run, set up the scanning computer alongside the accelerator controls to reduce the unnecessary movement across the control area, this can trim considerable time from the total data collection time (Das I. J. *et al* 2008). A periodic quality assurance must be warranted to check the free movement of each arm and the *x*, *y*, *z* and diagonal motion. Accuracy and precision should be checked over the long range of scanning system. Physical conditions of the tank, such as leaks, cracks, and mechanical stability, as well as the quality of connecting cables for leakage and reproducibility should also be checked before the use of the scanning system for beam data collection. All components of the scanning system must match, i.e., from the same manufacturer. Defects or communication errors in any components must be verified. In general, two detectors (or ion-chambers) are needed for scanning a field or a scanning detector that moves in the tank as programmed and a reference detector, which is stationary in the field. The reference detector is recommended because it removes the instantaneous fluctuations or drifts in the incident beam output. Both the scanning and reference detectors must be securely mounted with custom or

vendor specific holders in order to produce accurate and reproducible scans. Metallic adapters and holders should be avoided for securing the detector in the scanning system, as scatter radiation could affect the data accuracy. The reference detector may be positioned anywhere in the beam where it does not shadow the field detector for the entire area of programmed positions. The field and reference detectors should be chosen based on the application of the beam data. Generally, the detectors supplied with the scanning system have identical dimension in active length and inner diameter. The 3D-water phantom was setup under the linear accelerator as shown in picture 4 for the measurements of the photons (6 and 15 MV) beam data.

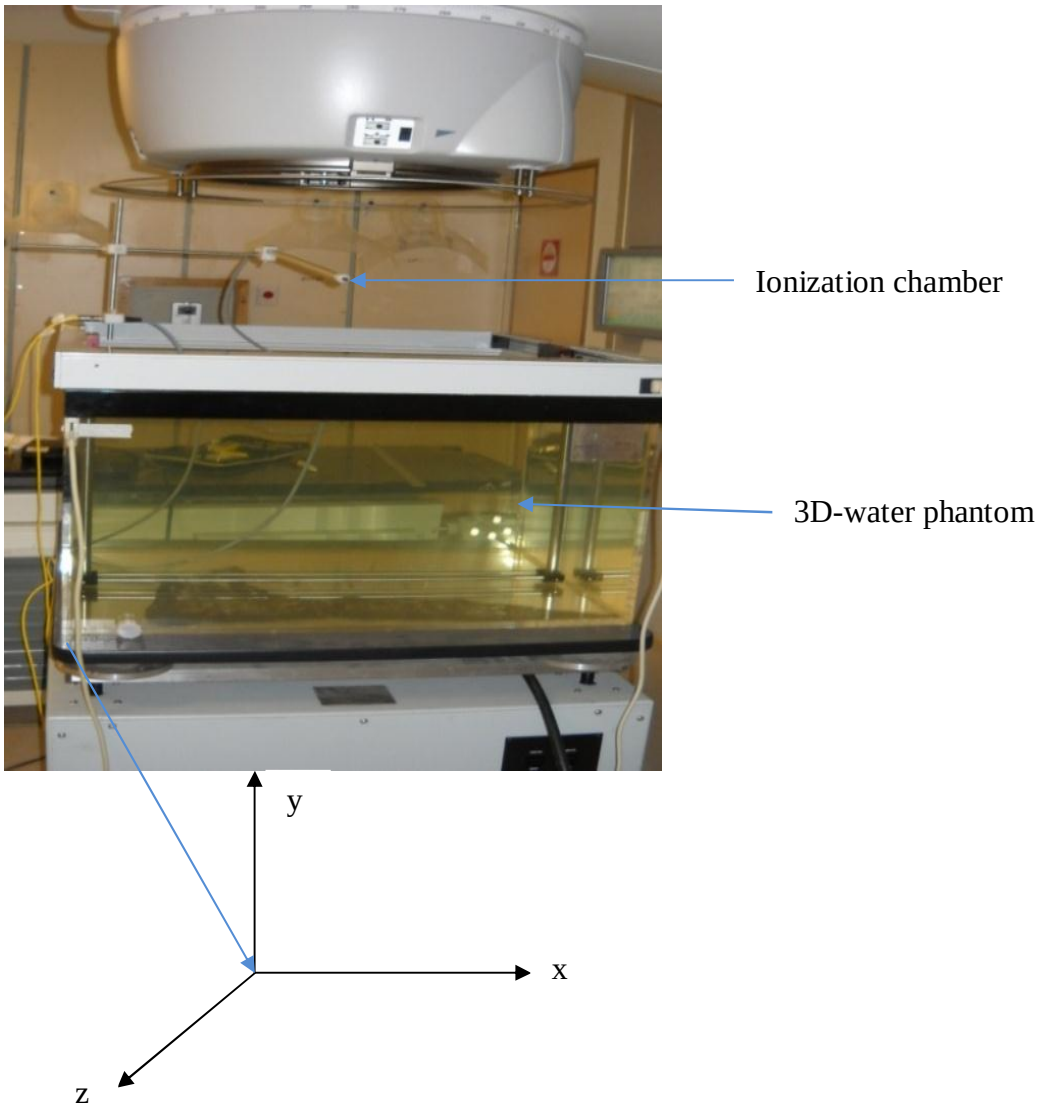

Picture 4: Setup of the 3D-water phantom for measurements of photon beams data.

The water phantom (over a water reservoir) was filled with water to allow the scanning ionization chamber to scan to the depth of 30 cm. The water phantom was positioned and labelled appropriately to ensure the quality of data and to detect possible sources of error in scan data. The water phantom was setup such that the orientation is such that the scanning chamber scans with the least amount of moving parts. The tank origin (0, 0, 0 cm) was set at the machine-isocenter. The water phantom was aligned with the lasers such that *x*-axis is the cross-plane (left-right) and *y*-axis is the in-plane (gun-target) direction. The water phantom levelling was performed using a spirit level. The two ionization chambers (Type PTW 31010) were connected as shown in figure 4.1 below with one chamber used as a reference chamber to adjust for the signal from the linear accelerator and to setup the gain for maximum charge to be collected, and the other chamber in water for scanning the beam.

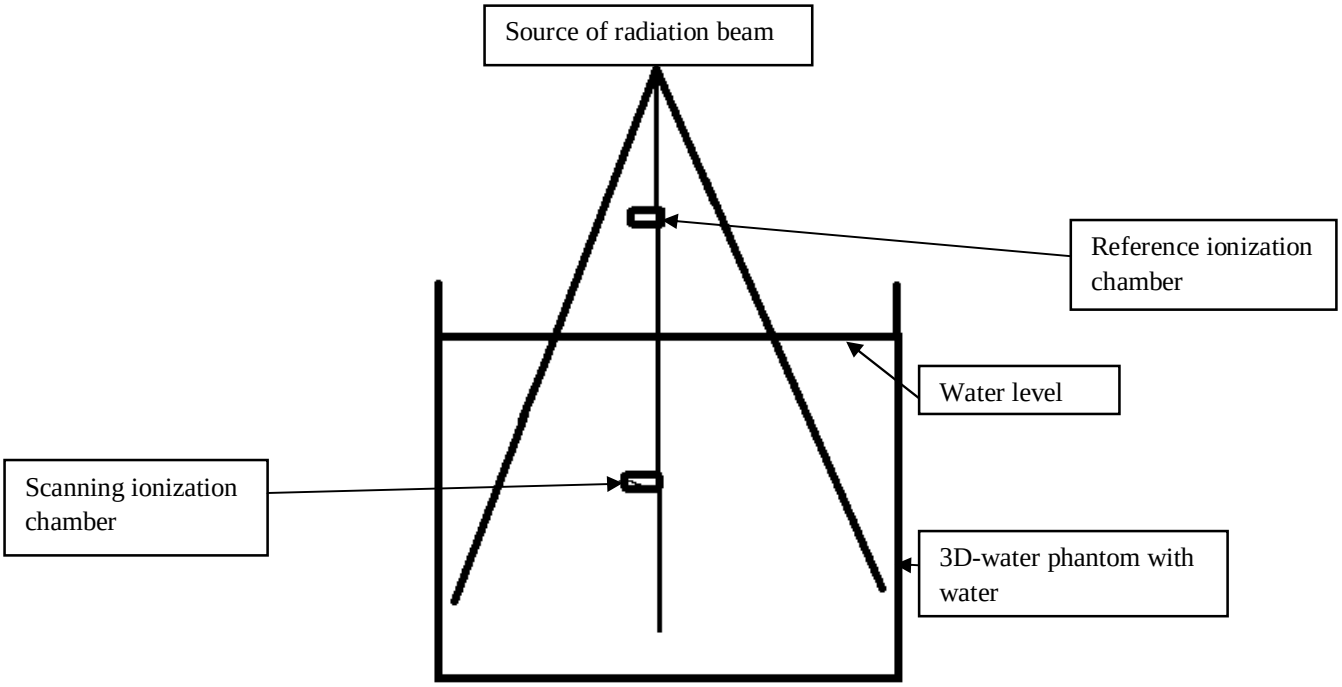

Figure 4.1: Connection setup of the scanning ionization chambers.

The scanning ionization chamber was levelled with water surface in all four corners of the tank and the directional movements (*x*, *y* and *z*) were established as shown in picture 4.

The *z*-direction movement of the chamber was verified to be parallel and follow the central axis of the machine at 0° gantry angle and 0° collimator angle. The SSD (source surface distance) was setup to 100 cm using both the lasers and the ODI (optical distance indicator). The scanning ion-chamber was then positioned such that the centre of the chamber splits the water surface and the reflected image and the ion-chamber makes a perfect circle. This position was then denoted the zero position, and this was set on the scanning computer for scanning purposes. Water evaporation can cause a change in zero depth, therefore the water level was checked periodically every 6 hours during the day. The water phantom scanning systemôs orientation was verified with the gantry axes. Before the beam data was collected, the acquisition plans were setup on the scanning computer. These plans specify the radiation field information including treatment machine, setup geometry (SSD, FSDD), beam energy and field size. They also specify the scan data point information including study type (single point, depth dose, rectilinear or fan beam profiles, radial profiles, grid, and etc), data point positions, scan positions, and scanning variables like depth, energy or wedges, etc.

For photon beams (6 and 15 MV), the acquisition plans were setup on a scanning computer using the RTD (real time dosimetry) multidata scanning software for data collection for the following field sizes: 6×6 cm^2, 10×10 cm^2, 14×14 cm^2, 20×20 cm^2 and 25×25 cm^2 all at the depths of 0.5 cm, 1.0 cm, 2.0 cm and 5 cm.

For electron beams (4, 6, 8, 10, 12 and 15 MeV), the acquisition plans were also setup on a scanning computer using the RTD (real time dosimetry) multidata scanning software for the following standard electron cones (applicators) sizes: 6×6 cm^2, 10×10 cm^2, 14×14 cm^2, 20×20 cm^2 and 25×25 cm^2 all at the depths of 0.5 cm, 1.0 cm, 2.0 cm and 5 cm. Setup for electron beams scanning:

Picture 5: Setup of the 3D-water phantom for measurements of electron beams data.

All the data collected were sent to excel spread sheet for analysis. Only the 10 × 10 cm^2 beam data at 1.0 cm depth were sent to CMS XiO treatment planning system for modelling.

4.4.2. Profiler 2 scanning system measurements.

Before the profiler 2 scanning system can be used, it needs to be calibrated properly, both for array calibration and dose calibration to set the amplifier gain of each detector before it can be used for scanning. Array calibration uses a wide-field procedure to measure the relative sensitivity differences between profiler 2 detectors. The sensitivity differences are stored as individual correction factors to be applied to the raw measurements from each detector (Zhu T. C. *et al* 1997, Saini A. S. *et al* 2002, Lilie L. *et al* 2007).

The correction factors eliminate response differences between the individual detector circuits. For the array calibration of all beam energies, four exposures were taken. For photon beams (both the 6 and 15 MV) array calibrations, the linear accelerator cross hairs were centred on the detector 42 (array centre) with the *+Y* axis towards the couch foot with the SSD of 100 cm and

the field size of 35 × 35 cm^2. The nominal gain was set to 4 for the exposure of 200 MU/min set on the accelerator. This is shown on figure 4.2 below.

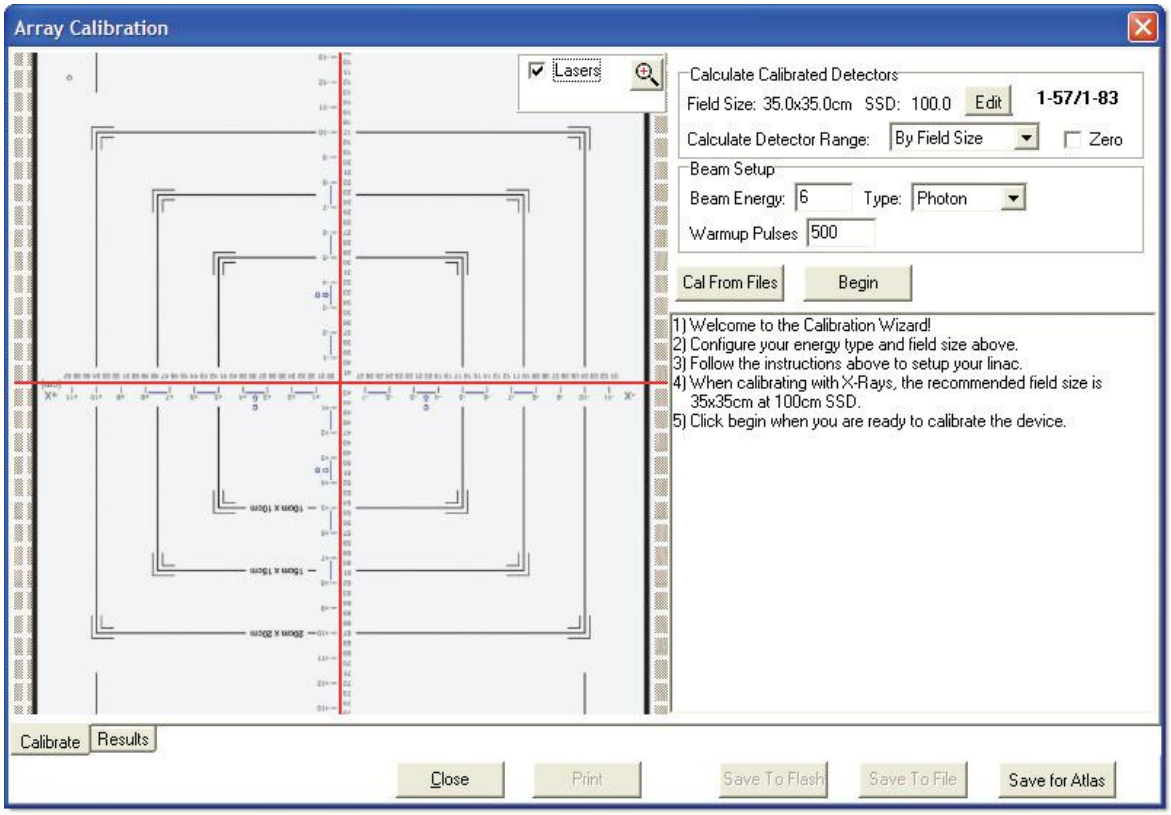

Figure 4.2: Cross hairs setup for array calibration (Profiler 2 reference guide 2010).

The second exposures were taken with the profiler 2 scanning system rotated through 180° clockwise with the cross hairs on the centre detector. For the third exposures, the profiler 2 scanning system was shifted a distance of 4 mm in the -*Y* direction, and the fourth exposures were taken with the profiler 2 shifted a distance of 4 mm in the -*X* direction. The profiles were then verified and saved in a calibration file.

For all electron beam energies (4, 6, 8, 10, 12 and 15 MeV) the linear accelerator cross hairs were also centred on the detector 42 (array centre) with the +*Y* axis towards the couch foot with the SSD of 100 cm and the largest electron applicator of 25 × 25 cm^2. The nominal gain was also set to 4 for the exposure of 200 MU/min set on the accelerator. The second exposures for all electron beam energies were also taken with the profiler 2 scanning system rotated through 180°

clockwise with the cross hairs on the centre detector. For the third exposures, the profiler 2 scanning system was shifted a distance of 4 mm in the -*Y* direction, and the fourth exposures were taken with the profiler 2 shifted a distance of 4 mm in the -*X* direction. The profiles were then verified and saved in a calibration file. Absolute dose calibration, converts the profiler 2 corrected counts to dose values by applying a single calibration factor to all detectors.

For photon beams, the profiler 2 scanning system was positioned on the treatment couch under the linear accelerator with the cross hairs centred on detector 42 with a build up of 9 cm Perspex slabs to simulate the 10 cm depth of ion-chamber in water, the source to chamber distance (SCD) was set to 100 cm and the field size (FS) of 10×10 cm^2. The linear accelerator was set to deliver 100 MU/min dose output for both 6 and 15 MV photon beam energies. The dose calibration files were then saved (Georg D. *et al* 1999, Quach K. Y. *et al* 2000).

For electron beams (4, 6 and 8 MeV), the profiler 2 scanning system was also positioned on the treatment couch under the linear accelerator with cross hairs centred on detector 42 without build up (contrary to the 10, 12 and 15 MeV, where the 1 cm Perspex slab build up was used) with the SCD set to 100 cm and the electron applicator size of 10×10 cm^2 used (Tzedakis A. *et al* 2004).

The profiler 2 scanning system was setup under the linear accelerator as shown in the picture 6 below for the measurements of the beam data.

Picture 6: Setup of the profiler 2 scanning system.

The profiler 2 scanning system was stored in the treatment room to allow for all parts of the instrument to reach the temperature equilibrium (Tailor R. C. *et al* 1998). The linear accelerator SSD was set to 100 cm with the gantry position at 0°. The beam profiles were collected for both photon and electron energies as follows:

Photon beams (6 and 15 MV): Perspex slabs were used as water equivalent for build up to simulate the depths. The following field sizes were scanned for both the 6 and 15 MV photon beams; 6×6 cm^2, 10×10 cm^2, 14×14 cm^2, 20×20 cm^2 and 25×25 cm^2, all at the depths of 0.5 cm, 1.0 cm, 2.0 cm and 5 cm which were achieved by putting Perspex slabs on top of the profiler 2 scanning system whilst adjusting the treatment couch vertically to maintain the SSD of 100 cm.

Electron beams (4, 6, 8, 10, 12 and 15 MeV): The same Perspex slabs were used for electron measurements. All electron beam energies (4, 6, 8, 10, 12 and 15 MeV) were also scanned for the standard applicator sizes: 6×6 cm^2, 10×10 cm^2, 14×14 cm^2, 20×20 cm^2 and 25×25 cm^2, all at the depths of 0.5 cm, 1.0 cm, 2.0 cm and 5 cm, which were archived by putting Perspex

slabs on top of the profiler 2 scanning system whilst adjusting the treatment couch vertically to maintain the SSD of 100 cm.

The profiler 2 scanning system is designed to measure beam profiles rather than depth doses, therefore the 0.6 cm^3 farmer type ion chamber inserted in a calibration block was used for the measurements of depth doses in Perspex for all applicators and field sizes (Song H. *et al* 2006). The ion chamber was positioned in a calibration block (which is 5 cm thick) at 4.4 cm and 0.6 cm on the treatment couch at SSD = 100 cm. Perspex slabs with varying thicknesses (0.1 cm, 0.2 cm, 0.3 cm, 0.5 cm and 1 cm) were added on top of the block to simulate depths, whilst the SSD was kept constant by lowering the couch vertically to achieve SSD = 100 cm.

Picture 7 below show the setup of the calibration block under the linear accelerator for measurements of percentage depth doses.

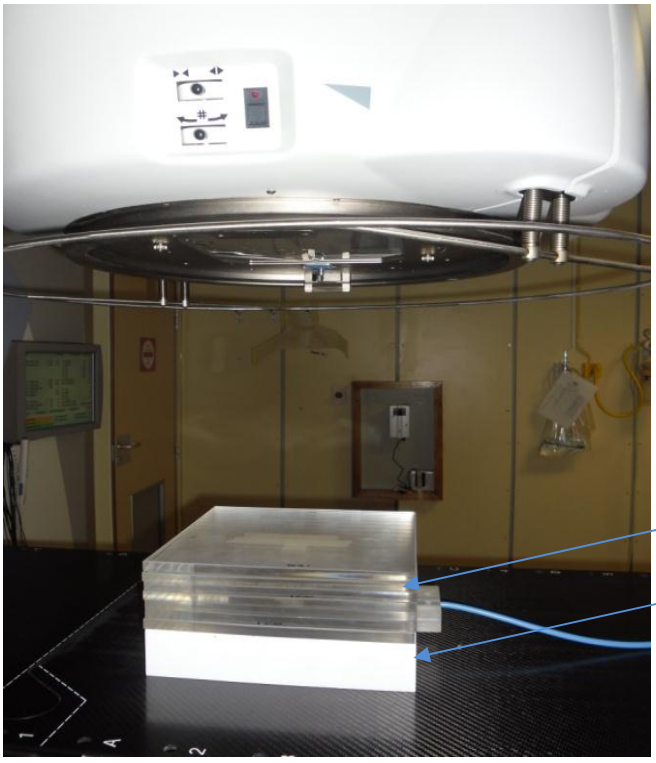

Picture 7: Setup of the Perspex block for measurements of the PDDs for photon beams data.

4.2.3. Absolute dose measurements in water.

The IAEA TRS 398 dosimetry protocol was used as a code of practice for the initial reference dosimetry (beam calibration) for both photon and electron beams. The MP1 1D-water phantom was filled with water and the water was left in the treatment room for about 30 minutes to stabilize (reach equilibrium) with the room temperature before measurements were taken (Tailor R. C. *et al* 1998). For both the 6 and 15 MV photon beam calibrations, the reference conditions were first established as follows: The temperature (T) of water, and the pressure (P) of the room were noted, Gantry position set to 0°, Collimator position set to 0°, SSD = 100 cm, FS = 10 × 10 cm^2, z_{ref} (reference depth) = 10 cm, linear accelerator output setup = 100 MU/min. Three charge readings were collected for each beam energy to correct for statistical variations in the readings. These readings were corrected for temperature and pressure to calculate the dose according to equation (4.4) below. (TG-25 1991, IAEA TRS-398 2001): The measurements were taken at 10 cm depth, therefore the doses were corrected for depth using the percentage depth doses.

Consider the following figure for measurements of absolute doses.

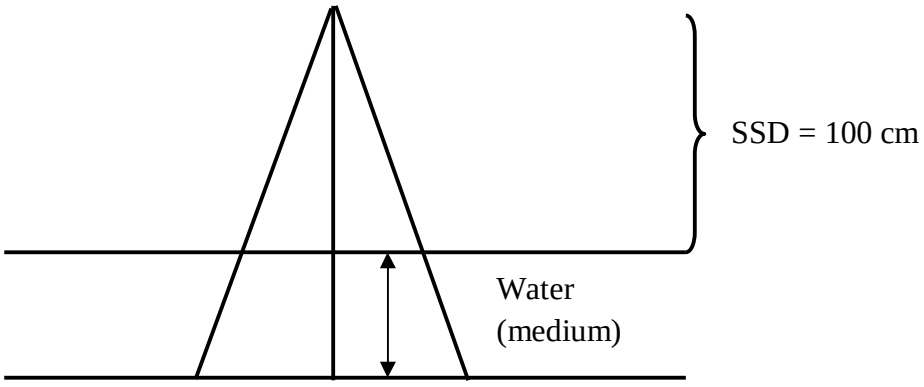

Figure 4.3: Setup for Absolute dose measurements of beam data in water.

For all electron beams (4, 6, 8, 10, 12 and 15 MeV) calibrations, the same reference conditions as in photon beams were used except that the 10 × 10 cm^2 electron applicator was used to define the field size, and measurements for each energy was taken at its specified reference depth as follows: 4 MeV (z_{ref}) = 1.0 cm, 6 MeV (z_{ref}) = 1.5 cm, 8 MeV (z_{ref}) = 1.9 cm, 10 MeV (z_{ref}) = 2.3 cm, 12 MeV (z_{ref}) = 2.7 cm and 15 MeV (z_{ref}) = 3.5 cm.

When using an ionization chamber, the measured quantity is the half-value of the depth-ionization distribution in water, $R_{50,ion}$. This is the depth in water (in g.cm^{-2}) at which the ionization current is 50 % of its maximum value. The half-value of the depth dose distribution in water R_{50} is then obtained using:

$$R_{50} = 1.029 R_{50,ion} - 0.06 gcm^{-2} \left(R_{50,ion} \leq 10 gcm^{-2}\right) \qquad (4.1)$$

$$R_{50} = 1.059 R_{50,ion} - 0.37 gcm^{-2} \left(R_{50,ion} > 10 gcm^{-2}\right) \qquad (4.2)$$

Thus reference depths (z_{ref}) were determined according to the following formalism (TRS-398 2001):

$$z_{ref} = 0.6 R_{50} - 0.1 gcm^{-2} \left(R_{50} \; in \; gcm^{-2}\right) \qquad (4.3)$$

The following equation was used for the determination of dose for both the photon and electron beam calibrations.

$$D_{w,Q} = M_Q N_{D,w,Q} k_{Q,Q_0} \qquad (4.4)$$

4.2.4. Absolute dose measurements with Profiler 2 scanning system.

The profiler 2 scanning system was setup on the treatment couch under the linear accelerator with 9 cm build-up of Perspex slabs on top to achieve 10 cm depth of the detectors since they are 1 cm below from the surface of the profiler 2 scanning system for the measurements of absolute dose for photon beams (6 and 15 MV). The scanning system was left in the treatment room for about 30 min before the measurements were taken to achieve temperature equilibration with the room temperature (Tailor R. C. *et al* 1998, Shi J. 2003). The treatment couch was lowered such that the SSD = 100 cm. The same machine parameters as in MP1 1D-water phantom setup was used, and directs dose measurements were measured.

For electron beams (4, 6 and 8 MeV) dose measurements, 10 × 10 cm^2 electron applicator was used to define the field size, with the SSD = 100 cm without the build-up (Perspex slabs) due to less penetrating capabilities of these energies, and for electron beam energies (10, 12 and 15 MeV), a 1 cm Perspex slab was added for build-up and the treatment couch was moved vertically down to maintain the 100 cm SSD (Lilie L. *et al* 2007).

Six measurements were taken for all beam energies over a period of three months for statistical analysis (both in water and with the profiler 2 scanning system).

4.3. Beam modeling.

After the collection of scanned beam data, it was necessary to do some processing before sending data to treatment planning system for modelling. The multidata scanning system has numerous tools to process beam data, such as smoothing, centering of the beam, and making the beam symmetrical. The amount of processing depends on the type of the scanner, the accuracy of setup, and characteristics of the machine itself (Shi J. *et al* 2003, Ali O. *et al* 2011).

All measured data have a varying degree of noise depending on the system. Smoothing and filtering routines help remove noise and extract actual data. This is also a low pass filtering where high frequencies (abrupt, sharp, spike and wiggle) are eliminated. Numerous smoothing routines are applied using least square, median, arithmetic mean, geometric mean, moving average, cubic spline, exponential, envelope, Gaussian, Fourier transform, and Bezier (Shi J. *et al* 2003). In this study the least square and Gaussian smoothing built in the scanning system were used.

Only the 10 × 10 cm^2 beam data for both the photon and electron beams were exported to XiO CMS treatment planning system for modelling. Beam data were transferred as a batch to XiO CMS treatment planning system. The Beam Modelling Guide (BMG) is designed to help the user for initial modelling, since it provides the step-by-step approach to create beam models. The modelling process requires stretches of uninterrupted attention.

CHAPTER 5

RESULTS AND DISCUSSIONS

5.1. Overview.

Beam profiles, depth dose curves and absolute doses were measured in 3D-water phantom and profiler 2 scanning system using Elekta Synergy Platform linear accelerator. Measurements of beam profiles and depth dose curves were validated using CMS XiO treatment planning system. The measurements were performed for the following energies: 6 and 15 MV photon beams, and 4, 6, 8, 10, 12 and 15 MeV electron beams with different field sizes (6 × 6 cm^2, 10 × 10 cm^2, 14 × 14 cm^2, 20 × 20 cm^2 and 25 × 25 cm^2) at different depths (0.5 cm, 1.0 cm, 2.0 cm and 5.0 cm). All measurements were performed at SSD = 100 cm. The PDDs for the profiler 2 scanning system were measured using the Perspex block (CB) with Perspex slabs since the system is meant for profiles only and not PDDs.

5.2. Characterization of profiles and PDDs.

The shapes of PDDs and dose profiles are complex and there is coincidence between different dose distributions, thus resists characterization by any single number. We chose to evaluate deviations between 3D-water phantom and profiler 2 scanning system dose distributions along different dimensions as described below, especially following the recommendations of Both A. J. *et al* (2004).

Each quantity represents a difference of a kind:

$$Q_{3WP} - Q_{\mathrm{Pr}of2} \qquad (5.1)$$

If described as a difference or:

$$\left(\frac{Q_{3WP}}{Q_{3WP}} - \frac{Q_{\mathrm{Pr}of2}}{Q_{3WP}}\right) \times 100\% \qquad (5.2)$$

if described as a percentage difference, where Q is a quantity of interest.

The notations are as follows:

$\boldsymbol{\Delta_{1,PDD}}$ (R_{80} for electron beams, and PDD_{10} for photon beams): for points on the central beam axis beyond d_{max} to depth at which dose is 10 % of maximum. This quantity is the displacement along the central axis direction of the 3D-water phantom isodose curves from the profiler 2 scanning system curves (LaRiviere P. D. 1989, Kosunen A. *et al* 1993, Followill D. S. *et al* 1998) and the limit is 2 % for photons and 1 mm for electrons.

$\boldsymbol{\Delta_{2,PDD}}$ (Build up region in PDDs): for points on the central beam axis in the build-up region, also a displacement of isodose curves.

$\boldsymbol{RW_{50}}$: (Field size): difference in radiological width, which is defined as the width of the profile at half its central axis value with a limit of 2 mm for field sizes less than 20 × 20 cm^2, and 4 mm for field sizes greater than 20 × 20 cm^2.

$\boldsymbol{F_r}$ (Penumbra): difference in the beam fringe or penumbra, which we define as the distance between the 80 % and 20 % of the maximum points on the profile. It is also defined as the region at the edge of a radiation beam, over which the dose rate changes rapidly as a function of distance from the beam axis (i.e. the distance between the 80% and the 20% isodose of the profile) with a limit of ± 12 mm (Metcalfe P. *et al* 1993, Herrup D. *et al* 2005, Chang K. S. *et al* 1996).

$\boldsymbol{\Delta_3}$ (Flatness): for points within the beam but away from the central axis, measured as a percentage difference of the local dose. This includes points just off the central axis to point sat 95 % of the central axis dose. In the computation of $\boldsymbol{\Delta_3}$ we sampled only the primary axis profiles. Flatness or Uniformity can also be defined as the maximum ratio of the maximum absorbed dose (anywhere in the radiation field) to the minimum absorbed dose in the flattened area at the standard measurement depth with a limit of 3 %.

$\boldsymbol{\Delta_4}$ (Symmetry): for points of profiles outside the beam geometrical edges, where both dose and dose gradient are low, measured as a percentage difference of the central axis dose at the same depth, namely:

$$\Delta_4 = \left(\frac{D_{3DWP}}{D_{CAX,3DWP}} - \frac{D_{Prof2}}{D_{CAX,3DWP}} \right) \times 100\% \qquad (5.3)$$

This quantity is measured at points where the dose is less than 7 % of the maximum value on the profile as stated by Both A. J. *et al* (2004). Symmetry can also be defined as the maximum ratio of the absorbed dose at any two points, symmetrically displaced (the symmetry ratio) about the beam axis and within the flattened area at the standard measurement depth with a limit of 3 %.

The following figures show the graphical summary of indices of accuracy used to asses quality of comparison between 3D-water phantom and profiler 2 scanning system (Perspex block) beam data for photon beams and electron beams respectively.

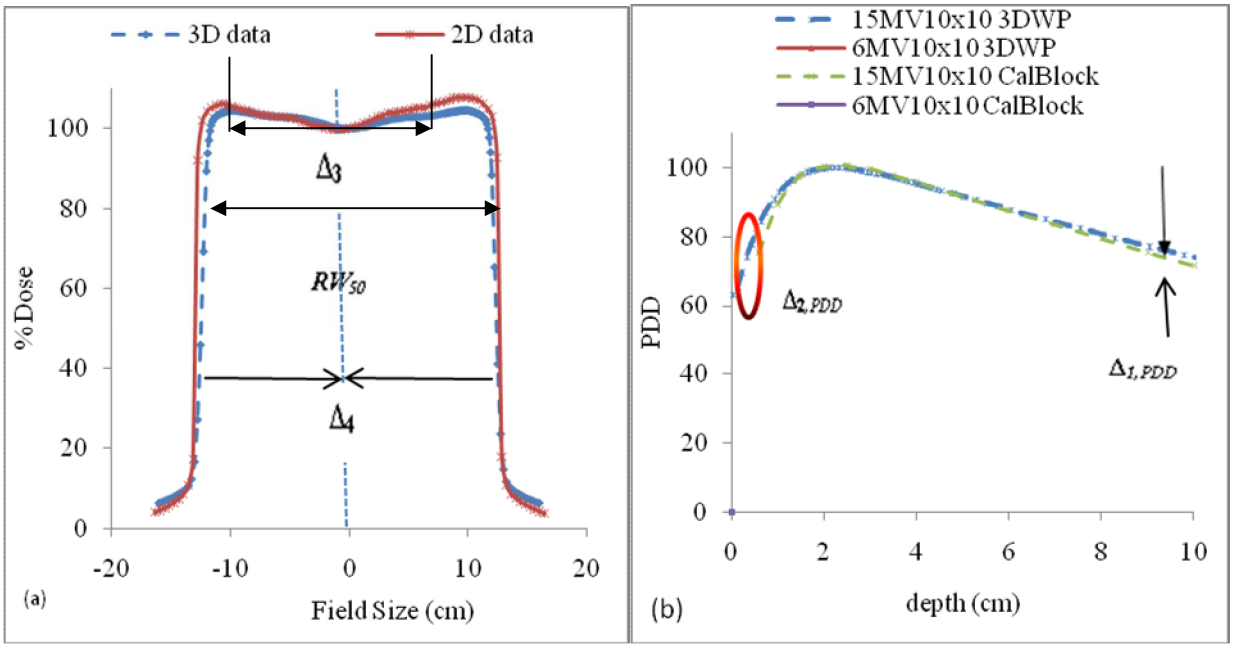

Figure 5.1: (a) Photon beam profiles. (b) Photon beam PDDs.

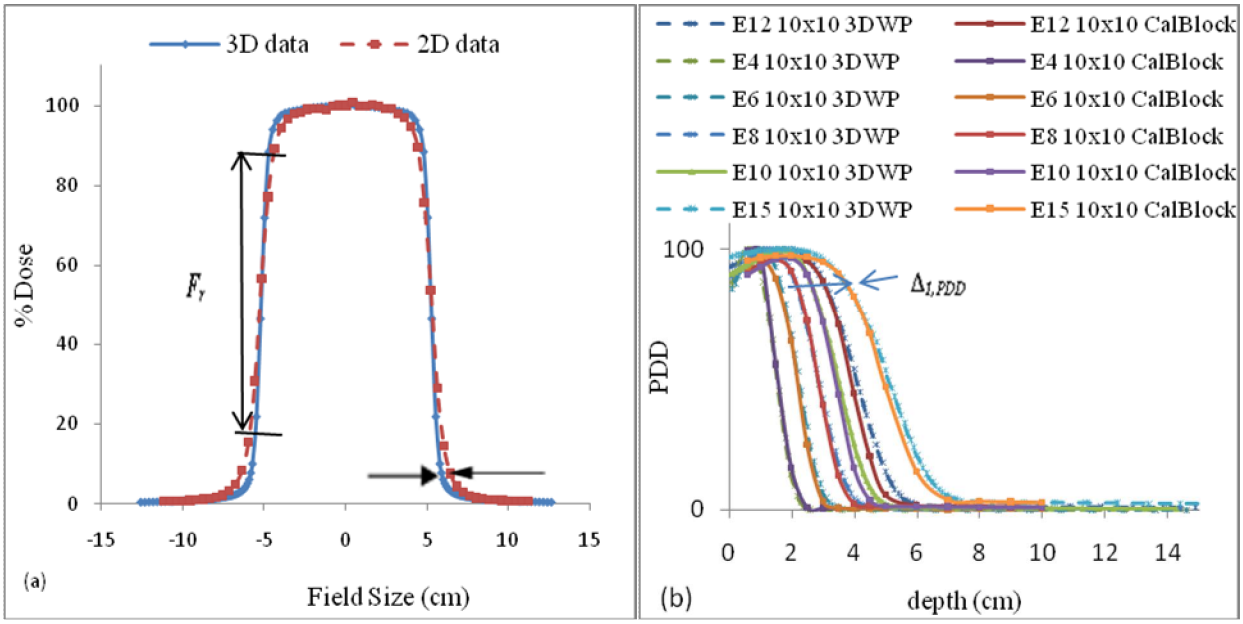

Figure 5.2: (a) Electron beam profiles. (b) Electron beams PDDs.

5.3. Photon beams.

5.3.1. Profiles for 6 MV photon beam.

Figures 5.3.(i) to (iv) show beam profiles for 6 MV photon beam measured with 3D-water phantom and profiler 2 scanning system at 0.5 cm, 1.0 cm, 2.0 cm and 5.0 cm depth respectively.

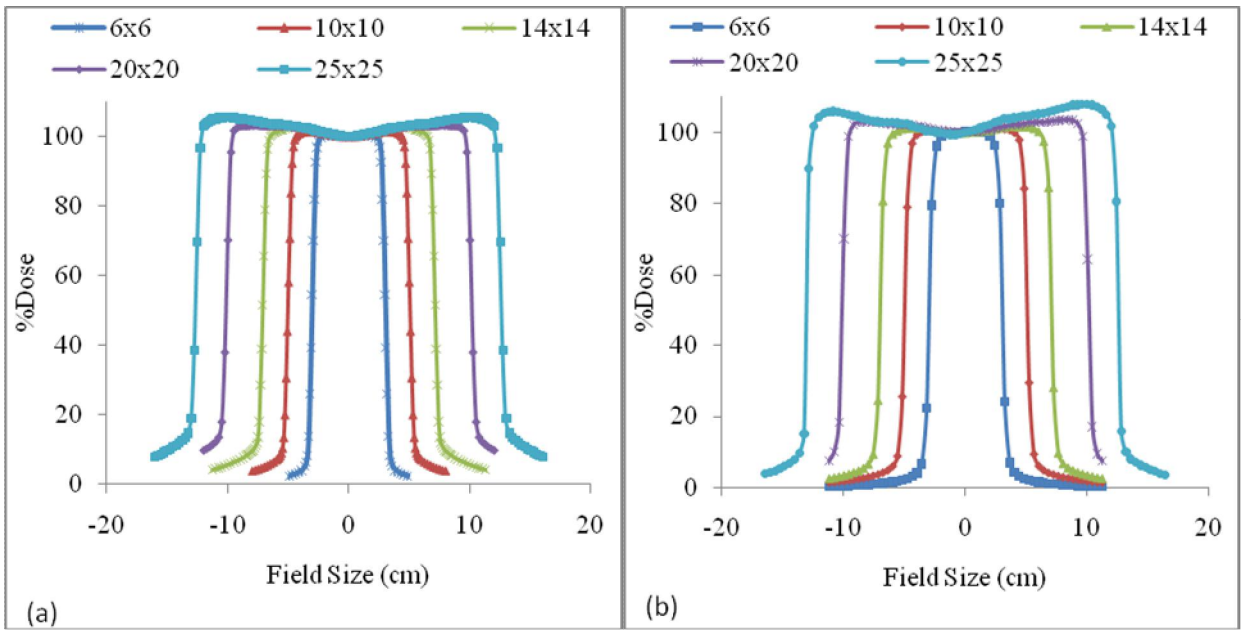

Figure 5.3. (i): Beam profiles measured at 0.5 cm depth. (a) 3D-water phantom beam. (b) Profiler 2 scanning system.

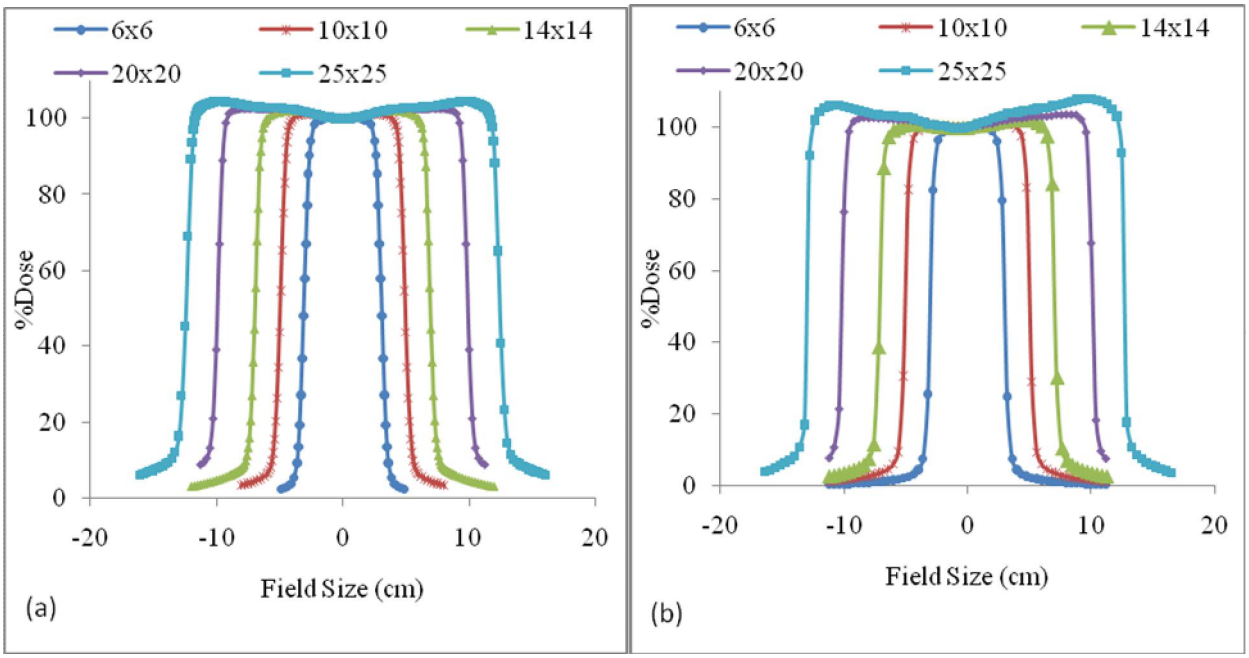

(ii): Beam profiles measured at 1.0 cm depth. (a) 3D-water phantom beam. (b) Profiler 2 scanning system.

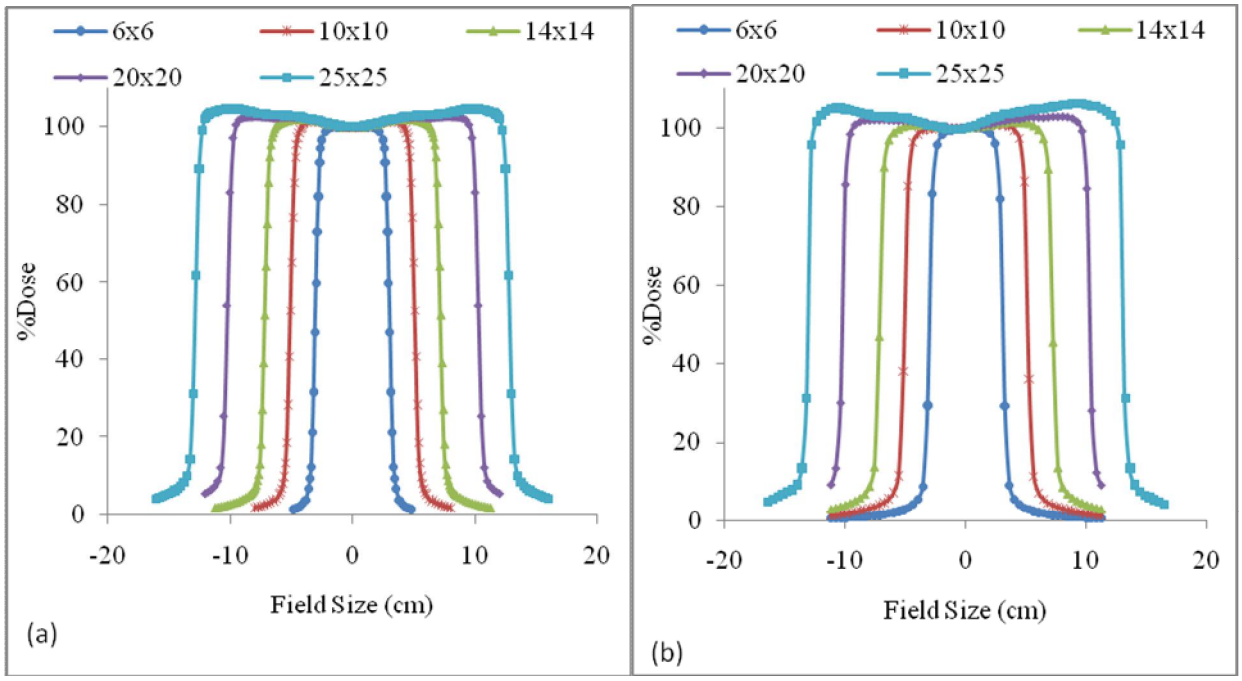

(iii): Beam profiles measured at 2.0 cm depth. (a) 3D-water phantom beam. (b) Profiler 2 scanning system.

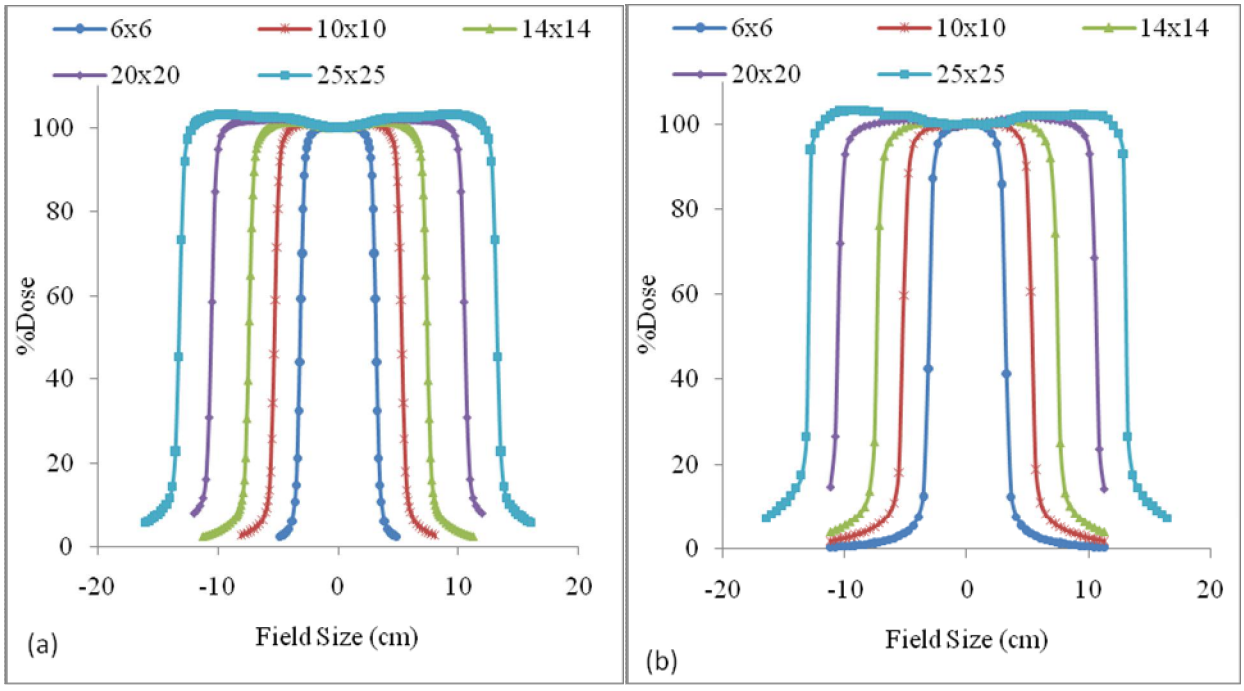

(iv): Beam profiles measured at 5.0 cm depth. (a) 3D-water phantom beam. (b) Profiler 2 scanning system.

From these figures 5.3 (i) ï (iv), it was evident that the profiler 2 scanning system beam profiles for the 6 MV photon beam measured for different field sizes at different depths followed the same trend as for the 3D-water phantom beam profiles, except that the profiles are prolonged on the profiler 2 scanning system at the wash-out region as compared to the 3D-water phantom. This could be due to a number of diode detectors receiving the signal in the profiler 2 scanning system outside the field region.

5.3.2. Profiles for 15 MV photon beam.

Figures 5.4. (i) to (iv) show beam profiles for 15 MV photon beam measured with 3D-water phantom and profiler 2 scanning system at 0.5 cm, 1.0 cm, 2.0 cm and 5.0 cm depth respectively.

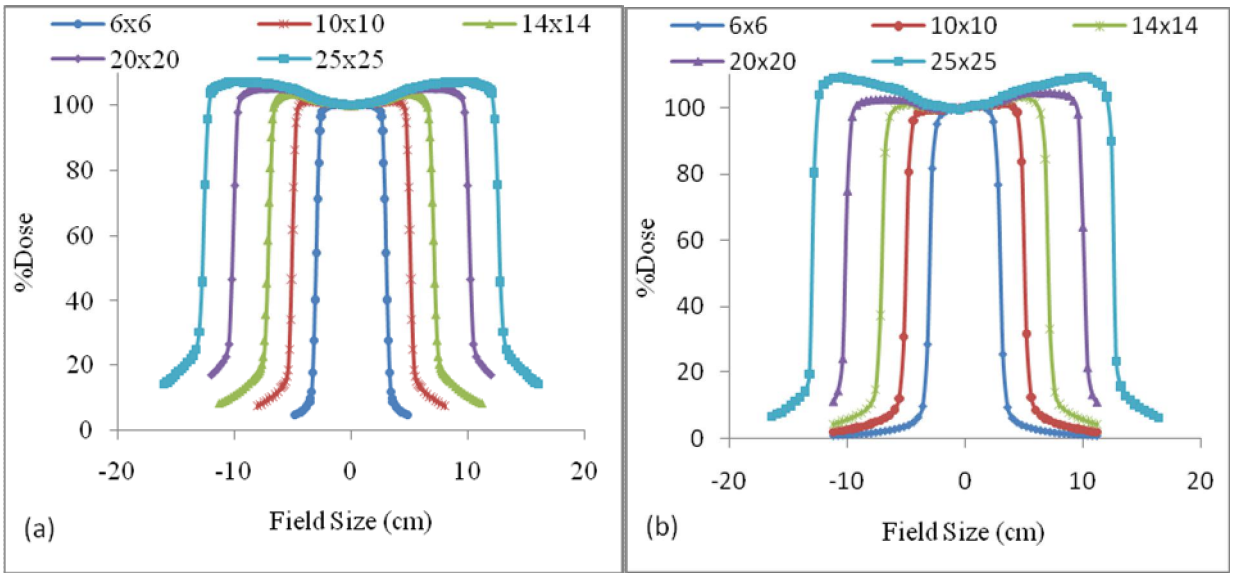

Figure 5.4. (i): Beam profiles measured at 0.5 cm depth. (a) 3D-water phantom beam. (b) Profiler 2 scanning system.

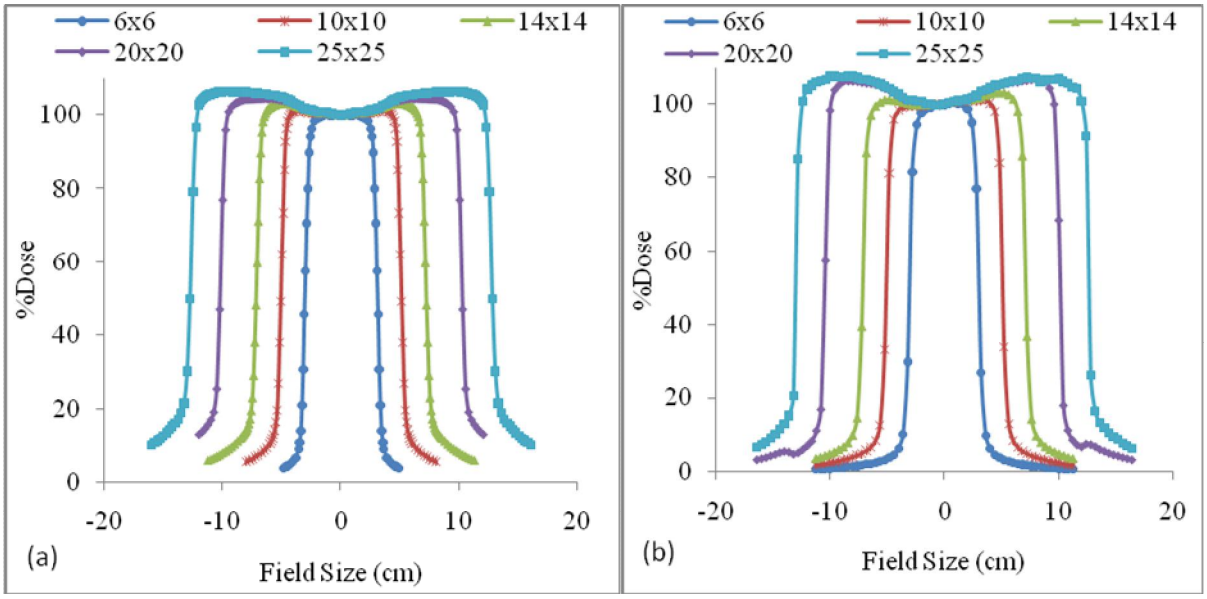

(ii): Beam profiles measured at 1.0 cm depth. (a) 3D-water phantom beam. (b) Profiler 2 scanning system.

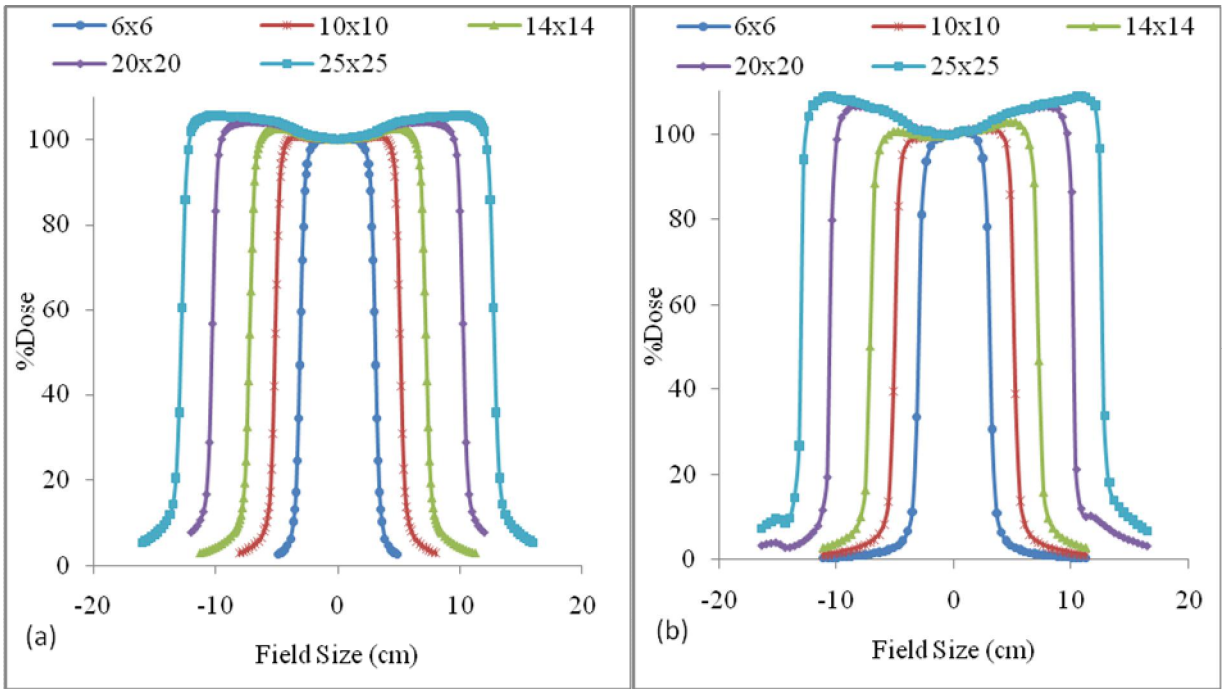

(iii): Beam profiles measured at 2.0 cm depth. (a) 3D-water phantom beam. (b) Profiler 2 scanning system.

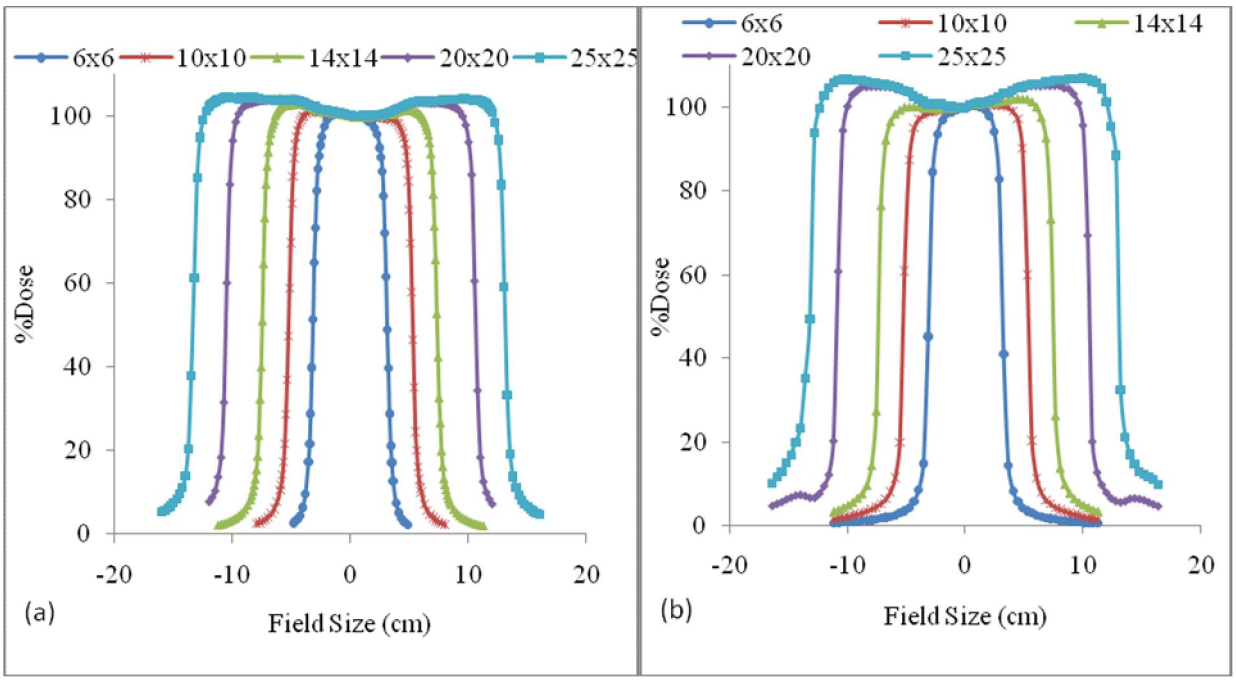

(iv): Beam profiles measured at 5.0 cm depth. (a) 3D-water phantom beam. (b) Profiler 2 scanning system.

From these figures 5.4 (i) - (iv), similar argument as for the 6 MV photon beam was seen for the 15 MV photon beam.

Figure 5.5 show a comparison between the 3D-water phantom and profiler 2 scanning system beam profiles for all field sizes measured for the 6 and 15 MV photon beam at 1.0 cm depth.

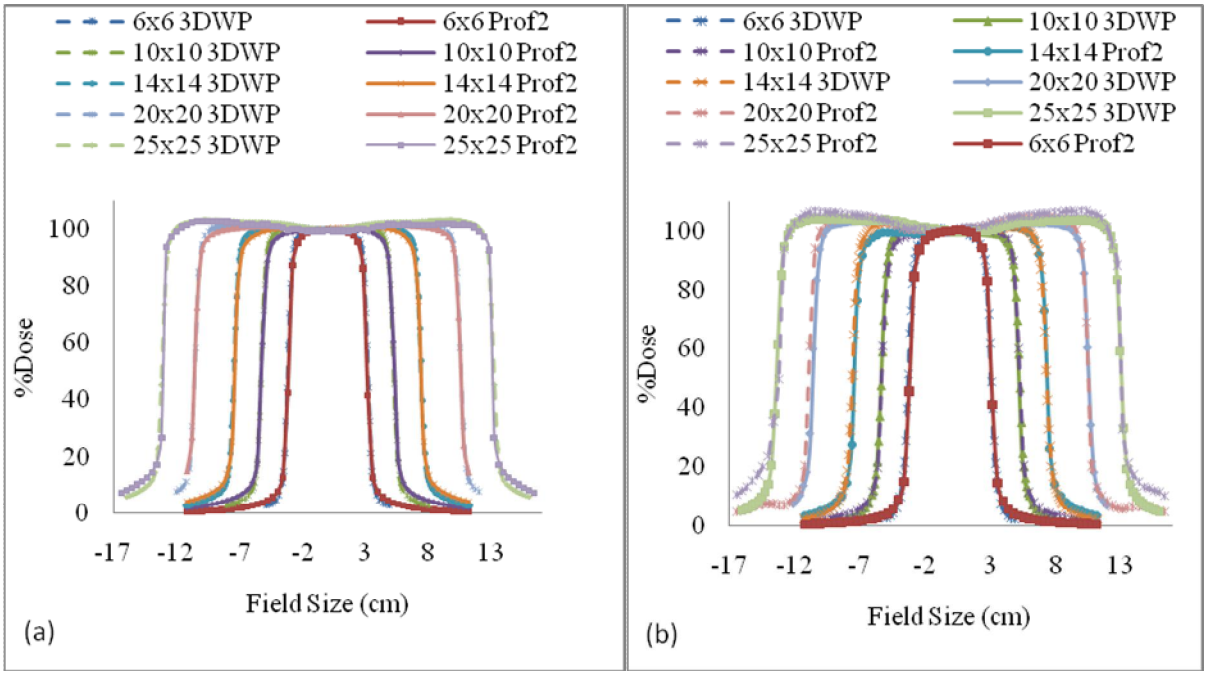

Figure 5.5: Comparison of photon beam profiles. (a) 3D-water phantom and profiler 2 scanning system for 6 MV. (b) 3D-water phantom and profiler 2 scanning system beam for 15 MV.

From these figures 5.5 (a) and (b), it was evident that the two systems (profiler 2 scanning system and 3D-water phantom) beam profiles for the 6 MV (a) and 15 MV (b) photon beams compared very well within the recommended limits of 2 mm (± 2 %) in general, except for the 25 × 25 cm^2 field size beam profiles for the 15 MV photon beam where there was a slightly high difference in the wash-out area. This could be due to the inherent 0.9 cm build-up of Perspex in the profiler 2 scanning system which has the density close to that of water but not the same.

5.3.3. PDDs for 6 MV photon beam.

Figures 5.6 and 5.7 shows the comparison of the 3D-water phantom and the Perspex block PDDs for all field sizes for 6 and 15 MV photon beams respectively.

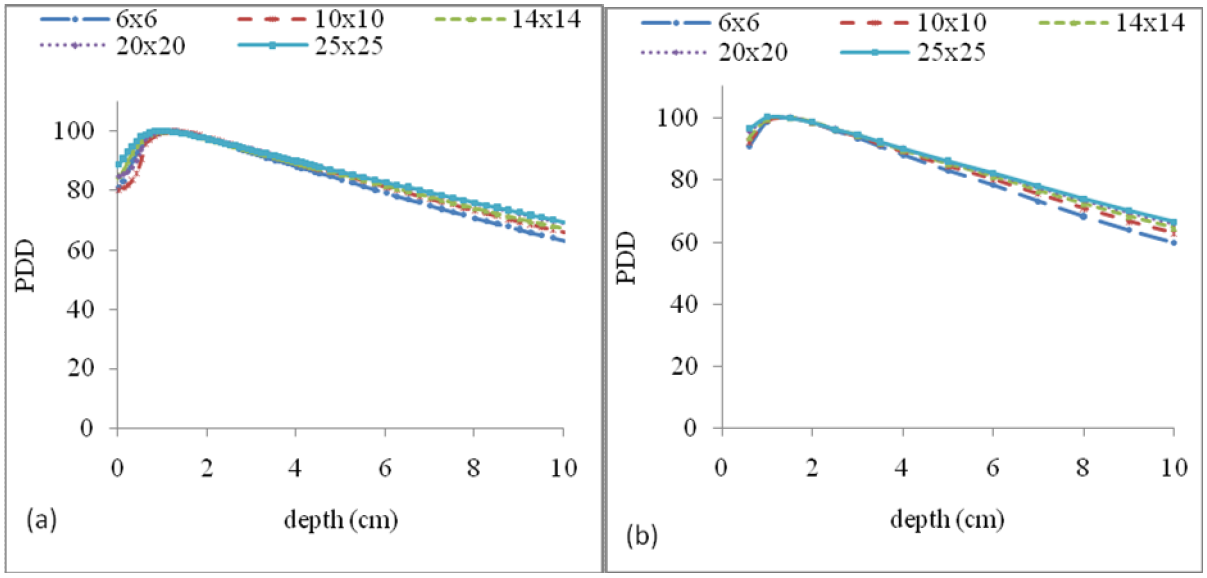

Figure 5.6: PDDs for the 6 MV photon beam. (a) 3D-water phantom. (b) Perspex block.

5.3.4. PDDs for 15 MV photon beam.

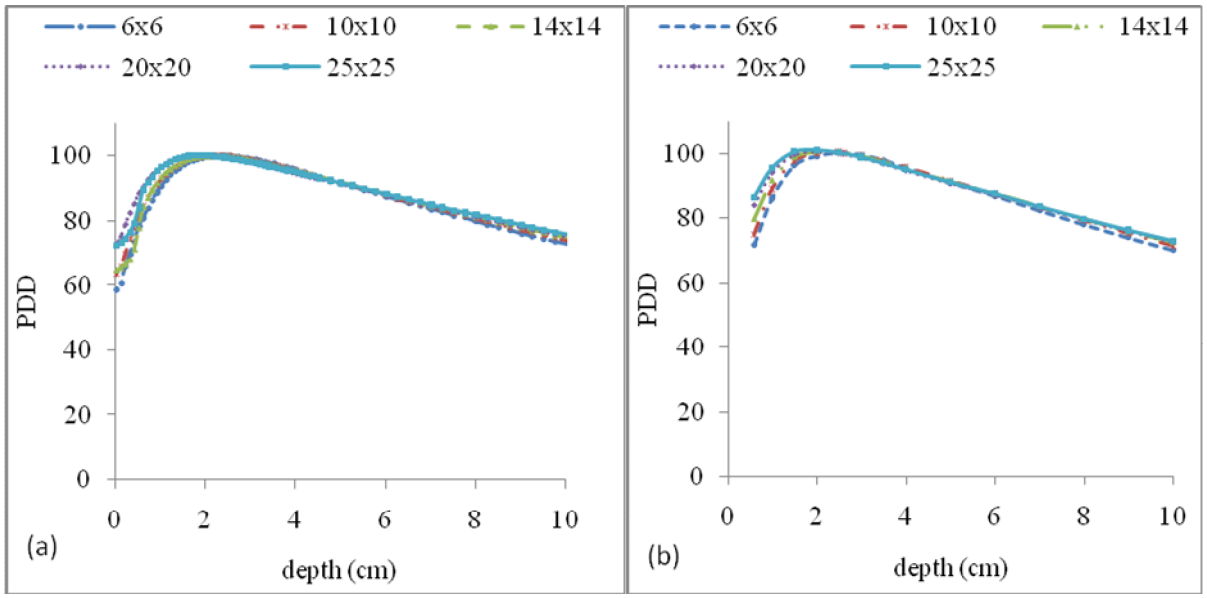

Figure 5.7: PDDs for the 15 MV photon beam. (a) 3D-water phantom. (b) Perspex block.

From these figures 5.6 and 5.7, it was evident that the Perspex block PDD measurements followed the same trend as the 3D-water phantom PDD measurements for both the 6 MV and 15 MV photon beams respectively. From these results one can deduce that there was a shift in the buildup region with the Perspex block measurements. This was due to the inherent buildup in the Perspex block of 0.6 cm that caused the shift in that area and thus restricts measurements at 0 cm depth (surface) to be taken with the Perspex block. The other limitation with the Perspex block measurements was the availability of number of Perspex slabs to be able to measure PDDs at depths deeper than 10 cm, as it was clear from the PDDs that only measurements up to 10 cm depth were taken.

5.4. Electron beams.

5.4.1. Profiles for electron beams.

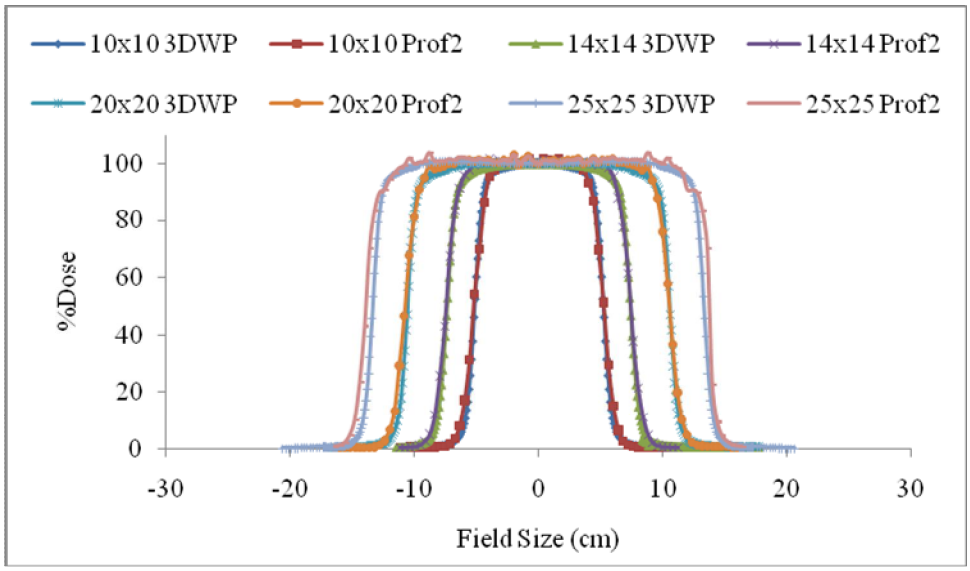

Figure 5.8 (i): Comparison of measured beam profiles for 3D-water phantom and profiler 2 scanning system for 4 MeV electron beam measured at 0.5 cm depth.

From figure 5.8 (i), one can deduce that there was a shift between the profiler 2 scanning system and the 3D-water phantom on the 25 × 25 cm^2 beam profile which was well within the recommended limits of 2 mm (± 2 %). The profiler 2 scanning system beam profile for the

25 × 25 cm^2 field size showed noise in the uniform area suggesting that there was some inconsistency / stability in the sensitivity of the detector diodes during that particular scan / measurement for the 4 MeV electron beam.

The following figures (Figures 5.8. (ii) to (vi)) show the 6 to 15 MeV electron beam profiles for the 3D-water phantom and profiler 2 scanning system measured at 1.0 cm depth respectively.

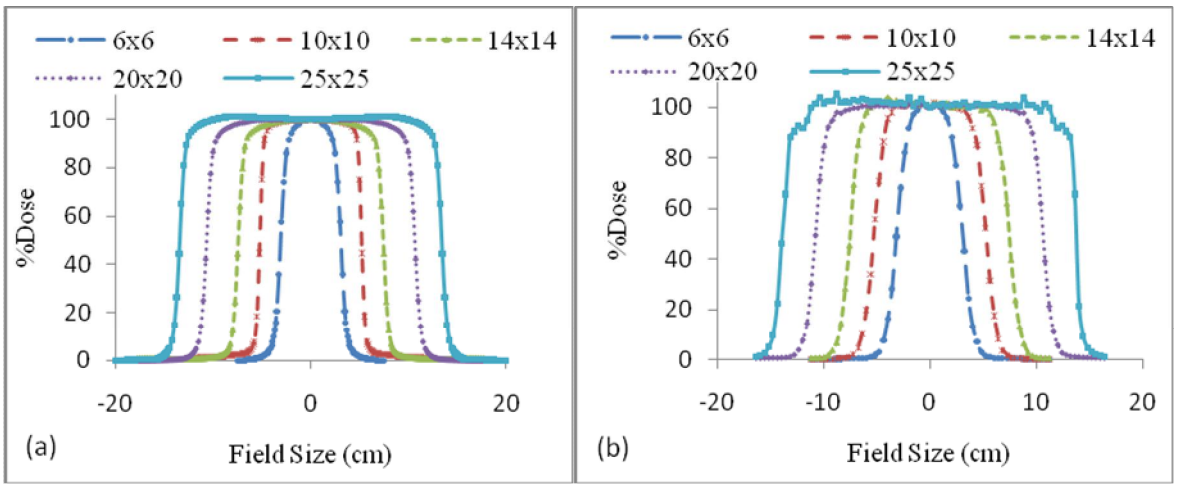

(ii): Beam profiles for 6 MeV measured at 1.0cm depth. (a) 3D-water phantom. (b) Profiler 2 scanning system.

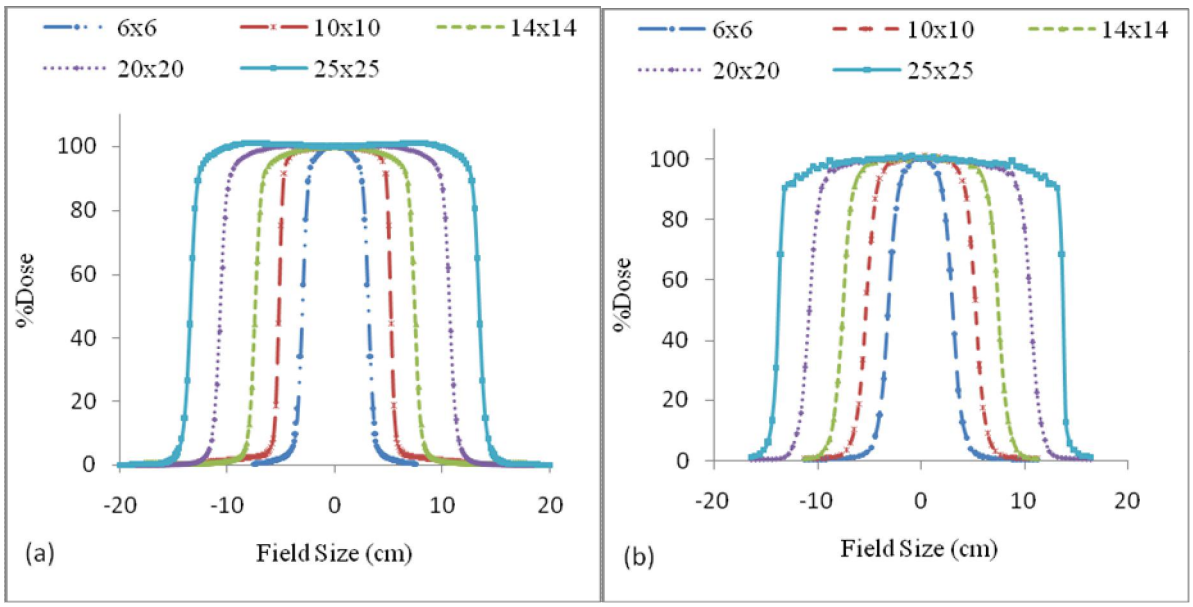

(iii): Beam profiles for 8 MeV measured at 1.0 cm depth. (a) 3D-water phantom. (b) Profiler 2 scanning system.

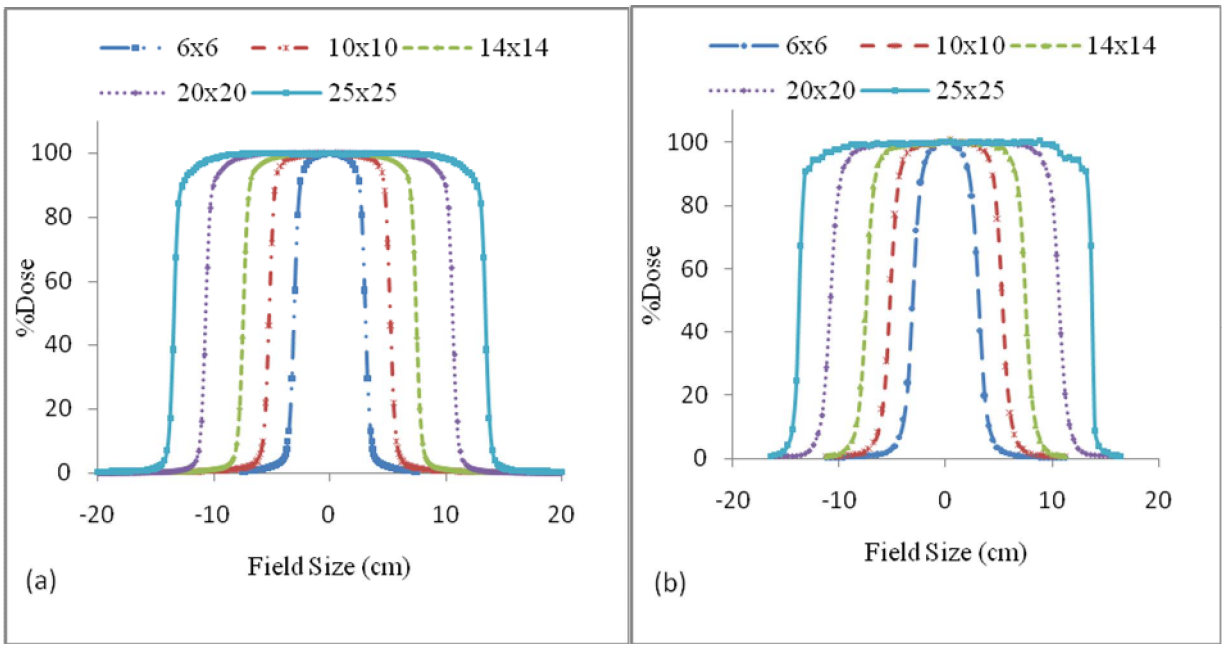

(iv): Beam profiles for 10 MeV measured at 1.0 cm depth. (a) 3D-water phantom. (b) Profiler 2 scanning system.

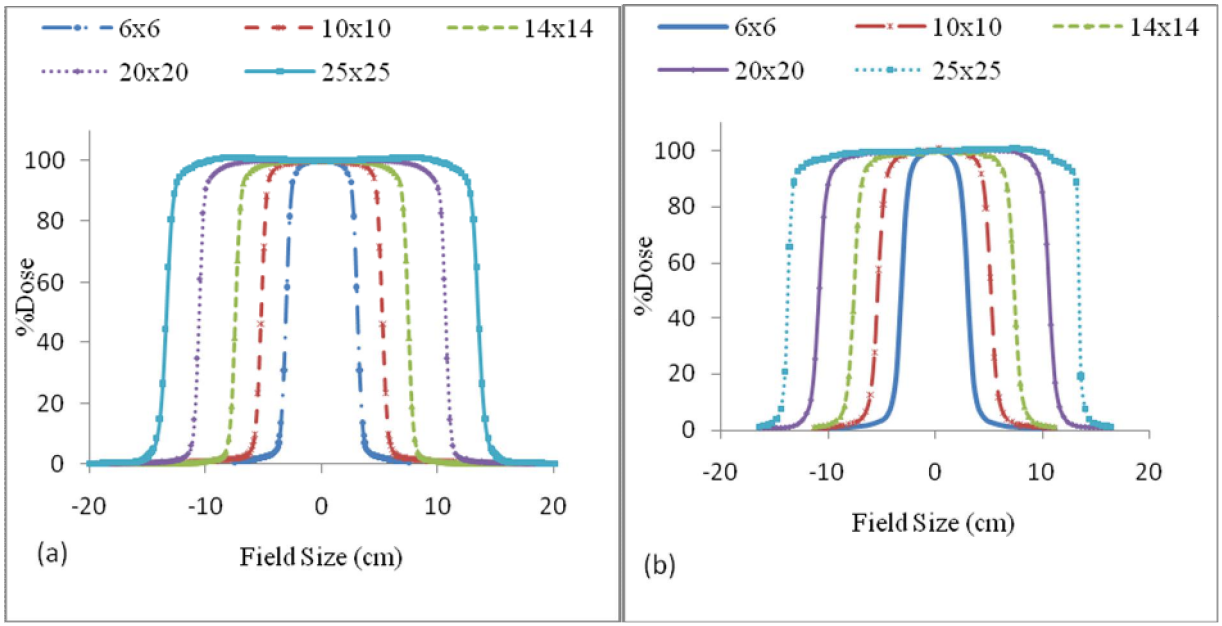

(v): Beam profiles for 12 MeV measured at 1.0 cm depth. (a) 3D-water phantom. (b) Profiler 2 scanning system.

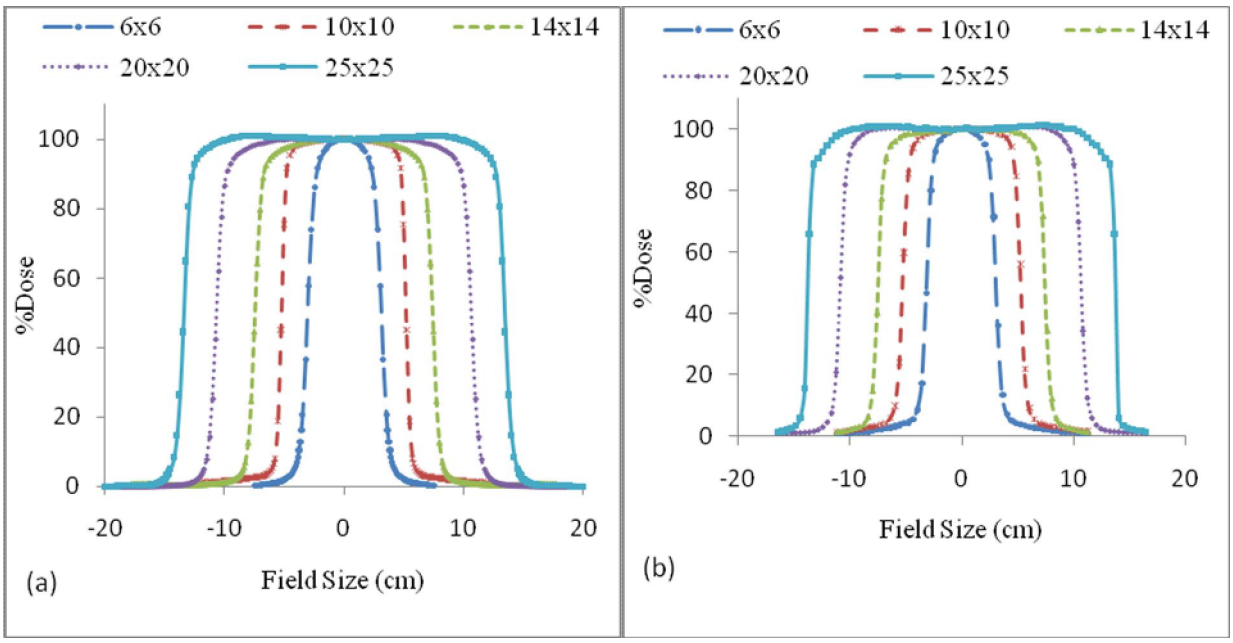

(vi): Beam profiles for 15 MeV measured at 1.0 cm depth. (a) 3D-water phantom. (b) Profiler 2 scanning system.

The following figures 5.6. (vii) to (x), show the 8 to 15 MeV electron beam profiles for the 3D-water phantom and profiler 2 scanning system measured at 2.0 cm depth respectively.

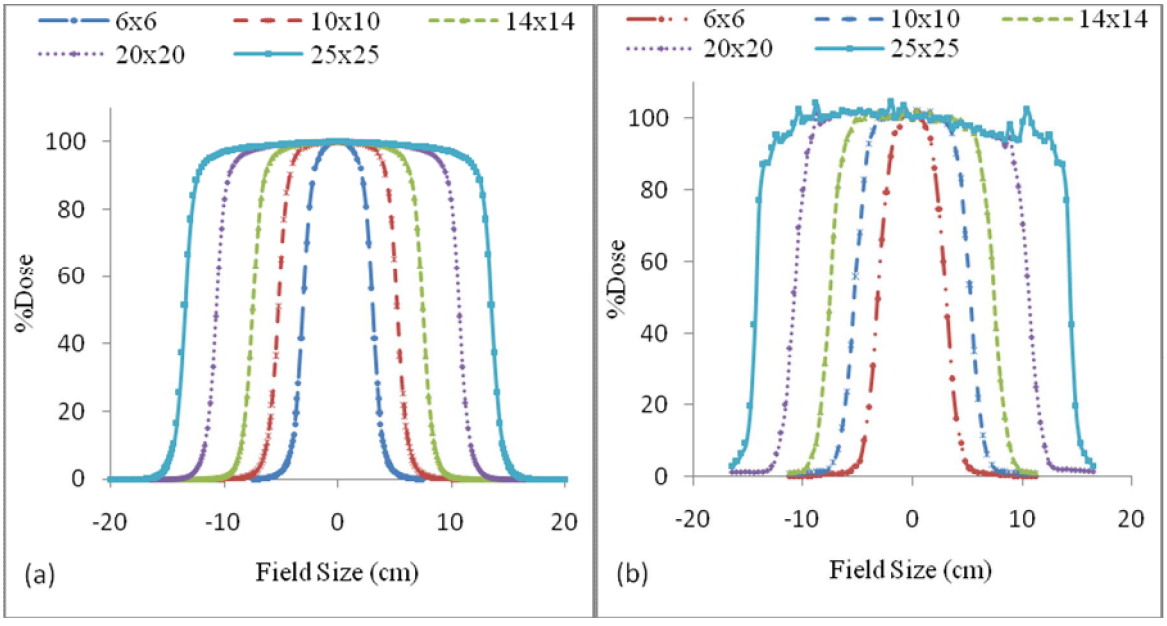

(vii): Beam profiles for 8 MeV measured at 2.0 cm depth. (a) 3D-water phantom. (b) Profiler 2 scanning system.

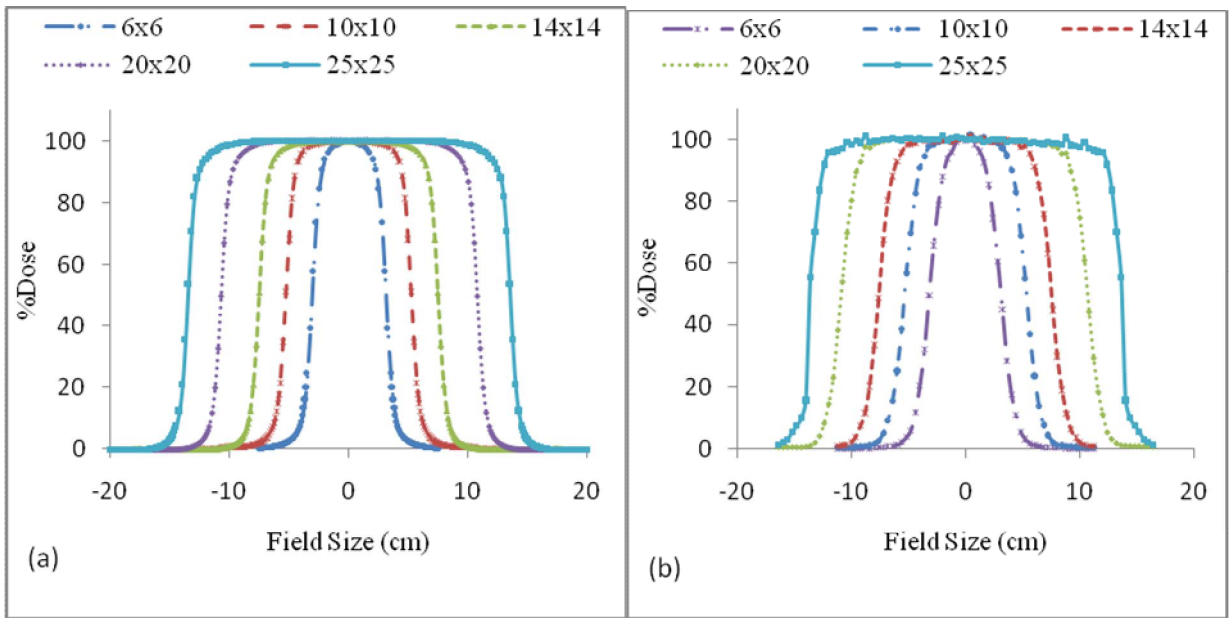

(viii): Beam profiles for 10 MeV measured at 2.0 cm depth. (a) 3D-water phantom. (b) Profiler 2 scanning system.

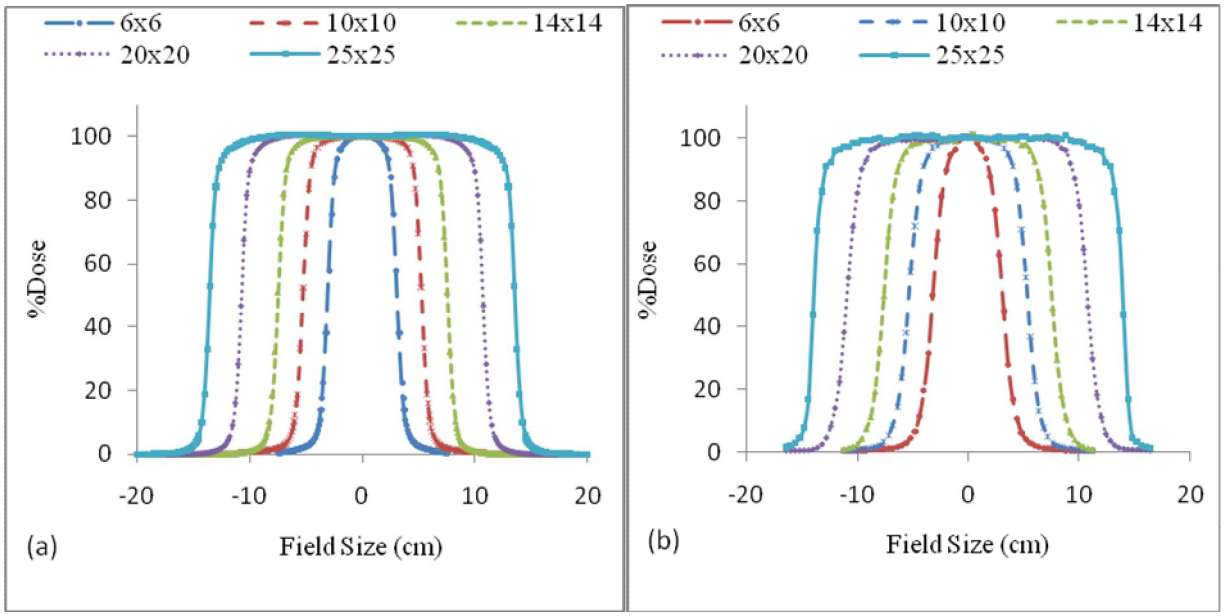

(ix): Beam profiles for 12 MeV measured at 2.0 cm depth. (a) 3D-water phantom. (b) Profiler 2 scanning system.

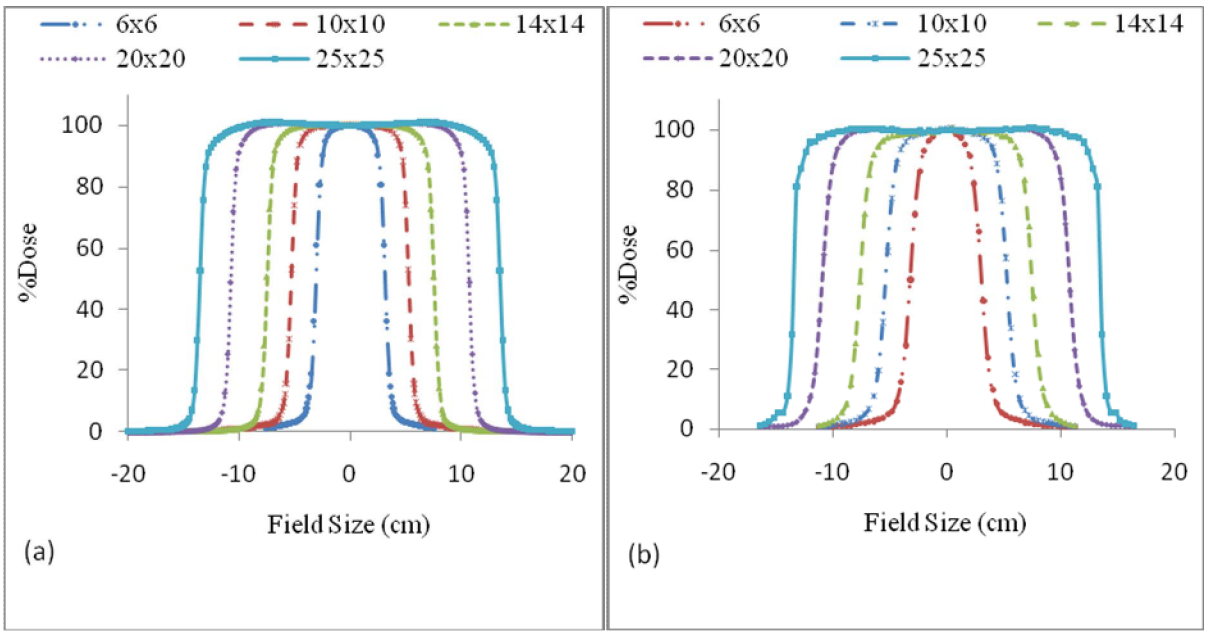

(x): Beam profiles for 15 MeV measured at 2.0 cm depth. (a) 3D-water phantom. (b) Profiler 2 scanning system.

The following figures 5.6. (xi) (a) and (b), show the 15 MeV electron beam profiles for the 3D-water phantom and profiler 2 scanning system measured at 5.0 cm depth respectively.

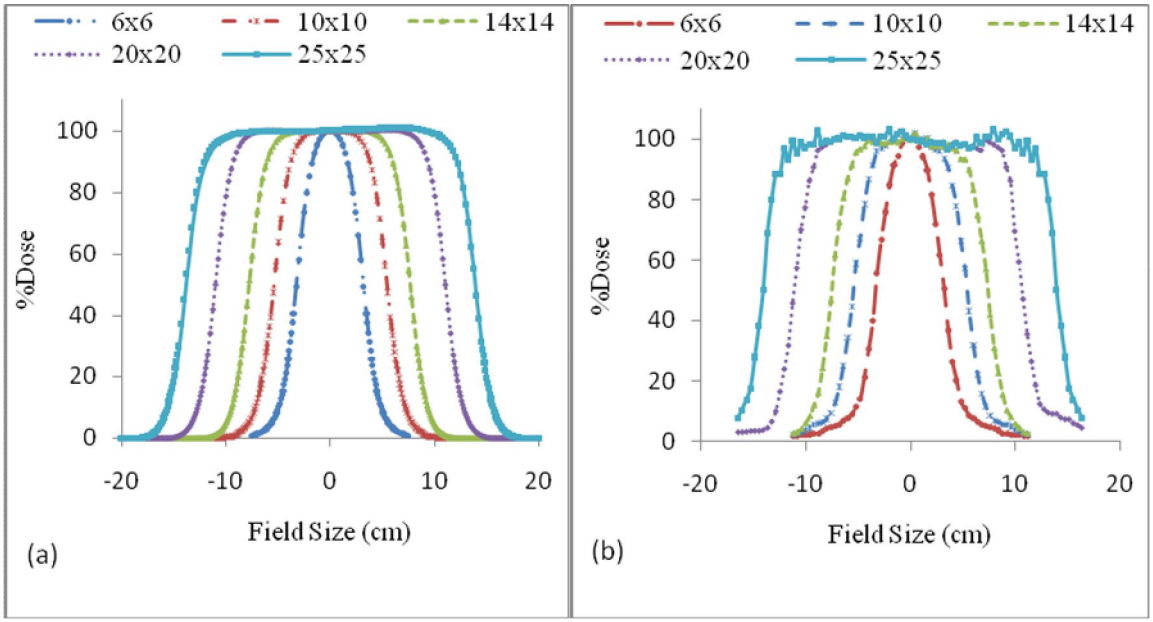

(xi): Beam profiles for 15 MeV measured at 5.0 cm depth. (a) 3D-water phantom. (b) Profiler 2 scanning system.

From these figures 5.8 (i) to (xi), it was evident that the profiler 2 scanning system beam profiles for the electron beams measured for different field sizes at different depths followed the same trend as for the 3D-water phantom beam profiles, except that for electron beams the profiles are prolonged on the 3D-water phantom at the wash-out region as compared to the profiler 2 scanning system profiles. This could be due to the less sensitivity of detector diodes to electron beam. In general, the beam profiles for the 25 × 25 cm^2 field size for the profiler 2 scanning system presents with noise in the uniform area.

The following figures 5.8 (xii) and (xiv), show the comparison between the 3D-water phantom and profiler 2 scanning system beam profiles for all field sizes measured 1.0 cm depth respectively.

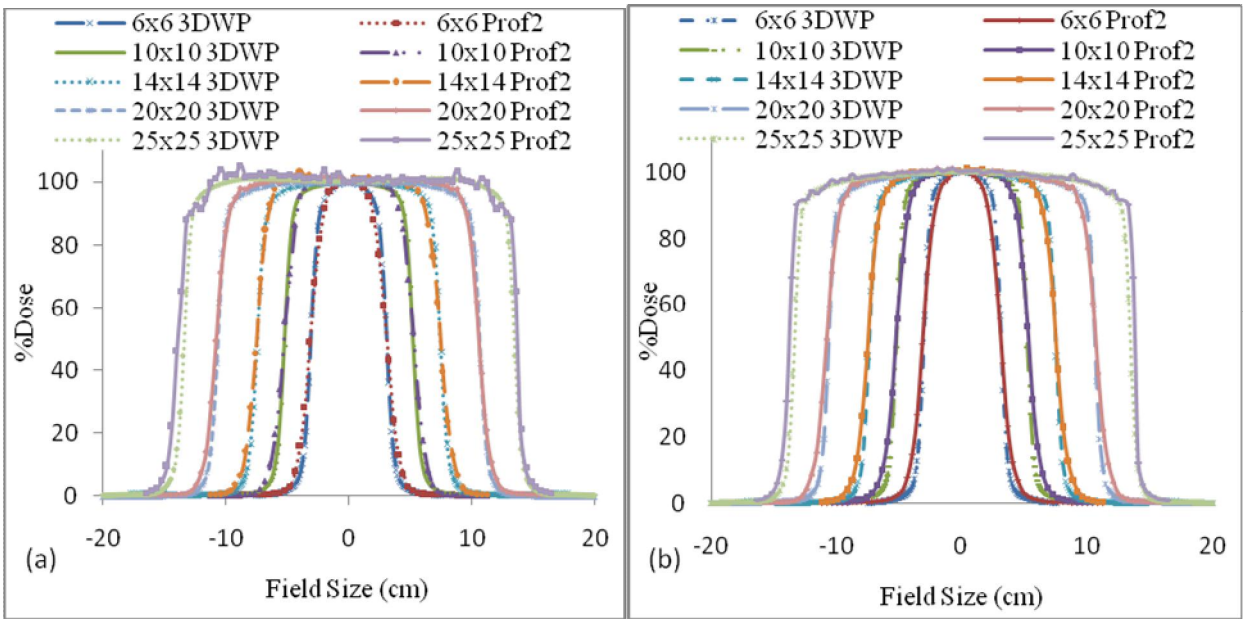

(xii): Comparison of beam profiles measured at 1.0 cm depth. (a) 6 MeV electron beam. (b) 8 MeV electron beam.

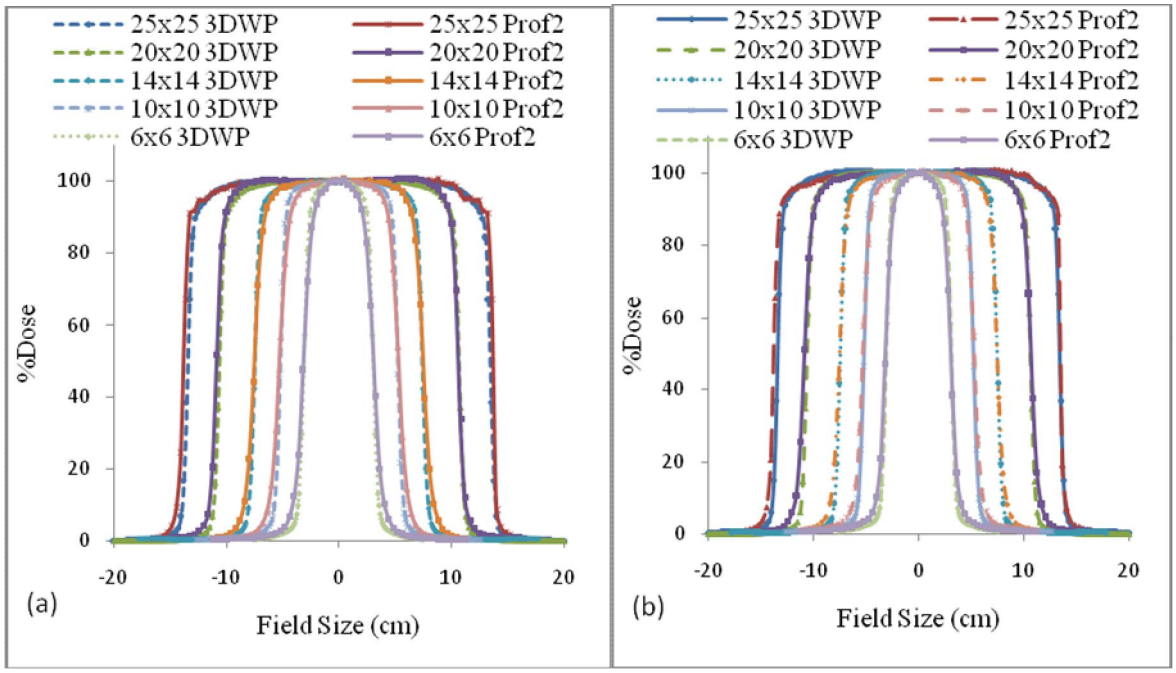

(xiii): Comparison of beam profiles measured at 1.0 cm depth. (a) 10 MeV electron beam. (b) 12 MeV electron beam.

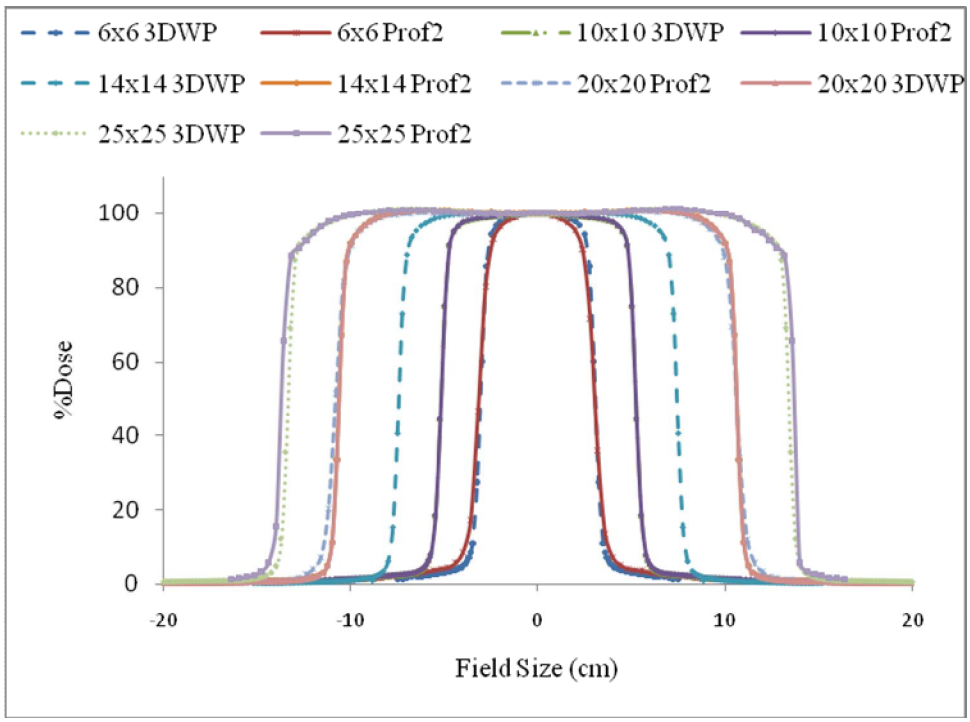

(xiv): Comparison of beam profiles measured at 1.0 cm depth for the 15 MeV electron beam.

From figures 5.8 (xii) and (xiv) one can deduce that the comparison was good well within recommended limits of 2 mm (± 2 %). The differences in the horn areas (areas of high dose) were within 2 mm (± 2 %), the penumbra regions (edges of the beam) were also within 2 mm (± 2 %), as well as in the wash-out areas (areas of dose variation as a result of both leakage and scatter from the collimator system). Elder P. J. *et al* (1995) has found an agreement to within 1.5 % for the ionization chamber measurements and the solid state detector beam profiles, whilst Leavitt D. D. *et al* (1990) has found a maximum difference of 2.7 %. In general, one can say the noise in the beam profiles for the profiler 2 scanning system for the 25 × 25 cm^2 can also be due to some statistical error and electronic instability in the diode detector or variations in the sensitivity of the detectors as stated by Elder P. J. *et al* (1995).

5.4.2. PDDs for electron beams.

The following figures 5.9 (i) to (v), shows the PDDs for all field sizes measured in the 3D-water phantom and Perspex (calibration) block for electron beam energies.

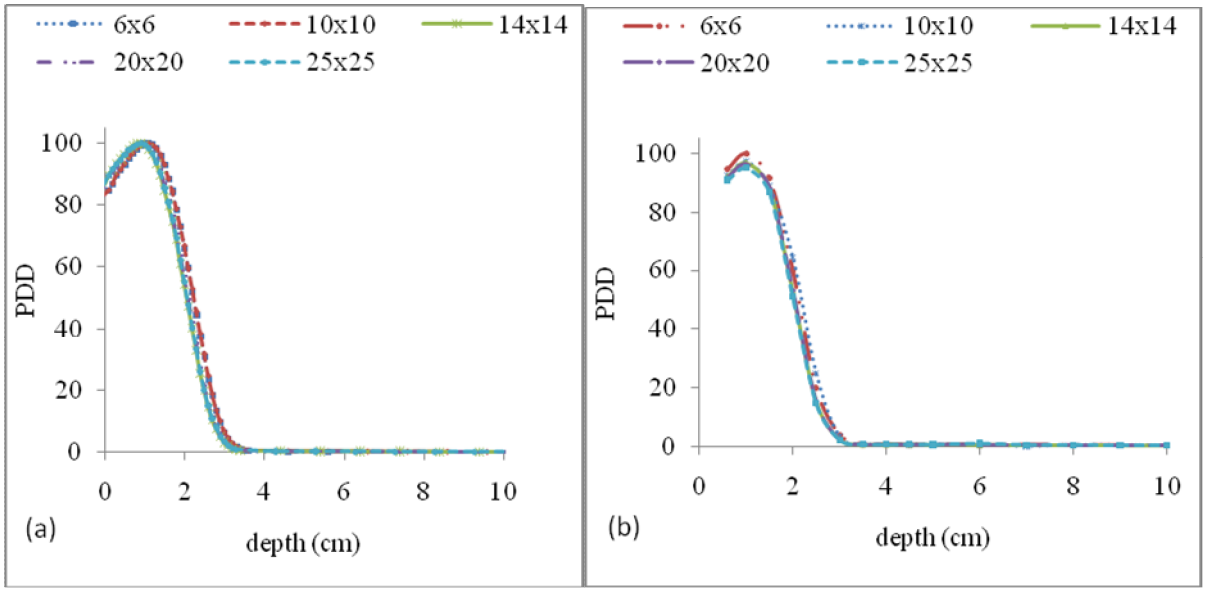

Figure 5.9 (i): Measured PDDs for 6 MeV. (a) 3D-water phantom. (b) Perspex block.

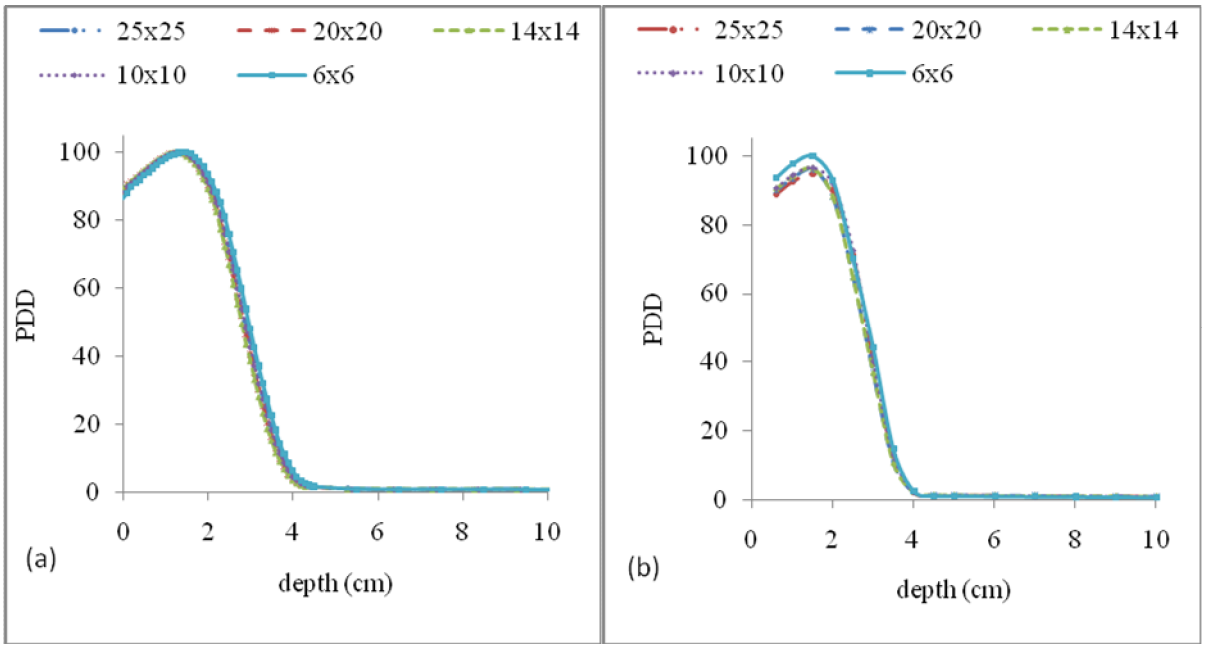

(ii): Measured PDDs for 8 MeV. (a) 3D-water phantom. (b) Perspex block.

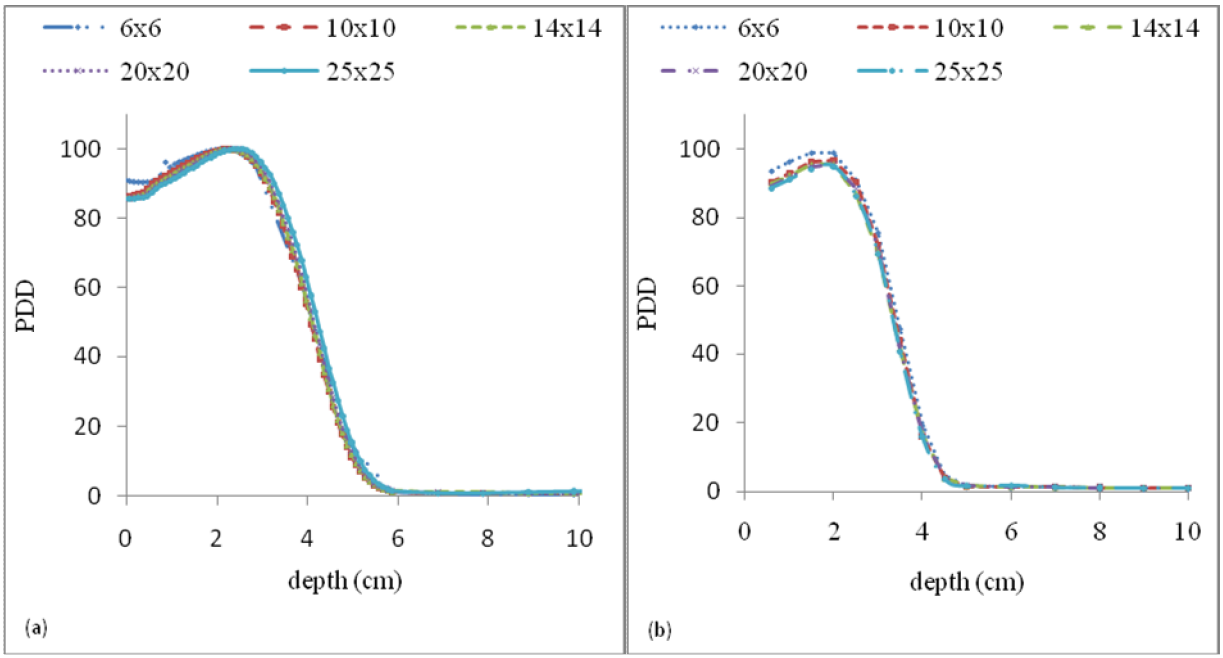

(iii): Measured PDDs for 10 MeV. (a) 3D-water phantom. (b) Perspex block.

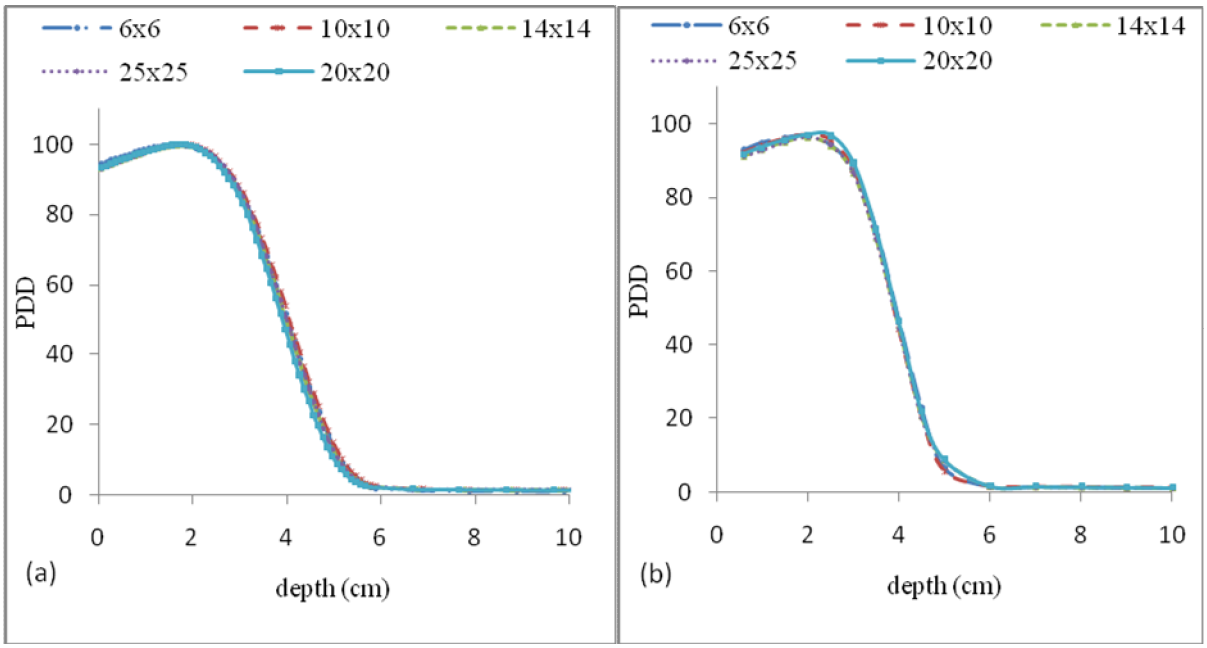

(iv): Measured PDDs for 12 MeV. (a) 3D-water phantom. (b) Perspex block.

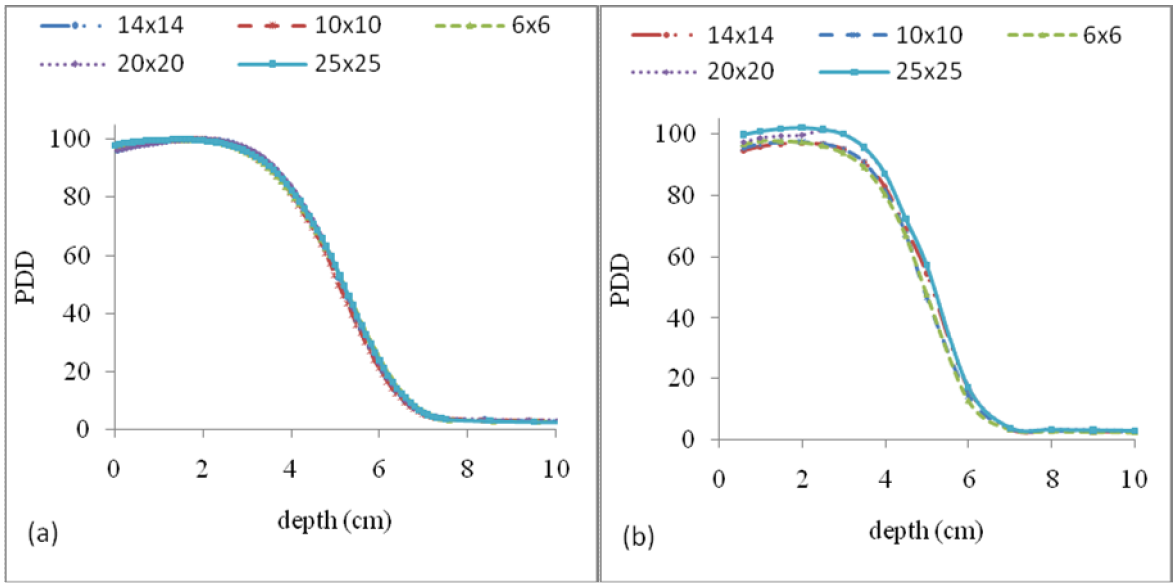

(v): Measured PDDs for 15 MeV. (a) 3D Water phantom. (b) Perspex block.

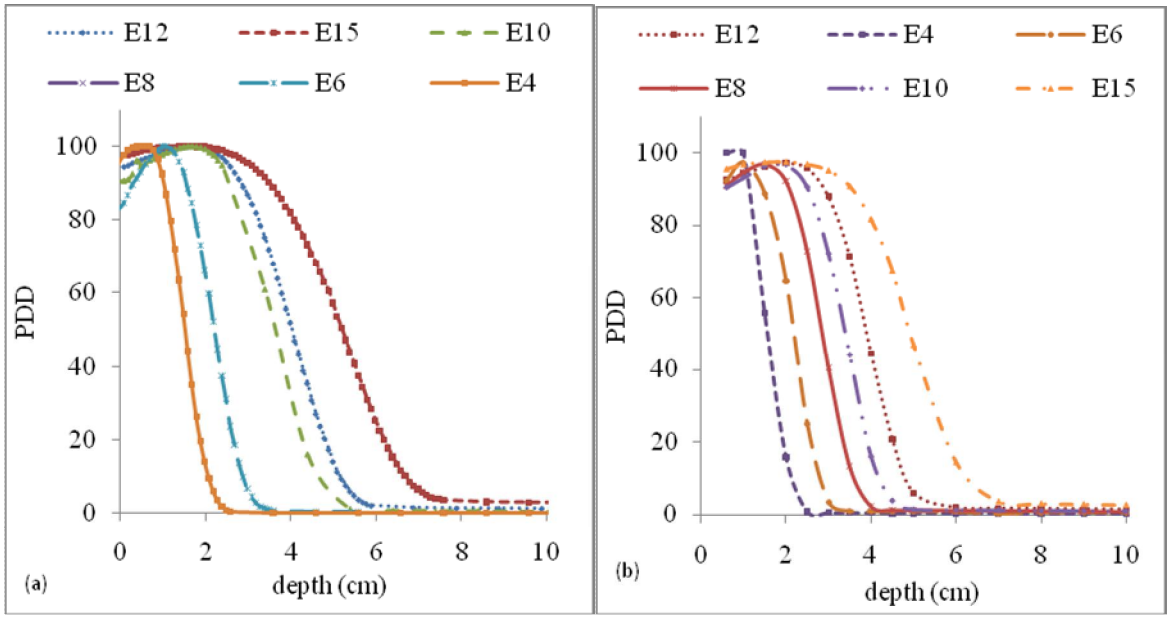

(vi). Comparison of PDDs for all electron beam energies. (a) 3D-water phantom. (b) Perspex block.

From figures 5.9 (i) to (vi), it was evident that the Perspex block PDD measurements follow the same trend as the 3D-water phantom measurements as expected. There was a shift in the buildup region for the Perspex block measurements due to the inherent buildup of 0.6 cm in the Perspex block. Therefore the Perspex block can be used to measure PDDs comparable to the 3D-water phantom PDDs provided some corrections are applied, like depth correction and density of water to Perspex correction. PDDs were also measured up to the depth of 10 cm due to the limited availability of Perspex slabs.

5.5. Analysis of tables.

The following tables are the results of the analysis of the comparison of the beam data profiles and PDDs between the 3D-water phantom and the profiler 2 scanning system (Perspex block).

Table 1: Comparison of beam profiles for the 6 MV photon beam at 0.5 cm depth.

	3D-water phantom				Profiler 2 scanning system				Differences			
FS (cm)	Δ_4 (%)	Δ_3 (%)	F_r (cm)	RW_{50} (cm)	Δ_4 (%)	Δ_3 (%)	F_r (cm)	RW_{50} (cm)	Δ_4 (%)	Δ_3 (%)	F_r (cm)	RW_{50} (cm)
6×6	0	0.33	0.433	0.058	0.3	1.3	0.400	-0.05	0.3	0.97	-0.033	0.008
10×10	0	1.48	0.476	0.104	0.3	0.8	0.410	-0.06	0.3	-0.68	-0.066	0.044
14×14	0	2.43	0.507	0.207	0.3	2.2	0.410	-0.11	0.3	-0.23	-0.097	0.097
20×20	0	3.48	0.588	0.287	0.3	3.7	0.315	-0.10	0.3	0.22	-0.273	0.187
25×25	0	5.43	0.609	0.273	1.6	7.7	0.275	0.16	1.6	2.27	-0.334	0.113

Table 2: Comparison of beam profiles for the 15 MV photon beam at 0.5 cm depth.

	3D-water phantom				Profiler 2 scanning system				Differences			
FS (cm)	Δ_4 (%)	Δ_3 (%)	F_r (cm)	RW_{50} (cm)	Δ_4 (%)	Δ_3 (%)	F_r (cm)	RW_{50} (cm)	Δ_4 (%)	Δ_3 (%)	F_r (cm)	RW_{50} (cm)
6×6	0	0.72	0.457	0.065	1.3	0.7	0.435	-0.04	1.3	-0.02	-0.022	0.025
10×10	0	1.41	0.526	0.149	1.5	1.7	0.43	-0.03	1.5	0.29	-0.096	0.119
14×14	0	3.65	0.707	0.305	1.5	3.5	0.46	-0.01	1.5	-0.15	-0.247	0.295
20×20	0	5.90	1.158	0.399	1.5	4.9	0.43	-0.06	1.5	-1.00	-0.728	0.339
25×25	0	7.13	1.506	0.373	0.5	9.6	0.295	0.17	0.5	2.47	-1.211	0.203

Table 3: Comparison of beam quality for the 6 and 15 MV photon beams for a 10 × 10 cm^2 field size.

	PDD_{10} (%)				
Energy (MV)	**Standard (%)**	**3D-water phantom (%)**	**Diff. (%)**	**Perspex block (%)**	**Diff. (%)**
6	**67.5**	67.04	-0.46	69.19	1.69
15	**76.5**	74.97	-1.53	77.76	1.26

Table 4: Comparison of beam quality for all electron beams for a 10 × 10 cm^2applicator size.

	R_{80}(mm)			
Energy (MeV)	**Standard (mm)**	**3D-water phantom**	**Perspex Block (mm)**	**Diff. (mm)**
4	**13.3**	14.95	14.60	0.35
6	**20.0**	20.60	20.03	0.57
8	**26.7**	28.04	27.49	0.55
10	**35.0**	34.21	33.15	1.06
12	**40.0**	40.89	38.47	2.42
15	**50.0**	50.59	48.31	2.28

Table 5: Comparison of beam profiles for the 4 MeV electron beam at 0.5 cm depth.

	3D-water phantom				Profiler 2 scanning system				Differences			
FS (cm)	Δ_4 (%)	Δ_3 (%)	F_r (cm)	RW_{50} (cm)	Δ_4 (%)	Δ_3 (%)	F_r (cm)	RW_{50} (cm)	Δ_4 (%)	Δ_3 (%)	F_r (cm)	RW_{50} (cm)
6 × 6	0	0.00	1.058	0.210	1.2	2.0	1.115	0.16	1.2	2.00	0.057	0.370
10 × 10	0	0.03	0.949	0.381	0.3	2.8	1.050	0.32	0.3	2.77	0.101	0.701
14 × 14	0	0.00	1.018	0.793	0.2	2.1	1.130	0.74	0.2	2.10	0.112	1.533
20 × 20	0	0.12	0.950	1.135	0.4	1.9	1.260	1.13	0.4	1.78	0.31	2.265
25 × 25	0	0.66	0.963	1.678	0.4	2.8	2.440	2.12	0.4	2.14	1.477	-0.442

Table 6: Comparison of beam profiles for the 6 MeV electron beam at 0.5 cm depth.

	3D-water phantom				Profiler 2 scanning system				Differences			
FS (cm)	Δ_4 (%)	Δ_3 (%)	F_r (cm)	RW_{50} (cm)	Δ_4 (%)	Δ_3 (%)	F_r (cm)	RW_{50} (cm)	Δ_4 (%)	Δ_3 (%)	F_r (cm)	RW_{50} (cm)
6 × 6	0	0.00	0.886	0.176	0.5	1.0	1.025	0.13	0.5	1.00	0.139	0.306
10 × 10	0	0.00	0.747	0.375	0.0	1.1	1.010	0.39	0.0	1.10	0.263	0.765
14 × 14	0	0.00	0.794	0.781	0.2	1.3	1.010	0.79	0.2	1.30	0.216	1.571
20 × 20	0	0.12	0.759	1.168	0.1	1.2	1.180	1.22	0.1	1.08	0.421	2.388
25 × 25	0	0.54	0.756	1.702	0.2	2.0	2.450	1.84	0.2	1.46	1.694	-0.138

Table 7: Comparison of beam profiles for the 8 MeV electron beam at 0.5 cm depth.

	3D-water phantom				Profiler 2 scanning system				Differences			
FS (cm)	Δ_4 (%)	Δ_3 (%)	F_r (cm)	RW_{50} (cm)	Δ_4 (%)	Δ_3 (%)	F_r (cm)	RW_{50} (cm)	Δ_4 (%)	Δ_3 (%)	F_r (cm)	RW_{50} (cm)
6 × 6	0	0.00	0.773	0.149	0.5	0.3	0.865	0.110	0.5	0.30	0.092	0.259
10 × 10	0	0.00	0.696	0.354	0.5	0.7	0.900	0.370	0.5	0.70	0.204	0.724
14 × 14	0	0.00	0.730	0.775	0.4	0.7	0.990	0.780	0.4	0.70	0.260	1.555
20 × 20	0	0.06	0.722	1.103	0.5	0.4	1.100	1.200	0.5	0.34	0.378	2.303
25 × 25	0	0.03	0.692	1.627	0.1	0.8	2.400	1.671	0.1	0.77	1.708	-0.044

Table 8: Comparison of beam profiles for the 10 MeV electron beam at 0.5 cm depth.

	3D-water phantom				Profiler 2 scanning system				Differences			
FS (cm)	Δ_4 (%)	Δ_3 (%)	F_r (cm)	RW_{50} (cm)	Δ_4 (%)	Δ_3 (%)	F_r (cm)	RW_{50} (cm)	Δ_4 (%)	Δ_3 (%)	F_r (cm)	RW_{50} (cm)
6 × 6	0	0.00	0.637	0.133	0.4	0.1	0.725	0.10	0.4	0.10	0.088	0.233
10 × 10	0	0.00	0.572	0.349	0.6	0.6	0.760	0.37	0.6	0.60	0.188	0.719
14 × 14	0	0.00	0.590	0.783	0.5	0.8	0.780	0.78	0.5	0.80	0.190	1.563
20 × 20	0	0.00	0.567	1.144	0.1	0.3	0.930	1.21	0.1	0.30	0.363	2.354
25 × 25	0	0.12	0.558	1.666	0.3	0.2	2.230	1.69	0.3	0.08	1.672	-0.024

Table 9: Comparison of beam profiles for the 12 MeV electron beam at 0.5 cm depth.

	3D-water phantom				Profiler 2 scanning system				Differences			
FS (cm)	Δ_4 (%)	Δ_3 (%)	F_r (cm)	RW_{50} (cm)	Δ_4 (%)	Δ_3 (%)	F_r (cm)	RW_{50} (cm)	Δ_4 (%)	Δ_3 (%)	F_r (cm)	RW_{50} (cm)
6 × 6	0	0.00	0.640	0.155	0.2	0.4	0.645	0.10	0.2	0.40	0.005	0.255
10 × 10	0	0.00	0.589	0.379	0.5	0.8	0.650	0.37	0.5	0.80	0.061	0.749
14 × 14	0	0.16	0.612	0.762	0.4	0.7	0.700	0.78	0.4	0.54	0.088	1.542
20 × 20	0	0.36	0.581	1.110	1.2	0.6	0.890	1.20	1.2	0.24	0.309	2.310
25 × 25	0	0.65	0.555	1.629	1.0	1.1	1.750	1.64	1.0	0.45	1.195	-0.011

Table 10: Comparison of beam profiles for the 15 MeV electron beam at 0.5 cm depth.

	3D-water phantom				Profiler 2 scanning system				Differences			
FS (cm)	Δ_4 (%)	Δ_3 (%)	F_r (cm)	RW_{50} (cm)	Δ_4 (%)	Δ_3 (%)	F_r (cm)	RW_{50} (cm)	Δ_4 (%)	Δ_3 (%)	F_r (cm)	RW_{50} (cm)
6 × 6	0	0.03	0.558	0.153	0.3	0.0	0.555	0.11	0.3	-0.03	-0.003	0.263
10 × 10	0	0.00	0.475	0.365	0.3	0.2	0.530	0.36	0.3	0.20	0.055	0.725
14 × 14	0	0.30	0.484	0.783	0.6	0.8	0.600	0.77	0.6	0.50	0.116	1.553
20 × 20	0	0.88	0.477	1.148	0.1	1.0	0.690	1.17	0.1	0.12	0.213	2.318
25 × 25	0	1.32	0.489	1.644	0.0	1.2	1.030	1.60	0.0	-0.12	0.541	0.044

From tables 1 and 2, the maximum difference in symmetry was 1.6 % for the 6 MV photon beam for the 25 × 25 cm^2 field size and 1.5 % for the 15 MV photon beam for field sizes (10 × 10 cm^2, 14 × 14 cm^2 and 20 × 20 cm^2). The maximum difference in flatness was 2.27 % for the 6 MV photon beam for a 25 × 25 cm^2 field size and 2.47 % for the 15 MV photon beam for a 25 × 25 cm^2 field size, which were well within the recommended limit of ± 3 %. The penumbra maximum difference was -0.334 cm for the 6 MV photon beam for a 25 × 25 cm^2 and for the 15 MV photon beam was -1.211 cm for a 25 × 25 cm^2 which was just outside the recommended limit of 1.2 cm and this can be due to insufficient scatter contribution from the profiler 2 scanning system. The field size maximum difference was 0.187 cm for the 6 MV photon beam for a 20 × 20 cm^2 and 0.339 cm for the 15 MV photon beam for a 20 × 20 cm^2which were well within the recommended limit of 0.2 cm for smaller field sizes and 0.4 cm for a 20 × 20 $cm^2$and for larger field sizes. It was evident that the 6 MV photon beam flatness for the field sizes 20 × 20 cm^2 and 25 × 25 cm^2 needed to be adjusted, same as for the 15 MV photon beam, the flatness of the field sizes 14 × 14 cm^2, 20 × 20 cm^2 and 25 × 25 cm^2 also needed to be adjusted.

From table 3,the largest difference in PDD_{10} was 1.69 % from the standard value for a 6 MV and 1.26 % for the 15 MV photon beam as argued by Kosunen A. *et al* (1993) that PDD_{10} is a better beam quality specifier since a pure photon beam specifies stopping power ratios within 0.2 % for all thick target bremsstrahlung. It maintains its sensitivity for high energy beams and has a simple physical and clinical meaning than $TPR_{20,10}$, because stopping power ratios for the same value of $TPR_{20,10}$ can vary by up to 0.7 % for thick target bremsstrahlung beams. The value of $TRP_{20,10}$ becomes insensitive to beam quality changes for high energy beams and it has little intuitive meaning. From table 4, the deviation in R_{80} values (PDD values near the end of the electron range) compared very well to within 2 mm with the standard values for all electron energies as stated by King R. P. *et al* (2000), except for the 12 and 15 MeV electron beams when the 3D-water phantom is compared to profiler 2 scanning system. The highest difference of 2.28 mm was obtained with the 15 MeV electron beam and 2.42 mm for the 12 MeV electron beam.

From tables 5 to 10, the maximum difference in symmetry was 1.2 % for the 4 MeV electron beam for the 6 × 6 cm^2 applicator size and for the 12 MeV electron beam for the applicator size of 20 × 20 cm^2. The maximum difference in flatness was 2.77 % for the 4 MeV electron beam for a 10 × 10 cm^2 applicator size which were within the recommended limit of ± 3 %. The penumbra maximum difference was 1.708 cm for the 8 MeV electron beam for a 25 × 25 cm^2 applicator size which was outside the limit of 1.2 cm and the maximum field size difference was 2.388 cm for the 6 MeV electron beam for a 20 × 20 cm^2 applicator size, which was outside the recommended limit of 0.4 cm. In general the field size difference was out of the recommended limit for all electron energies for the field sizes 14 × 14 cm^2 and 20 × 20 cm^2.

5.6. Validation of beam data.

The beam data were validated by exporting the 10 × 10 cm^2 field size profiles measured at 1.0 cm depth and PDDs to CMS XiO TPS for modeling. After modeling, data was exported back to excel spreadsheet for comparison. This comparison was achieved by superimposing these beam data for all three systems (3D-water phantom, profiler 2 scanning system and CMS XiO treatment planning system).

The following figures show the comparisons of beam data.

5.6.1. Photon beams (Profiles).

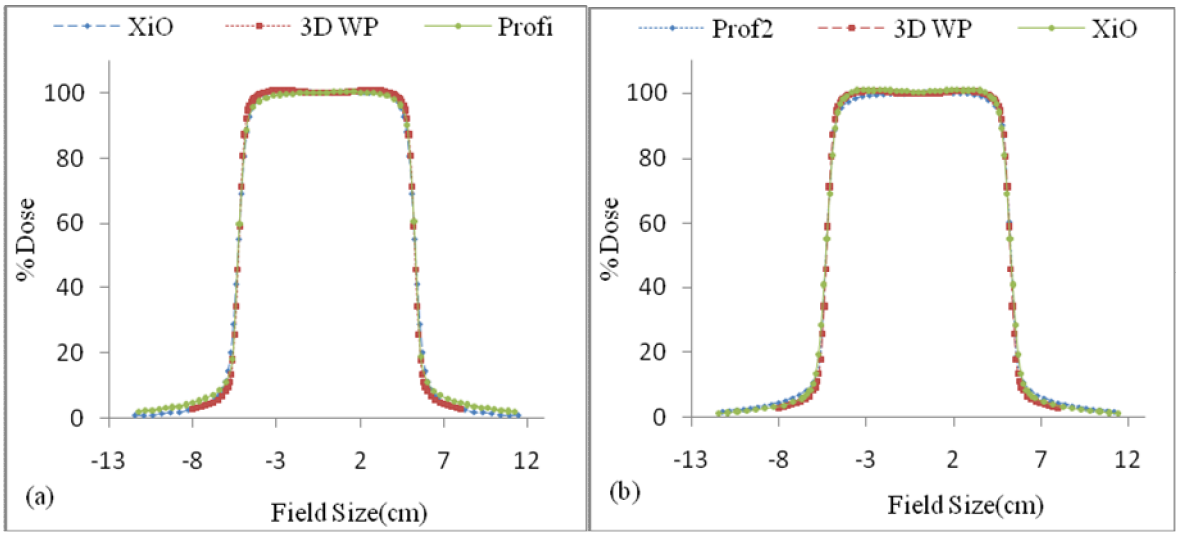

Figure 5.10: Comparison of the 3D-water phantom, profiler 2 scanning system and CMS XiO TPS photon beam profiles for the 10×10 cm^2 field size measured at 5.0 cm depth.(a) 15 MV. (b) 6 MV.

From figure 5.10, it was evident that the comparison between the 3D-water phantom, profiler 2 scanning system and CMS XiO TPS beam profiles for both the 6 and 15 MV photon beams was good to within 1 mm (± 1 %) with the limit of ± 3 % (3 mm) as recommended by CMS XiO TPS for the 10 × 10 cm^2 field size measured at 5.0 cm depth. Therefore this validate that the profiler 2 scanning system to be used as a substitute for the 3D-water phantom for profile measurements.

5.6.2. Photon beams (PDDs).

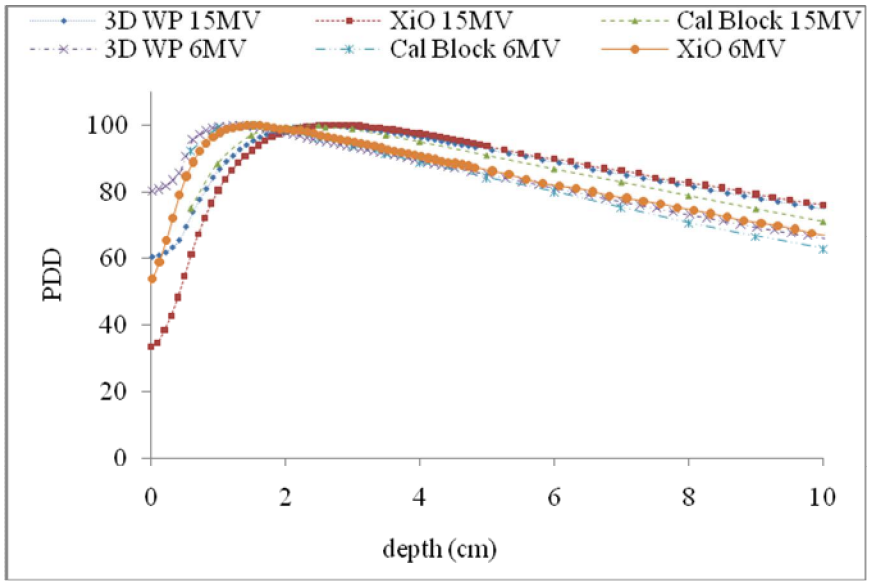

Figure 5.11: Comparison of the 3D-water phantom, Perspex block and CMS XiO TPS PDDs for the 10 × 10 cm^2 for the 6 and 15 MV photon beams.

From figure 5.11, one can deduce that the PDD measurements comparison for the 3D-water phantom, Perspex block and XiO CMS TPS was very well within recommended limits especially at the depth of maximum dose (d_{max}) and at depth up to 5 cm. The deviation was outside the recommended limit at the buildup region and becomes worse at depths larger than 5 cm with the Perspex block. This simply meant that the Perspex block cannot be used to substitute the 3D-water phantom for PDD measurements for commissioning of a linear accelerator, but only as a rough estimate for the energy checks in quality assurance measurements.

5.6.3. Electron beams (Profiles).

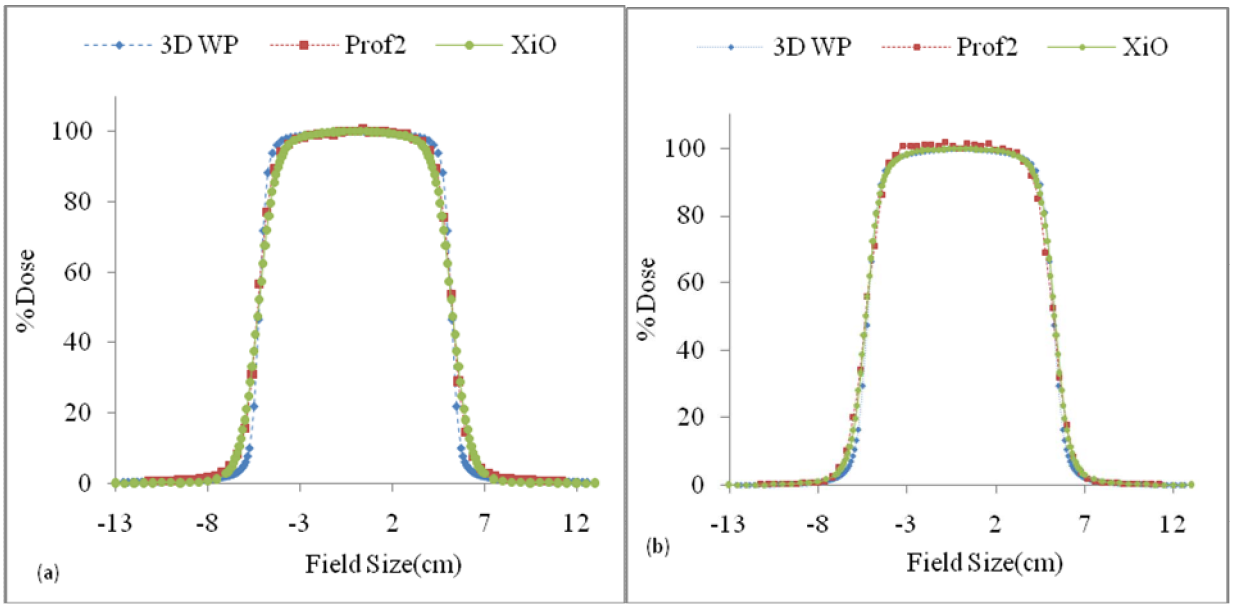

Figure 5.12 (i): Comparison of the 3D-water phantom, profiler 2 scanning system, and CMS XiO TPS electron beam profiles for the 10 × 10 cm^2 field sizes measured at 1.0 cm depth. (a) 4 MeV. (b) 6 MeV.

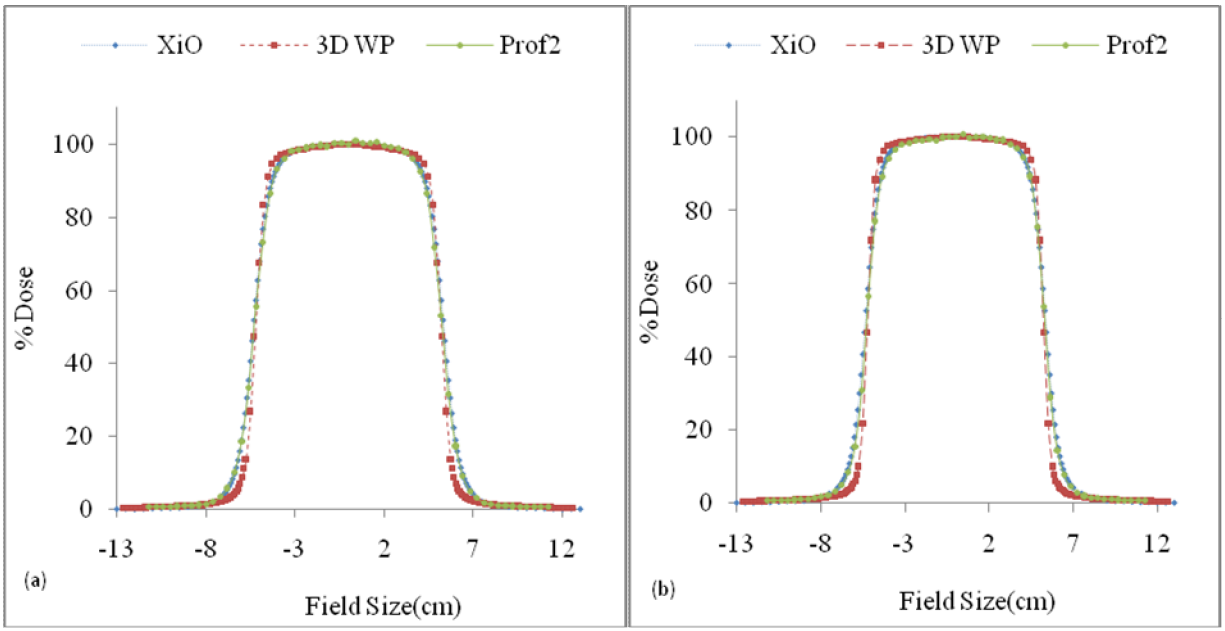

(ii): Comparison of the 3D-water phantom, profiler 2 scanning system, and CMS XiO TPS electron beam profiles for the 10 × 10 cm^2 field sizes measured at 1.0 cm depth. (a) 8 MeV. (b) 10 MeV.

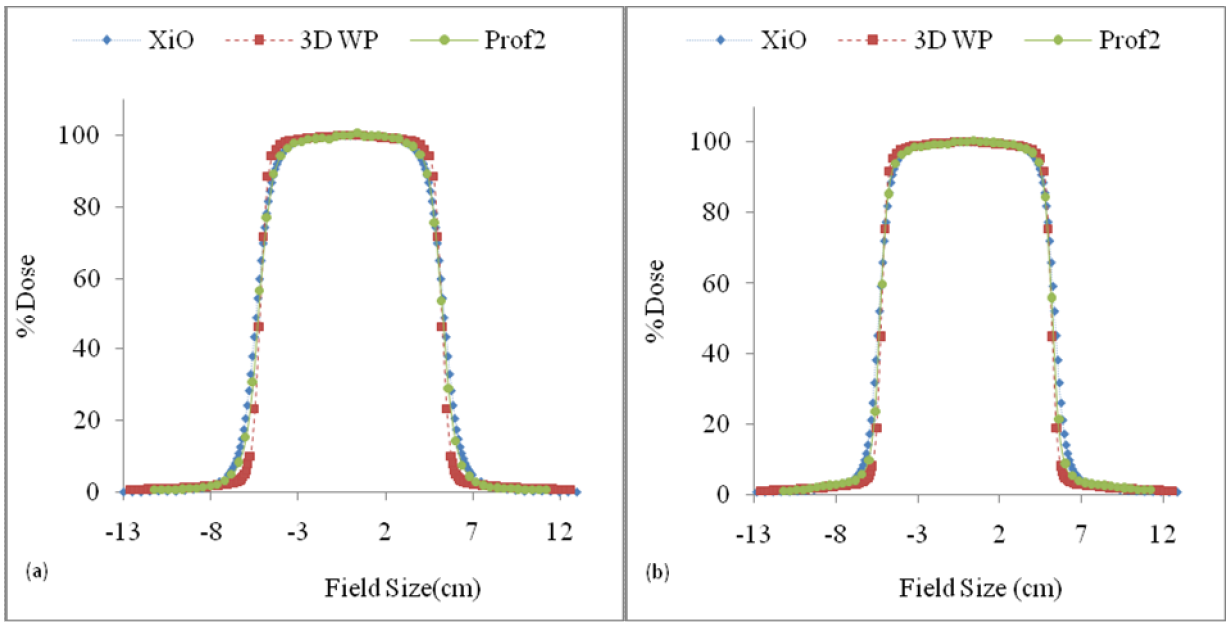

(iii): Comparison of the 3D-water phantom, profiler 2 scanning system, and CMS XiO TPS electron beam profiles for the 10 × 10 cm^2 field sizes measured at 1.0 cm depth. (a) 12 MeV. (b) 15 MeV.

From figures 5.12 (i) to (iii), it was evident that the comparison between the 3D-water phantom, profiler 2 scanning system and CMS XiO TPS beam profiles for all electron beam energies was good with a slight shift of the profiler 2 scanning system profiles from the 3D-water phantom and CMS XiO TPS both at the horns and at the penumbra region within recommended limit of ± 3 % (3 mm) as recommended by CMS XiO TPS. Therefore this validate that the profiler 2 scanning system to be used as a substitute for the 3D-water phantom for profile measurements.

5.6.4. Electron beams (PDDs).

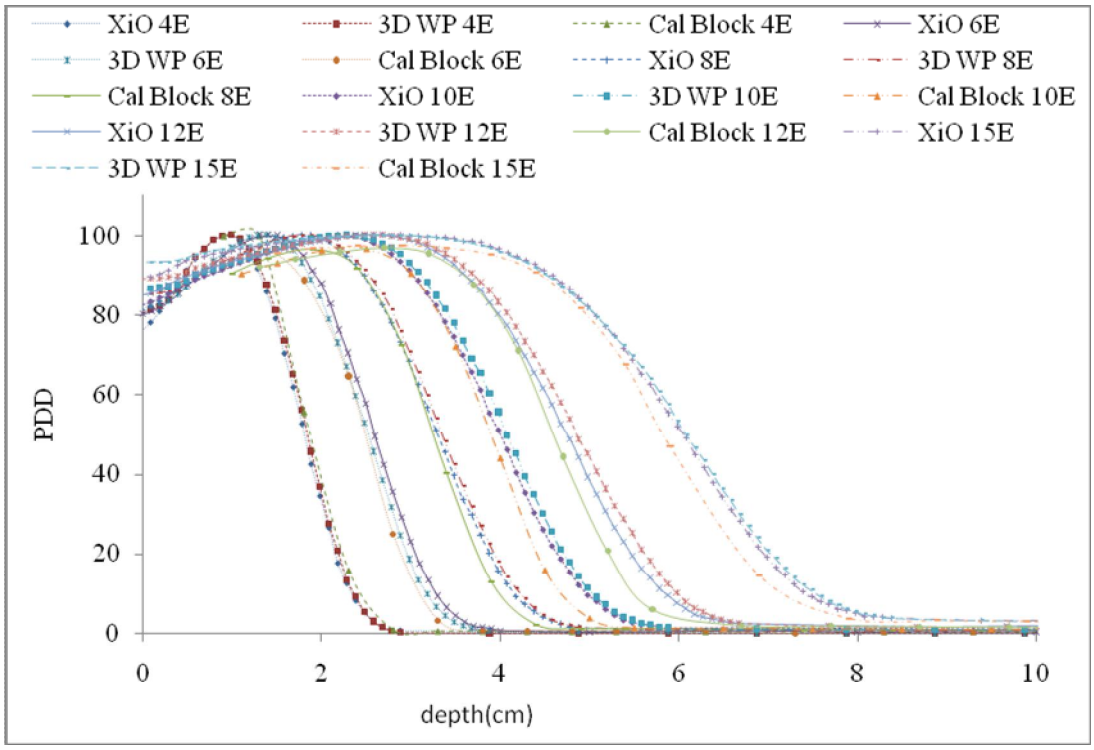

Figure 5.13: Comparison of the 3D-water phantom, the Perspex block and CMS XiO TPS PDDs for the 10 × 10 cm^2applicator size for all electron energies (4, 6, 8, 10, 12 and15MeV).

From figure 5.13 it was evident that as the energy of the electron increases, the particles scattered from the insert (applicator size) with enough energy to reach the point of measurement, thus the outer-scatter electrons are compensated by in-scatter electrons (from the insert edges) virtually maintaining constant particle fluence at the depth of measurement as stated by Turian J. V. *et al* (2004). The deviations appear to be larger for depths beyond the R_{50}. From table 10, the 12 MeV and 15 MeV R_{80}*'s* were outside the tolerance limit of 1 mm with 2.42 mm for the 12MeV and 2.28 mm for the 15 MeV. However Turian J. V. *et al* (2004) has also reported a maximum γ index of 1.154 for the 9 MeV electron beam which correspond to a maximum difference of about 2.3 %, and for a 20 × 20 cm^2 applicator they reported a maximum γ index of 1.2 for the same electron beam which corresponds to a maximum difference of about 2.4 %.

5.7. Absolute dose comparisons.

The IAEA TRS-398 dosimetry protocol was followed for the determination of absolute dose measurements in water. The profiler 2 scanning system was calibrated such that it gives the dose output for all photon and electron energies under similar conditions (temperature and pressure) as the dosimetry measurements in water. The dose measurements were acquired for both systems over a period of three months with an error limit of ± 3 %.

The following table shows the results of absolute dose comparisons.

Table 11: Comparison of absolute dose measurements.

	Week 1	Week 3	Week 5	Week 7	Week 9	Week 11		
6MV	Dose (cGy)	Dose (cGy)	Dose (cGy)	Dose (cGy)	Dose (cGy)	Dose (cGy)	Average Dose	Standard Deviation
1D WP	100.00	100.70	99.90	100.10	100.50	99.80	**100.17**	**0.36**
Prof2	99.98	101.74	100.10	100.05	100.03	100.10	**100.33**	**0.69**
% Error	**0.20**	**-0.99**	**-0.20**	**0.05**	**0.47**	**-0.30**		
15MV								
1D WP	100.01	100.70	100.30	100.10	99.90	99.90	**100.15**	**0.31**
Prof2	99.99	100.43	100.00	99.80	100.01	100.09	**100.05**	**0.21**
% Error	**0.20**	**0.27**	**0.30**	**0.30**	**-0.11**	**-0.19**		
4MeV								
1D WP	99.99	100.60	99.80	99.90	100.10	100.00	**100.07**	**0.28**
Prof2	99.68	100.25	100.10	100.11	100.13	100.09	**100.06**	**0.20**
% Error	**0.31**	**0.35**	**-0.30**	**-0.21**	**-0.03**	**-0.09**		
6MeV								
1D WP	99.97	100.50	100.30	100.80	100.20	99.90	**100.28**	**0.34**
Prof2	99.63	100.06	100.02	100.21	99.69	99.84	**99.91**	**0.23**
% Error	**0.34**	**0.44**	**0.28**	**0.59**	**0.51**	**0.06**		
8MeV								
1D WP	100.01	100.50	99.90	100.60	99.90	100.08	**100.17**	**0.31**
Prof2	99.95	99.90	99.910	100.02	100.20	100.09	**100.01**	**0.12**
% Error	**0.06**	**0.60**	**-0.01**	**0.58**	**-0.30**	**-0.01**		
10MeV								
1D WP	100.03	100.70	100.10	99.80	99.90	100.10	**100.11**	**0.31**
Prof2	99.98	100.49	99.95	99.99	100.01	100.23	**100.11**	**0.21**
% Error	**0.05**	**0.21**	**0.15**	**-0.19**	**-0.11**	**-0.13**		
12MeV								
1D WP	99.99	100.60	100.00	99.90	100.10	100.60	**100.20**	**0.32**
Prof2	100.01	100.90	100.50	100.21	100.31	100.37	**100.38**	**0.30**
% Error	**-0.02**	**-0.30**	**-0.50**	**-0.31**	**-0.21**	**0.23**		
15MeV								
1D WP	100.00	100.50	100.20	100.50	100.60	100.0	**100.30**	**0.27**
Prof2	99.69	100.27	99.95	99.99	99.91	100.02	**99.97**	**0.19**
% Error	**0.31**	**-0.23**	**0.25**	**0.51**	**0.67**	**-0.02**		

Absolute dose measurements were performed over three months to verify the accuracy, stability and precision of the profiler 2 scanning system. Table 11 showed the results of the dose measurements for all beam energies (6 and 15 MV photon beams and 4, 6, 8, 10, 12 and 15 MeV electron beams). The percentage errors were calculated for each beam energy at the time of measurements. Kilic A. *et al* (2002) showed that the 2D and 3D systems showed an average of -0.8 % and -1.0 % for 6 MV indicating underestimation of absorbed dose at a point of measurements and an average of +2.2 % and +1.4 % for 15 MV indicating overestimation of absorbed dose at a point of measurements. Paganetti H. (2006) has reported excellent agreement between absolute dose measurements between Monte Carlo (MC) simulation and physical measurements to 1.5 %, where about 50 % of the fields agreed to 1 %, and that were within the uncertainty of the data. Our study showed the maximum of -0.99 % for the 6 MV which indicated underestimation of the absorbed dose at a point of measurement in week 2, and the maximum average of + 0.27 % for the 15 MV which indicated an overestimation of the absorbed dose at a point of measurement in week 3. On average for electron beams, the maximum percentage error was shown for the 15 MeV which was + 0.67 % on week 5 indicating overestimation of the absorbed dose at a point of measurement on that week. The averages and standard deviations for each dose measurements were also calculated and the maximum standard deviation was + 0.69 for the 6 MV photon beam energy for the profiler 2 scanning system. Therefore this showed that the profiler 2 scanning system can be used to monitor the linear accelerator dose output constancy for the Elekta Synergy Platform linear accelerator over a period of time. This was also confirmed by Saminathan S. *et al* (2010) when they found a linear relation in dose between the 2D-ion chamber and the film.

CHAPTER 6

CONCLUSION AND FUTURE RECOMMENDATIONS.

The study aimed to establish whether the profiler 2 scanning system can be used to substitute the 3D-water phantom for commissioning of the linear accelerator. The objective was to compare dose distributions of the photon beams and electron beams from an Elekta Synergy Platform linear accelerator.

Therefore in general, the objectives of this study were achieved especially for the photon beam dose distributions with some uncertainties in some of the electron beams to within the recommended limit of ± 3 % (3 mm) according to CMS XiO treatment planning system. The ionization chambers gave accurate results as expected, but the data acquisition was very time consuming, thus the array diode detectors showed in general a good reasonable agreement with the ionization chamber measurements especially with beam profile measurements with some uncertainties generally with electron beams PDDs (Elder P. J. *et al* 1995).

From the measurements performed and the results obtained, it was evident that the profiler 2 scanning system can be used as a substitute for 3D-water phantom for measurements of linear accelerator beam dose distributions. The profiler 2 scanning system needs to be calibrated for linear array diode detectors and for dose measurements. These calibration factors are necessary for measurements of dose distributions. There are few limitations involved with the profiler 2 scanning system that were not investigated in this study.

Recommendations.

The dose distribution measurements using the profiler 2 scanning system are recommended for centers that wish to commission a linear accelerator similar to the one already on site so that beam matching of the linear accelerator can be assumed as well as accurate calibration of the profiler 2 scanning system.

The future study could be on the limitations of the profiler 2 scanning system, which are:

(i). Field size (maximum field size of 20 × 30 cm^2 at SSD = 100 cm of the profiler 2 scanning system) - which may be overcome by moving the profiler 2 scanning system closer to the source (linear accelerator head) for scanning the field size of 40 × 40 cm^2 or by scanning the half profiles and mirror imaging them.

(ii). Number of Perspex slabs to be placed on top of the profiler 2 scanning system - which restricts for measurements at deeper depth and this can be overcome by manufacturing a stand holder for Perspex plates.

(iii). Measurements of diagonal profiles-which can be overcome by rotating the collimator head of the linear accelerator through 45°.

REFERENCES

Alber M, Broggi S, De Wagter C. *et al* 2008. Guidelines for the verification of IMRT. The Netherlands Cancer Institude-Antoni van Leeuwenhoek Hospital, Amsterdam. 1-136.

Ali O, Willemse C. A, Shaw W, du Plessis F. C. P. *et al* 2011. Monte Carlo electron source model validation for an Elekta Precise linac. *Med. Phys.* **38** 2366-73.

Amin E. and Meir H. M. 2001. Verification of Photon Beam Data Calculated by a Treatment Planning System Based on Pencil Beam Model. Journal of the Egyptian Nat. Cancer Inst. **13** 57-62.

Supply 25 B.J.R. 1996. Central axis depth dose data for use in radiotherapy. *Br. J. Radiol*. British Institute of Radiology. Supplement. **25** 1-12.

Bomford C. K, Kunkler I. H. and Sherriff S. B. 1993. Walter and Millerôs Textbook of Radiotherapy. Radiation Physics, Therapy and Oncology, Fifth Edition. 42-293.

Both J. A. and Pawlicki T. 2004. Monte Carlo commissioning of low energy electron radiotherapy beams using NXEGS software. *Int. J. Med. Sci.* **1** 63-75.

Chang P. S, Kuo M. P, Sye H. J. *et al* 1993. Commissioning Varian 2100C medical linear accelerator. Department of Radiation Therapy, Kaohsiung Medical College, Taiwan, Republic of China. 1-8.

Chang K. S, Yin F. F, and Nie K. W 1996. The effect of detector size to the broadening of the penumbra-A computer simulated study. *Med. Phys.* **23** 1407-11.

Das I. J, Chee-Wai C, Watts R. J, Ahnesjo A. *et al* 2008. Accelerator beam data commissioning equipment and procedure. Report of the TG-106 of the Therapy Physics Committee of the AAPM 4186-215.

Das I. J. and Zhu T. C. 2004. Thermal and temporal response of ionization chambers in radiation dosimetry. *Med. Phys.* **31**573-8.

Ding G. X. 2003. Using Monte Carlo simulations to commission photon beam output factors-a feasibility study. *Phys. Med. Biol.* **48** 3865-74.

Directorate: Radiation Control 1990. Requirements for medical electron accelerators (photons and electrons). 1-26.

Elder P. J, Coveney F. M. and Welsh A. D. 1995. An investigation into comparison between different dosimetric methods of measuring profiles and depth doses for dynamic wedges on a Varian 600C linear accelerator. *Phys. Med. Biol.* **40** 683-9.

Elekta Synergy Platform 2008.Customer Acceptance Tests. 1-6.

Fogliata A, Nicolini G, Alber M. *et al* 2007. On the performances of different IMRT treatment planning systems for selected paediatric cases. Oncology Institute of Southern Switzerland. *Med. Phys.* Unit 1-21.

Followill D. S. 1998. An empirical relationship for determining photon beam quality in TG-21 from a ratio of percent depth doses. *Med. Phys.* **25** 1202-5.

George D, De Ost B, Hoornnaert M. T. *et al* 1999. Build-up modification of commercial diodes for entrance dose measurements in ôhigher energyô photon beams. *Radiother. Oncol.* **51** 249-56.

Gerbi B. J. and Khan F. M. 1990. Measurement of dose in the buildup region using fixed-separation plane-parallel ion chamber. *Med. Phys.* **17** 17-26.

Guillot M, Gingras L, Archambault L.*et al* 2010. Toward 3D dosimetry of intensity modulated radiotherapy treatments with plastic scintillation detectors. *J. Phys.* **250** 1-5.

Griessbach I, Lapp M, Bohsung J. *et al* 2005. Dosimetric characteristics of a new unshielded silicon diode and its application in clinical photon and electron beams. *Med. Phys.* **30** 3750-4.

Herrup D, Chu J, Cheung H. *et al* 2005. Determination of penumbral widths from ion chamber measurements. *Med. Phys.* **32** 3636-40.

Heydarian M, Hoban P. W, Becham W. A. *et al* 1993. Evaluation of a PTW diamond detector for electron beam measurements. *Phys. Med. Biol.* **38** 1035-42.

Ho A. and Paliwal B. R. 1986. Stopping-power and mass energy-absorption coefficient ratios for solid water. *Med. Phys.* **13** 403-4.

Hoban P. W, Heydarian M, Becham A. *et al* 1994. Dose rate dependence of a PTW diamond detector in the dosimetry of a 6 MV photon beam. *Phys. Med. Biol.* **39** 1219-29.

Howlett S, Kron T, Xuan Ku N.*et al* 1999. Monitor unit calculations using a 3D computerized treatment planning system: Verification in an anthropomorphic phantom. *Austral. Phys. Eng. Sci. Med.* **22** 163-5.

ICRU 1984. Radiation Dosimetry: Electron beams with energies between 1 and 50 MeV. International Commission on Radiation Units and Measurements. Report no **35** Bethesda.

ICRU 1987. Use of Computers in External Beam Radiotherapy Procedures with High Energy photons and Electrons. International Commission on Radiation Units and Measurements. Report no **42** 4-46.

Indrayan A, Satyanarayana L. 2006. Simple Biostatistics for MBBS.PG Entrance and USMLE.

7-217.

IPEM 2007. Acceptance testing and commissioning of linear accelerators. Institute of Physics and Engineering in Medicine. Report No. **94**

Jiang S. B, Sharp G. C, Neicu T, Berbeco R. I. *et al* 2006. On dose distribution comparison. *Phys. Med. Biol.* **51** 759.

Johs H. E. and Cunningham J. R. 1983. The Physics of Radiology. Fourth edition. Springfield, Illinois, USA. 25-67.

Kalach N. I. and Rogers D.W.O. 2003. Which accelerator photon beams are clinic-like for reference dosimetry purposes? *Med. Phys.* **30** 1546-55.

Karzmark C. J. and Pering N. C. 1973. Electron linear accelerator for radiation therapy: History, principles and contemporary developments. Department of Radiology, Stanford University School of Medicine, Stanford, CA 94305, USA. *Phys. Med. Biol.* **18** 321-54.

Khan F. M. 2005. The Physics of Radiation Therapy. Third edition: 28-37, 42-47, 64-75, 97-198. Lippincott Williams and Wilkins.

Khan F. M, Doppke K. P, Hogstrom K. R, Kutcher G. J, Nath R. *et al* 1991. Clinical electron-beam dosimetry. Report of AAPM Radiation Therapy Committee Task Group No 25. *Med Phys.* **18** 73-109.

Khrunov V. S, Martinov S. S, Vatnisky S. M. *et al* 1990. Diamond detectors in relative dosimetry of photon, electron and proton radiation fields. *Radiat. Prot. Dosim.* **33** 155-7.

Kilic A, Ozkan L. and Engin K. 2002.The dosimetric verification of commercial two and three-dimensional radiation treatment planning systems. *Turk. J. Med. Sci*. **32** 133-7.

Kim Y. K, Park S. H, Kim H. S. *et al* 2005. Polarity effect of the thimble-type ionization chamber at a low dose rate. *Phys. Med. Biol.* **50** 4995-5003.

King R. P. and Anderson R. S. 2001. A Simple method for electron energy constancy measurement. American College of Medical Physics 51-3.

Klemp P. F. B, Perry A. M, Hedland-Thomas B. *et al* 1988. Commissioning of the linear accelerator with independent jaws: computerized data collection and transfer to a planning system. *Phys. Med. Biol.* **33** 1-14.

Kosunen A. and Rogers D. W. O. 1993. Beam quality specification for photon beam dosimetry. *Med. Phys.* **20** 1181-8.

Lamb A. and Blake S. 1998. Investigation and modeling of the surface dose from linear accelerator produced 6 and 10 MV photon beams. *Phys. Med. Biol.* **43** 1133-46.

LaRiviere P. 1989. The quality of high-energy x-ray beams. *Br. J Radiol.* **62** 473-81.

Leavitt D. D. and Klein E. 1997. Dosimetry measurement tools for commissioning enhanced dynamic wedge. *Med. Dosim.* **22** 171-6.

Lilie L, Wang W, Rogers D. W. O. 2007. Monte Carlo Study of Silicon diode response in electron beams. *Med. Phys.* **34** 1734-42.

Low D. A. and Dempsey J. F. 2003. Evaluation of the gamma dose distribution comparison method. American Association of Physicists in Medicine.

Marshall M. G. 1992. Matching the 6 MV photon beam characteristics of the two dissimilar linear accelerators. *Med. Phys. Biol.* **42**. 1875-86.

McGowan H. C. E, Faddegon B.A. and Ma C. M. 2007. STATDOSE for 3D dose distributions. Ionization Radiation Standards, NRCC: 1-10.

MeKenna M. G, Chen X. G, Altschuler M. D. *et al* 1995. Calculation of the dose in the build-up region for high energy photon beam. Treatment planning when beam spoilers are employed. *Radiother. Oncol.* **34** 63-8.

Mellenberg D. E, Dahl R.A and Blackwell C. R. 1990. Acceptance testing of an automated scanning water phantom. *Med. Phys.* **17** 311-4.

Metcalfe P, Kron T, Elliot A.*et al* 1993. Dosimetry of 6MV x-ray beam penumbra. *Med. Phys.* **20** 1439-45.

Nath R, Biggs P. J, Bova F. J. *et al* 1994. AAPM code of practice for radiotherapy accelerators: Report of AAPM Radiation Therapy Task Group No. 45. *Med. Phys.* **21** 1093-121.

Nilsson B. and Brahme A. 1986. Electron contamination from photon beam collimators. *Radiother. Oncol.* **5** 235-44.

Niroomand-Rad A, Blackwell C. R, Coursey B. M. *et al* 1998. Radiographic film dosimetry: Recommendations of AAPM Radiation Therapy Committee Task Group 55. *Med. Phys.* **25** 2093-115.

Paganetti H. 2006. Monte Carlo calculations for absolute dosimetry to determine machine outputs for photon therapy fields. *Phys. Med. Biol.* **51** 2801-12.

Pai S, Das I. J, Dempsey J. F. *et al* 2007.TG-69: Radiographic film for megavoltage beam dosimetry. *Med. Phys.* **34** 2228-58.

Podgorsak E. B, Technical editor 2005. Radiation Oncology Physics: A hand book for teachers and students. Sponsored by IAEA. 45-68, 77-92, 123-253.

Podgorsak E. B. 2003. Review of Radiation Oncology Physics: A handbook for teachers and students. International Atomic Energy Agency (IAEA), Vienna, Austria. 90-217.

Quach K. Y, Morales J, Butson M. J. *et al* 2000. Measurement of radiotherapy x-ray skin dose on a chest wall phantom. *Med. Phys.* **27** 1676-80.

Rafaravavy R, Andriambololona R. and Bridier A. 2007. Study of dose distribution in high energy photon beam used in radiotherapy. Oncology & Radiotherapy Department. 1-5.

Ravichandran R, Binukumar J. P, Davis C.A. *et al* 2007. Evaluation methods for detecting changes in beam output and energy in radiation beams from high energy linear acceleratorsô *Med. Phys.* **32** 92-6.

Saini A. S. and Zhu T. C. 2004. Dose rate and SDD dependence of commercially available diode detectors. *Med. Phys.* **31** 914-24.

Saini A. S. and Zhu T. C. 2002. Temperature dependence of commercially available diode detectors. *Med. Phys.* **29** 622-30.

Saminathan S, Manickan R, Chandraraj V. *et al* 2010. Dosimetric study of the 2D ion chamber array matrix for the modern radiotherapy treatment verification. *Journal of Applied Clinical Medical Physics*. **11** 116-27.

Schmid M. G. and Morris R. L. 1989.A water phantom controller for automated acquisition of linac beam parameters. *Med. Phys.* **16** 126-9.

Schreiner L. J. 2011. On the quality assurance and verification of modern radiation therapy treatment. Department of Oncology and Physics, Queenôs University, Kingston, Ontario, Canada. **36** 189-91.

Sharma S. C, Ott J. T, Williams J. B. *et al* 2007. Commissioning and acceptance testing of a Cyber knife linear accelerator. Parkview Comprehensive Cancer Center, Fort Wayne, Indiana, USA.

Shi J, Simon W. E, Zhu T. C. 2003. Modeling the instantaneous dose rate dependence of radiation diode detectors. *Med. Phys.* **30** 2509-19.

Siantar C. L. H, Bergstrom P. M, Daly T. P. *et al* 1999. Clinical implementation of the PEREGRINE Monte Carlo dose calculations system for photon beam therapy. *11th International Congress of Radiation Research Dublin*, Ireland, July 18-23.

Sidhu N. P. 1999. Interfacing a linear diode array to a conventional water scanner for the measurement of dynamic dose distributions and comparison with a linear ion chamber array. *Med. Dosim.* **24** 57-60.

Simpson and John J. 2000. The Sudbury Neutrino Observatory. APT Announcer. **30**.

Sjögren R. and Karlsson M. 1996. Electron contamination in clinical high energy photon beams. *Med. Phys.* **23** 1873-81.

Song H, Ahmad M, Deng J.*et al* 2006. Limitations of silicon diodes for clinical electron dosimetry. *Radiat. Prot. Dosim.* **120** 56-9.

Spokas J. J. and Meeker R. D.1980. Investigation of cables for ionization chambers.
Med. Phys. **7** 135-40.

Starkschall G, Steadham Jr. R. E, Popple R.A. *et al* 2000. Beam commissioning methodology for a three-dimensional convolution/superposition photon dose algorithm. *Journal of Applied Clinical Medical Physics.* **1** 8-27.

Tailor R. C, Tello V. M, and Schroy C. B. *et al* 1998. A generic off-axis energy correction for linac photon beam dosimetry. *Med. Phys.* **25** 662-7.

Tailor R. C, Chu C, Followill D. S. and Hanson W. F. 1998. Equilibration of air temperature inside the thimble of a farmer-type ion chamber. *Med. Phys.* **25** 496-502.

Tello V. M, Tailor R. C. and Hanson W. F. 1995. How water equivalent are water-equivalent solid materials for output calibration of photon and electron beams. *Med. Phys.* **22** 1777-89.

Turian J. V, Smith B. D, Bernard D. A. *et al* 2004. Monte Carlo calculations of the output factors for clinically shaped electron fields. *Am. Coll. Med. Phys*. **42** 42-63.

Tzedakis A, Damilakis J, Mazonakis M. *et al* 2004. Influence of initial electron beam parameters on Monte Carlo calculated absorbed dose distributions for radiotherapy photon beams. *Med. Phys.* **31** 907-13.

TG-21 1983. A protocol for determination of absorbed dose from high-energy photon and electron beam. Radiation Therapy committee, American Association of Physicists in Medicine.

TG-25 1991. Clinical electron beam dosimetry. Report of AAPM Radiation Therapy Committee Task Group No.25. *Med. Phys.* **18** 73-109.

TG-51 1999. AAPMôs TG-51 protocol for clinical reference dosimetry of high-energy photon and electron beams. *Med. Phys.* **26** 1847-70.

TG-53 1998. Quality assurance for clinical radiotherapy treatment planning. American Association of Physicist in Medicine Radiation Therapy Committee Task Group 53. *Med. Phys.* **25** 1773-829.

TG-62 2005. Diode in vivo dosimetry for patients receiving external beam radiation therapy. Report of the AAPM radiation therapy committee Task Group No. 62 Medical Physics. Madison. WI.

Thomas S. C. III, James E. D. and Robert C. M. J. R. 1990. Christensenôs physics of Diagnostic Radiology. *Fourth edition*. Lea and Febiger, Philadelphia.

TRS-398 2001. Absorbed Dose Determination in External Beam Radiotherapy. An International Code of Practice for Dosimetry based on Standards of Absorbed Dose to Water, IAEA.

Veer B. R. 2006. Fundamentals of Biostatistics. Aneôs Student Edition. 80-111.

Weber L, Nilsson P, and Ahnesjo A. 1997. Build-up cap material s for measurement of photon head-scatter factors. *Phys. Med. Biol.* **42** 1875-86.

Woo M, Charland P, and Kim B. *et al* 2003. Commissioning, evaluation, quality assurance and clinical application of a virtual micro MLC technique. *Med. Phys.* **30** 138-43.

Wu X. and Zhu Y. 2001. A maximum entropy method for the planning of conformal radiotherapy. *J. Med. Phys.* 2241-6.

Wysocka A, Maciszewski W. 2000. The Photon beam characteristics of linear accelerator equipped with additional narrow beam collimator. The Andrzej Soltan institute for Nuclear Studies, Department of Accelerator Physics 05-400 Swierk, Poland. 2563-5.

Xing L, Li JG, Pugacher A, Le Q. T. *et al* 1999. Estimation theory and model parameter selection for therapeutic treatment plan optimization. *Med. Phys.* **26** 2348-58.

Yin F. F. 1995.Physical penumbra change of beam profile due to film digitization. *Med. Phys.* **22** 803-5.

Zhu T. C. and Palta J. R. 1989. Electron contamination in 8 and 18 MV photon beams. *Med. Phys.* **25** 12-9.

Zhu T. C, Ding L, Liu C. R. *et al* 1997. Performance evaluation of a diode array for enhanced dynamic wedge dosimetry. *Med. Phys.* **24** 1173-80.

APPENDICES

APPENDIX A-1: List of figures.

Figure 1.1: Block diagram of a linear accelerator (1)

Figure 1.2: Typical linear accelerator head. (2)

Figure 3.1: Therapy x-ray tube with hooded anode. (13)

Figure 3.2: Bremsstrahlung process. (14)

Figure 3.3: The production of characteristic x-rays. (14)

Figure 3.4: The process of the photoelectric effect. (17)

Figure 3.5: The process of coherent scattering. (18)

Figure 3.6: The Compton effect. (19)

Figure 3.7: The pair production process. (21)

Figure 3.8: Relationship between collision Kerma and absorbed dose for ɓ=1. (24)

Figure 3.9: Relationship between collision Kerma and absorbed dose for ɓ=1 and ɓ>1. (24)

Figure 3.10: Depth dose profile for linear accelerator beam. (29)

Figure 3.11: Typical electron beam central axis depth dose curve. (30)

Figure 4.1. Connection setup of the scanning ionization chambers. (40)

Figure 4.2: Cross hairs setup for array calibration. (43)

Figure 4.3: Setup for the absolute dose measurements of the beam data in water. (47)

Figure 5.1: (a) and (b) Graphical summary of indices of photon beam profiles and PDDs. (53)

Figure 5.2: (a) and (b) Graphical summary of indices of electron beam profiles and PDDs. (54)

Figure 5.3. (i): Beam profiles measured at 0.5 cm depth for 6 MV. (a) 3D-water phantom. (b) Profiler 2 scanning system. (55)

Figure 5.3. (ii): Beam profiles measured at 1.0 cm depth for 6 MV. (a) 3D-water phantom. (b) Profiler 2 scanning system. (55)

Figure 5.3. (iii): Beam profiles measured at 2.0 cm depth for 6 MV. (a) 3D-water phantom. (b) Profiler2 scanning system. (56)

Figure 5.3(iv): Beam profiles measured at 5.0 cm depth for 6 MV. (a) 3D-water phantom. (b) Profiler 2 scanning system. (56)

Figure 5.4(i): Beam profiles measured at 0.5 cm depth for 15 MV. (a) 3D-water phantom. (b) Profiler 2 scanning system. (57)

Figure 5.4(ii): Beam profiles measured at 1.0 cm depth for 15 MV. (a) 3D-water phantom. (b) Profiler 2 scanning system. (58)

Figure 5.4(iii): Beam profiles measured at 2.0 cm depth for 15 MV. (a) 3D-water phantom. (b) Profiler 2 scanning system. (58)

Figure 5.4(iv): Beam profiles measured at 5.0 cm depth for 15 MV. (a) 3D-water phantom. (b) Profiler 2 scanning system. (59)

Figure 5.5: Comparison of beam profiles at 1.0 cm depth. (a) 3D-water phantom and profiler 2 scanning system for 6 MV. (b) 3D-water phantom and profiler 2 scanning system for 15 MV. (60)

Figure 5.6: PDDs for 6 MV photon beam. (a) 3D-water phantom. (b) Perspex block. (61)

Figure 5.7: PDDs for 15 MV photon beam. (a) 3D-water phantom. (b) Perspex block. (61)

Figure 5.8 (i): Comparison of measured beam profiles for 3D-water phantom and Profiler 2 scanning system for 4 MeV electron beam measured at 0.5 cm depth. (62)

Figure 5.8 (ii): Beam profiles for 6 MeV measured at 1.0 cm depth. (a) 3D-water phantom. (b) Profiler 2 scanning system. (63)

Figure 5.8 (iii): Beam profiles for 8 MeV measured at 1.0 cm depth. (a) 3D-water phantom. (b) Profiler 2 scanning system. (63)

Figure 5.8 (iv): Beam profiles for 10 MeV measured at 1.0 cm depth. (a) 3D-water phantom. (b) Profiler 2 scanning system. (64)

Figure 5.8 (v): Beam profiles for 12 MeV measured at 1.0 cm depth. (a) 3D-water phantom. (b) Profiler 2 scanning system. (64)

Figure 5.8 (vi): Beam profiles for 15 MeV measured at 1.0 cm depth. (a) 3D-water phantom. (b) Profiler 2 scanning system. (65)

Figure 5.8 (vii): Beam profiles for 8 MeV measured at 2.0 cm depth. (a) 3D-water phantom. (b) Profiler 2 scanning system. (65)

Figure 5.8 (viii): Beam profiles for 10 MeV measured at 2.0 cm depth. (a) 3D-water phantom. (b) Profiler 2 scanning system. (66)

Figure 5.8 (ix): Beam profiles for 12 MeV measured at 2.0 cm depth. (a) 3D-water phantom. (b) Profiler 2 scanning system. (66)

Figure 5.8 (x): Beam profiles for 15 MeV measured at 2.0 cm depth. (a) 3D-water phantom. (b) Profiler 2 scanning system. (67)

Figure 5.8 (xi): Beam profiles for 15 MeV measured at 5.0 cm depth. (a) 3D-water phantom. (b) Profiler 2 scanning system. (67)

Figure 5.8 (xii): Comparison of beam profiles measured at 1.0 cm depth. (a) 6 MeV electron beam. (b) 8 MeV electron beam. (68)

Figure 5.8 (xiii): Comparison of beam profiles measured at 1.0 cm depth. (a) 10 MeV electron beam. (b) 12 MeV electron beam. (69)

Figure 5.8 (xiv): Comparison of beam profiles measured at 1.0 cm depth for 15 MeV electron beam. (69)

Figure 5.9 (i): Measured PDDs for all field sizes for 6 MeV. (a) 3D-water phantom. (b) Perspex block. (70)

Figure 5.9 (ii): Measured PDDs for all field sizes for 8 MeV. (a) 3D-water phantom. (b) Perspex block. (71)

Figure 5.9 (iii): Measured PDDs for all field sizes for 10 MeV. (a) 3D-water phantom. (b) Perspex block. (71)

Figure 5.9 (iv): Measured PDDs for all field sizes for 12 MeV. (a) 3D-water phantom. (b) Perspex block. (72)

Figure 5.9 (v): Measured PDDs for all field sizes for 15 MeV. (a) 3D-water phantom. (b) Perspex block. (72)

Figure 5.9 (vi): Comparison of PDDs for all electron beam energies. (a) 3D-water phantom. (b) Perspex block. (73)

Figure 5.10: Comparison of the 3D-water phantom, Profiler 2 scanning system and CMS XiO TPS beam profiles for the 10 × 10 cm^2 measured at 5.0 cm depth. (a) 15 MV. (b) 6 MV. (81)

Figure 5.11: Comparison of the 3D-water phantom, Perspex block and XiO TPS PDDs for the 10 × 10 cm^2 for the 15 and 6 MV photon beams. (82)

Figure 5.12 (i): Comparison of the 3D-water phantom, Profiler 2 scanning system and CMS XiO TPS beam profiles for the 10×10 cm^2 field size measured at 1.0 cm depth. (a) 4 MeV. (b) 6 MeV. (83)

Figure 5.12 (ii):Comparison of the 3D-water phantom, Profiler 2 scanning system and CMS XiO TPS beam profiles for the 10 × 10 cm^2 field size measured at 1.0 cm depth. (a) 8 MeV. (b) 10 MeV. (83)

Figure 5.12 (iii): Comparison of the 3D-water phantom, Profiler 2 scanning system and CMS XiO TPS beam profiles for the 10 × 10 cm^2field size measured at 1.0 cm depth. (a) 12 MeV. (b) 15 MeV. (84)

Figure 5.13: Comparison of the 3D-water phantom, the Perspex block and CMS XiO TPS PDDs for the 10 × 10 cm^2 applicator size for all electron energies (4, 6, 8, 10, 12 and 15 MeV). (85)

APPENDIX A-2: List of pictures.

Picture1: Elekta Synergy Platform linear accelerator. (32)

Picture 2: 1D-water phantom. (34)

Picture 3: The profiler 2 scanning system. (37)

Picture 4: Setup of the 3D-water phantom for measurements of photon beam data. (39)

Picture 5: Setup of the 3D-water phantom for measurements of electron beams data. (42)

Picture 6: Setup of profiler 2 scanning system. (45)

Picture 7: Setup of Perspex block for measurements of PDDs for photon beams data. (46)

APPENDIX A-3: List of tables.

Table 1: Comparison of beam profiles for the 6 MV photon beam at 0.5 cm depth. (74)

Table 2: Comparison of beam profiles for the 15 MV photon beam at 0.5 cm depth. (74)

Table 3: Comparison of beam quality for 6 and 15 MV photon beams for a 10 × 10 cm^2 field size. (75)

Table 4: PDDs for electron beams. (75)

Table 5: Comparison of beam profiles for the 4 MeV electron beam at 0.5 cm depth. (76)

Table 6: Comparison of beam profiles for the 6 MeV electron beam at 0.5 cm depth. (76)

Table 7: Comparison of beam profiles for the 8 MeV electron beam at 0.5 cm depth. (77)

Table 8: Comparison of beam profiles for the 10 MeV electron beam at 0.5 cm depth. (77)

Table 9: Comparison of beam profiles for the 12 MeV electron beam at 0.5 cm depth. (78)

Table 10: Comparison of beam profiles for the 15 MeV electron beam at 0.5 cm depth. (78)

Table 11: Comparison of absolute dose measurements. (87)